2012

Skill assessment and optimization of the third generation wave models for applications in Gulf of Mexico

Seyed Mostafa Siadatmousavi
Louisiana State University and Agricultural and Mechanical College

SKILL ASSESSMENT AND OPTIMIZATION OF THE THIRD GENERATION WAVE MODELS FOR APPLICATIONS IN GULF OF MEXICO

A Dissertation

Submitted to the Graduate Faculty of the
Louisiana State University and
Agricultural and Mechanical College
in partial fulfillment of the
requirements for the degree of
Doctor of Philosophy

in

The Department of Oceanography and Coastal Sciences

by
Seyed Mostafa Siadatmousavi
B.S., Isfahan University of Technology, 2003
B.S., Isfahan University of Technology, 2004
M.S., University of Tehran, 2006
May 2012

ACKNOWLEDGEMENTS

This dissertation could not have been completed without dedicated help and support from numerous people. I begin by thanking my former advisor, Dr. Gregory W. Stone, who passed away in last winter, 2011. His continuous encouragements, even when apparent setback happened, gave me enough confidence and motivation for completing my research. I also wish to express my gratitude to Dr. Harry H. Roberts who took over the chair of the dissertation committee and eventually allowed me to complete this work. I appreciate my co-advisor, Dr. Q. Jim Chen at Civil and Environmental Engineering Department for dedicated commitments to my doctoral research and allowing me to work closely with his research group. It is hard to forget Dr. Chunyan Li, my committee member and new director of WAVCIS lab who taught me critical thinking, hard work and many teaching skills. I am also thankful to the other committee members, Drs. Nan D. Walker, Dubravko Justic and Aixin Hou for suggestions which improved this dissertation substantially.

I appreciate help from CSI field support group staff and discussions in the WAVCIS Laboratory. Dr. Felix Jose carefully reviewed all proposals and manuscripts and gave me frank and useful comments. Especial thank to MohammadNabi Allahdadi who helped me to clarifying the objectives and methods of my research, and Yixin Luo who set up two clusters for WAVCIS Laboratory. The help from Dr. Baozhu Liu, Yuliang Chen, Amy Spaziani, Daijiro Kobashi and Clint Edrington must be recognized.

I wish to thank Dr. Marcel Zijlema (Delft University of Technology) for sharing the source code of unstructured SWAN before its official release, Dr.ir. Gerben J. de Boer for sharing the source code of SWANMud (Delft University of Technology), and Jonathan R. Shewchuk (UC-Berkeley) for providing the Triangle grid generation tool.

Finally, the seemingly endless patience and support of my family, especially my parents, back in Iran must also be appreciated.

TABLE OF CONTENTS

ACKNOWLEDGEMENTS ii

ABSTRACT v

CHAPTER 1: INTRODUCTION 1
1.1 The Basic Physics of Third Generation Wave Models 1
1.2 Open Source Third Generation Wave Models 2
1.3 Preparation of General Data Used to Run a Wave Model 3
1.4 Statistical Parameters Used for Evaluation 6
1.5 Objectives 7
1.6 Organization of Dissertation 7

CHAPTER 2: EVALUATION OF TWO WAM WHITE CAPPING PARAMETERIZATIONS USING PARALLEL UNSTRUCTURED SWAN WITH APPLICATION TO THE NORTHERN GULF OF MEXICO, U.S.A. 9
2.1 Introduction 9
2.2 Methods 10
2.3 Results and Discussion 13
2.4 Conclusions of Chapter 2 21

CHAPTER 3: ON THE IMPORTANCE OF HIGH FREQUENCY TAIL IN THIRD GENERATION WAVE MODELS 23
3.1 Introduction 23
3.2 Third Generation Wave Models and High Frequency Tail 25
3.3 Methods 26
3.4 Results and Discussion 28
3.5 Conclusions of Chapter 3 41

CHAPTER 4: THE EFFECTS OF BED FRICTION ON WAVE SIMULATION: IMPLEMENTATION OF AN UNSTRUCTURED THIRD-GENERATION WAVE MODEL, SWAN 43
4.1 Introduction 43
4.2 Methods 45
4.3 Results and Discussion 46
4.4 Conclusions of Chapter 4 48

CHAPTER 5: WAVE AND BOTTOM BOUNDARY LAYER DYNAMICS OVER THE SAND SHOALS OFF THE ATCHAFALAYA SHELF DURING COLD FRONTS 51
5.1 Introduction 51
5.2 Experimental Setting 53
5.3 Methods 56
5.4 Observations 59
5.5 Discussion 68
5.6 Conclusions of Chapter 5 74

CHAPTER 6: SIMULATION OF WAVE DAMPING DURING A COLD FRONT OVER THE MUDDY ATCHAFALAYA SHELF 77
6.1 Introduction 77
6.2 Experimental Setting 81
6.3 Method 81
6.4 Results 86
6.5 Discussions 89
6.6 Conclusions of Chapter 6 95

CHAPTER 7: SYNTHESIS AND CONCLUSIONS 98
7.1 Calibration of Whitecapping Term 98
7.2 Slope of High Frequency Tail and Cut-off Frequency 98
7.3 Use of Sediment Characteristics in Bed Friction Term 99
7.4 Inclusion of Mud-induced Attenuation of Wave Energy 99
7.5 Directions for Future Research 100

REFERENCES 102

APPENDIX A: COVER PAGE OF JOURNAL OF APPLIED OCEAN RESEARCH PAPER 116

APPENDIX B: COVER PAGE OF JOURNAL OF COASTAL ENGINEERING PAPER 117

APPENDIX C: ELSEVIER COPYRIGHT POLICY 118

APPENDIX D: COVER PAGE OF JOURNAL OF COASTAL RESEARCH PAPER 119

APPENDIX E: LETTER OF PERMISSION; JOURNAL OF COASTAL RESEARCH 120

VITA 121

ABSTRACT

Numerical phase-averaged wave models are the best option to obtain the spatial and temporal distribution of the wave energy over a large domain, such as the Gulf of Mexico. Parallel implementation of unstructured SWAN and WAVEWATCH-III were engaged in this research to evaluate the performance of third generation wave models for different conditions. Met-ocean data from a network of NDBC buoys and WAVCIS stations were used to assess the predictive skills of the wave models.

Deep water wave energy dissipation formulations were carefully analyzed and modified to improve the accuracy of the bulk wave parameters. Moreover, the importance of the assumptions for choosing the high frequency cut-off and the slope of the power law for the frequency tail were highlighted by several simulations using SWAN and WAVEWATCH-III. The results show that previous underestimation of wave period reported from the WAM-3 formulation of SWAN was partially attributed to the different assumptions used on the high frequency end of the spectrum.

When waves propagate to shallow water, several other processes affect the wave spectrum such as dissipation of wave energy by bed friction in non-cohesive environments. The wave model with an optimized set of coefficients for the Gulf of Mexico was used to skill assess two widely used bed friction formulations. Simulation results showed that the incorporation of sediment information in an eddy viscosity formulation led to more accurate wave hindcast than the JONSWAP formulation. The computation cost required to use the proposed formulation increased by less than 4%.

The turbid plume exiting the Atchafalaya Bay system significantly influences the wave spectrum of western Louisiana coast. Using extended deployments during low and high discharge periods of the Atchafalaya River, meteorological, hydrodynamic and bottom boundary layer parameters were monitored from Tiger and Trinity Shoals. These datasets were used to evaluate the mud-wave interaction in SWAN. The numerical algorithm to solve the complex dispersion equation of SWAN was optimized. Moreover, the model was extended to incorporate the damping term in non-stationary simulations. The results show that without including the mud-effects, the high frequency waves were overestimated close to Tiger Shoal during northerly winds.

CHAPTER 1: INTRODUCTION

1.1 The Basic Physics of Third Generation Wave Models

The third-generation phase-averaged wave models are efficient tools for simulating wave fields in medium- and large-scale domains (Zubier et al., 2003). Larger grid sizes (and therefore temporal time steps) are allowable in the statistical description of wave compared to phase resolving models, because there is no need to have several grid points in each wavelength to resolve the wave shape information. Since practical observations of wave phase are limited, and the computational benefits are significant, these models have been used since 1960s (Janssen, 2008). The phase-averaged models are based on the wave action balance equation which is also valid in the presence of ambient currents (Whitham, 1965), and is given by:

$$\frac{DN}{Dt} = \frac{S_{tot}}{\sigma} \tag{1.1}$$

in which $N \equiv F/\sigma$ is wave action density, F is wave energy density, $\sigma = 2\pi f$, in which f denotes relative frequency, and S_{tot} is the total of source/sink terms. The main two differences of third generation wave models compared with earlier generations are 1) the presence of an explicit formulation for nonlinear wave-wave interaction, and 2) exclusion of any pre-assumed form for sea or swell part of the wave spectrum (Massel, 1996).

The left hand side of Equation 1.1 gives the rate of change of the sea state caused by adiabatic processes such as advection, wave refraction, and shoaling. Wind input (S_{in}), quadruplet wave-wave interaction (S_{nl4}), and energy dissipation due to white cap (S_{dis}) are the most common source/sink terms in deep water (Komen et al., 1994). When waves propagate across intermediate and shallow waters, wave transformation processes such as bed friction (S_{bot}) become important (Graber and Madsen, 1988), especially during high energy events (Li and Mao, 1992). The rate of energy dissipation is roughly estimated as a few watts per square meter, approximately the same as the rate of energy transferred from wind to the sea surface during moderate wind conditions (Cavaleri et al., 2007).

The substantial damping of wave energy due to complex interaction with a cohesive sediment bottom also has to be considered for deltaic coasts (Sheremet and Stone, 2003). Depending on the characteristics of the mud layer, the mud dissipation term (S_{mud}) may have very different spectral behavior compared to S_{bot} (see Chapter 6). Wave breaking (S_{bre}) is another energy sink process which needs to be included in Equation 1.1. Spectral characteristics of waves are also affected when propagating in shallow water. Since the phase speed is almost independent of wave frequency in shallow water, the waves are weakly- to non-dispersive and wave components stay with each other for a long period of time, which attracts near-resonant conditions for three wave frequencies (S_{nl3}) (Janssen, 2004). Assuming weak interaction among

the aforementioned processes, S_{tot} can be expressed as linear summation of all sink and source terms:

$$S_{tot} = S_{in} + S_{nl4} + S_{dis} + S_{bot} + S_{mud} + S_{bre} + S_{nl3} \quad (1.2)$$

1.2 Open Source Third Generation Wave Models

In his pioneering work, Komen (1984) showed that the pulse-based quasi-linear model of Hasselmann (1974), proposed for calculating the dissipation induced in the form of white cap, and the rescaled wind input formulation of Snyder et al (1981), were able to reproduce the fully developed wind sea. These formulations became the core of the WAM cycle 3 wave model. A more detailed understanding of the complex interaction of wind and waves in energy transfer to waves resulted in a newer wind input formulation (Janssen, 1991) and was incorporated in WAM cycle 4; along with a dissipation term with quadratic dependence on the wavenumber to provide more dissipation in high frequency end of the spectrum (Janssen, 2004). The WAM formulations have been included in most of the other phase-averaged wave models developed later. In this study, two widely used wave models, SWAN and WAVEWATCH-III are employed for different simulations. A brief introduction of these models is presented in this section.

The well-documented wave model SWAN (Simulating WAves Nearshore) was developed originally to simulate nearshore water wave transformation, by Delft University of Technology (SWAN team, 2010). Unlike most popular third generation wave models, SWAN employs second and third order implicit schemes to solve the Eulerian form of Equation 1.1 in (σ, θ) spectral domain for stationary and non-stationary simulations respectively. The use of implicit schemes implies that the time step is mainly determined by the desired temporal accuracy, rather than the restriction by stability criteria of an explicit scheme in shallow water. Since version 40.72, SWAN provides an opportunity to use the Finite Volume method to solve the wave action equation on an unstructured triangular mesh; so that the user can incorporate a finer mesh for zones of interest, with approximately no change in total computational cost, and still use coarser grids where sharp modification in energy spectra is not expected.

The version 40.72 of SWAN is used throughout this study except in Chapter 6 (see section 6.3 for more details). This model has several formulations for S_{in} and S_{dis}, including WAM-3 and WAM-4, which makes it an appropriate platform to compare the performance of different formulations. The linear wave growth according to Cavaleri and Rizzoli, (1981) is also included in S_{in} to provide more realistic results in early stages of wave developments. Details of these formulations are presented in section 2.2. Although an exact expression for calculating nonlinear quadruplet wave-wave interaction is formulated to be used in SWAN (van Vledder, 2006), it is not feasible to implement it for operational wave forecasting purposes, due to intense numerical calculations involved. By considering only a few configurations from all plausible combinations of interacting wavenumbers, Discrete Interaction Approximation (DIA) provides a

fast estimation of wave-wave interaction term in third generation operational wave models (Hasselmann et al., 1985). Although this method is criticized for being oversimplified to produce an exact wave spectrum (Hasselmann and Hasselmann, 1985; van Vledder, 2006; van Vledder GP. and Bottema, 2003), it has proved itself to be accurate enough to reproduce bulk wave parameters (Janssen et al., 1994). Due to limited computational resources, DIA was used to estimate S_{nl4} in all wave simulations in this study. Moreover the nonlinear triad interaction is considered according to Eldeberky (1996), and depth-induced wave breaking according to Battjes and Janssen (1978). Several formulations are available for including bed friction in SWAN such as the JONSWAP formulation (Hasselmann et al., 1973) and the eddy-viscosity model of Madsen et al. (1988). More details on these bed friction formulations are presented in section 4.2.

Another commonly used third generation wave model is WAVEWATCH-III, developed at the Marine Modeling and Analysis Branch of National Centers for Environmental Prediction, (NCEP/NOAA). It was designed originally for deep water wave evolution and transformation, and considered to be one or two orders of magnitude more efficient than SWAN at oceanic scales. However, since its latest version, 3.14, it also includes formulations for most of the shallow water processes. However, it is estimated that WAVEWATCH-III is one order of magnitude slower than SWAN in shallow waters (SWAN team, 2010). WAVEWATCH-III employs either an explicit third order scheme called ULTIMATE QUICKEST or the explicit first order upwind scheme to solve the wave action balance equation in spectral domain (k,θ) in which k is wavenumber (Tolman, 2009). Beside WAM formulations, WAVEWATCH-III includes the Tolman and Chalikov (1996) source package which is based on the energy transfer formulations of Chalikov (1995) and Chalikov and Belevich (1993). Its dissipation term also consists of a low frequency constituent, based on the analogy with turbulence, and an empirical formulation for contribution from high frequency constituents. Similar equations to SWAN were used in WAVEWATCH-III for the nonlinear quadruplet wave-wave interaction, linear wave growth, and depth-induced wave breaking.

Beside the difference in numerical schemes and discretization of Equation 1.1 in different spectral domains, there are some different assumptions on the high frequency tail of the spectrum in SWAN and WAVEWATCH-III. These differences will be explained in Chapter 3 in more details.

1.3 Preparation of General Data Used to Run a Wave Model

It is not surprising that all of the formulations for wind input in wave models are a function of wind speed. The wind velocity components were extracted from the North American Regional Re-analyzed (NARR) database from the National Center for Environmental Prediction/ National Oceanic and Atmospheric Administration (NCEP/NOAA) server. The NARR data grid 221 covers the entire continental US and the Gulf of Mexico with the horizontal resolution of ~32 km.

In order to prepare wind data for simulating Hurricanes, higher resolution wind data, especially near the center of a hurricane, were necessary. Combining National Oceanic and Atmospheric Administration (NOAA)/Hurricane Research Division (HRD) high resolution re-analyzed wind data (online at www.aoml.noaa.gov/hrd) with NARR data provides higher resolution to investigate the dynamics associated with wind asymmetry near the center of a hurricane. The HRD wind data are derived from a synthesis of all available surface weather platforms, aviation reports, and reconnaissance aircraft data adjusted to the surface, providing 6 km resolution data within the 1000 km × 1000 km "moving box" centered around a hurricane's track. Linear interpolation was used in both time and space domains to blend two sets of wind data to prepare wind inputs for wave model for every three hours.

In order to prepare the depth information required by wave models, bathymetry was downloaded from the National Geophysical Data Center (NGDC). Three seconds cell size (~90 m) data from the *US Coastal Relief Model Grids* database for the northern Gulf of Mexico were combined with coarser *ETOPO1 1-minute Global Relief* database that covered the entire Gulf. The linear interpolation subroutine of MATLAB® was used to determine the depth for each mesh node from the best database and the result was carefully checked to remove any potential anomalies in both databases. The result was ready to use for a wave model with a structured grid. Note that recent measurements of Roberts et al. (2010) from Tiger and Trinity Shoals were incorporated in the bathymetry files used in Chapter 6.

In order to use an unstructured grid, the triangular mesh should be produced for the study area. The computational grid requires enough resolution to accommodate the complex bathymetry of shallow water for accurate coastal wave modeling (Hagen et al., 2002). In this study, the BatTri package (Bilgili et al., 2006) was originally used to generate the computational mesh file. This mesh was later enhanced by smoothing the mesh size change using SMS ver 10.1. Although the use of the implicit numerical scheme in SWAN ensures unconditional numerical stability, the accuracy of the result is highly dependent on mesh quality. Hence, additional precautions were taken during mesh generation to avoid a steep element slope, very small vertex angles, or even significant change in mesh size relative to the adjoining mesh elements (SWAN team, 2010). The final mesh file for Gulf of Mexico is shown in Figure 1.1, which consists of 32,235 nodes and 59,258 triangles with the element lateral length varying from 1 km nearshore to 50 km in deeper water. A higher mesh resolution is assigned where a sharp change in the wave spectrum is expected, such as shallow water.

In order to run the wave model in parallel, the mesh file was partitioned into sub-grids using *adcprep,* the grid preparation module of the circulation model ADCIRC (Westerink et al., 1992). The 70 mesh partitions are also presented in Figure 1.1. A linear speedup for PunSWAN was established on a Linux cluster with 35 nodes, each of them having two Intel(R) Xeon(TM) CPU 3.06GHz processors and 2GB RAM, which reaffirms the optimized parallelization of the SWAN source code (Zijlema, 2009). These nodes were connected by optical cable and MX protocol for communications.

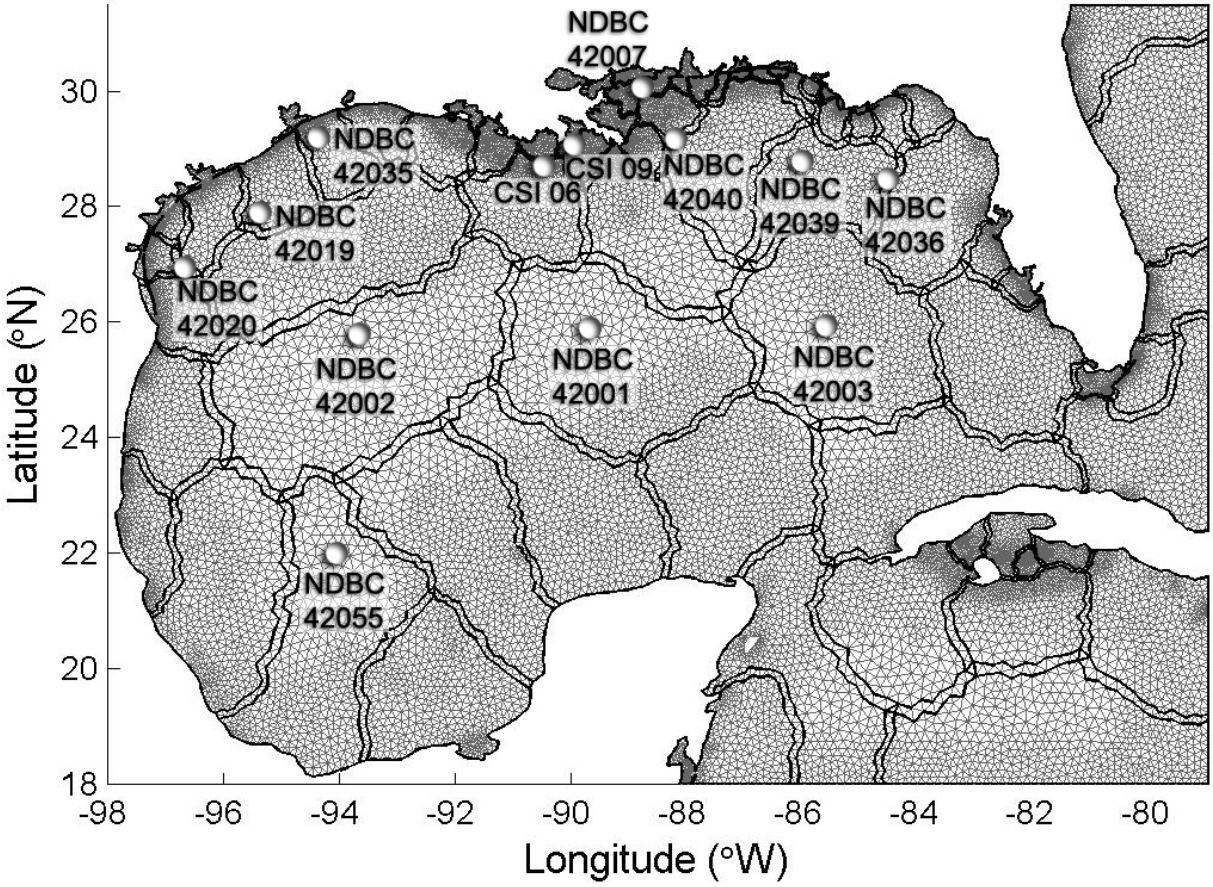

Figure 1.1: Mesh file and its different partitions for parallel computing using 70 processors. The calculations for the common vertices along the boundaries are accomplished in both adjacent sub-grids. The locations of in situ met-ocean data monitoring in deep water (NDBC Buoys) and shallow water (WAVCIS CSI stations) used in this study are also provided.

Wave, wind and meteorological archived data from several deep water buoys obtained from the National Data Buoy Center (NDBC) were analyzed to ascertain the accuracy of the wind field (main driving force for waves) and the computed deep water bulk wave parameters, from SWAN. Additional data were obtained from WAVCIS (Wave Current Surge Information System, www.wavcis.lsu.edu) stations (Stone et al., 2001), maintained by the Coastal Studies Institute at Louisiana State University, to similarly evaluate the model for shallow waters, where more complex processes such as bed friction and depth-induced wave breaking are also important. The locations of *in situ* observations used in this study are also given in Figure 1.1.

As shown in Table 1.1, sustained wind speed at some of these stations is measured at elevations other than 10 m above mean sea level (MSL), the unified standard set by WMO (WMO, 2008). Since wave models are formulated based on the wind speed at 10 m above MSL

(referred to as U_{10}), the measured wind speed at elevation z above MSL (referred to as U_z) needs to be converted to U_{10}. One of the widely accepted conversion formula is based on a logarithmic wind profile (Peixoto and Oort, 1992; Thomas et al., 2005). The power-law wind profile is another simple method for reconstruction of the wind profile over an offshore water body in a neutral-condition, which is the case for moderate and strong wind speeds that produces noticeable wind-induced sea state (Hsu, 1988). However, these theories are not valid in unstable conditions nor for very stable conditions (Walmsley, 1988).

There are also more complex formulae such as the LKB model (Liu and Tang, 1996) that take into account the stability state and the effects of temperature and humidity on the wind profile. Although these methods were close for most of the time periods used in this study, the LKB method was selected for calculations due to its general applicability.

Table 1.1: Anemometer elevation (from MSL) at various *in situ* observation stations.

Station	NDBC											WAVCIS	
	42001	42002	42003	42007	42019	42020	42035	42036	42039	42040	42055	CSI06	CSI09
Anemometer height (m)	10	10	10	5	5	5	5	5	5	5	10	40	32

1.4 Statistical Parameters Used for Evaluation

Statistical parameters are useful to compare the simulated bulk wave parameters such as wave height and wave period with the corresponding measured parameters. They can be used also to check the quality of input wind used to run the wave model. The Bias, root mean square error (RMSE), Scatter Index (SI) are the most common statistical parameters used to evaluate the performance of wave models (Alves et al., 2002; Ardhuin et al., 2010; Janssen, 2008) and defined as:

$$Bias = \sum_{i=1}^{N} \left(X_{Mi} - X_{Oi} \right) \tag{1.3}$$

$$RMSE = \sqrt{\frac{1}{N} \sum_{i=1}^{N} \left(X_{Mi} - X_{Oi} \right)^2} \tag{1.4}$$

$$SI = \frac{RMS}{Mean} = SI = \frac{\sqrt{\frac{1}{N} \sum_{i=1}^{N} \left(X_{Mi} - X_{Oi} \right)^2}}{\frac{1}{N} \sum_{i=1}^{N} X_{Oi}} \tag{1.5}$$

in which X_{Oi} and X_{Mi} denote ith data resulted from observation and model, respectively, and N is the total number of data points.

1.5 Objectives

The main purpose of this study is to reproduce the measured wave spectrum in the Gulf of Mexico during different meteorological conditions using phase averaged models. However, there are several objectives within this broad topic:

1) The model composed of several sources and sinks as discussed in section 1.1 and the deficit of some terms is sometimes corrected by spurious behavior of other terms (Ardhuin et al., 2007). Therefore as a first objective of this study, the white capping dissipation term was calibrated against measured data in deep water.
2) Different models have different assumptions on frequency range in which they are being used, and it is important to study the effects of these assumptions on the overall performance of wave model.
3) The model with optimized coefficient for deep water terms is used to skill assess the performance of friction formulation in non-cohesive environment during several cold fronts with intermittent fair weather periods as well as hurricane situations.
4) Inclusion of the mud-wave interaction over non-rigid bottoms in phase averaged wave models is a topic of recent studies. These models were tested for the propagation of stationary wave train over muddy environment. However, for the cold front conditions in which wind turns its direction, special treatments are required in the code of the model. Extending the model capabilities to a non-stationary simulation is the last objective of this study.

1.6 Organization of Dissertation

This dissertation includes 7 chapters which summarize the modifications implemented in formulations of the phase-averaged wave models to improve their performance, and processing of the required input data. Chapter 1 presented an introduction to the third generation wave models, basic data required to run the model, basic tools to evaluate the performance of model, and the objectives of this study.

Chapter 2 describes an optimization effort to minimize the error of hindcasting bulk wave parameters in the Gulf of Mexico using two widely used formulations of the wave model. These formulations were further modified to provide a better estimate of the wave field during cold front events as well as intermittent fair weather periods. The effects of different assumptions on the high frequency tail of the wave spectrum and high cut-off frequency on simulated bulk wave parameters are presented in Chapter 3.

Chapter 4 investigates the bed friction term in the wave model and the spatial extent in which this term has a significant role in simulated bulk wave parameters. Moreover the application of the model with two different formulations for the bed friction term was assessed during the passages of several cold fronts and also hurricane Dennis which made landfall in 2005.

In Chapters 5, an intense data analysis of two *in situ* data collection deployments in Atchafalaya Shelf is discussed. The wave parameters, current profiles, and acoustic and optical estimates of bottom boundary parameters resulted from these deployments were used to study the interaction of wave and cohesive bottom in Chapter 6.

A summary of all the work, recommendations of this study, and suggested future investigations are presented in Chapter 7.

CHAPTER 2: EVALUATION OF TWO WAM WHITE CAPPING PARAMETERIZATIONS USING PARALLEL UNSTRUCTURED SWAN WITH APPLICATION TO THE NORTHERN GULF OF MEXICO, U.S.A.[1]

2.1 Introduction

Among source/sink terms in deep water (wind input, quadruplet wave-wave interaction and energy dissipation (Komen et al., 1994)), dissipation is widely considered to be the least understood term (Cavaleri et al., 2007). Although several different formulations have been proposed for energy dissipation in deep water (Babanin et al., 2010; Cavaleri et al., 2007; Rogers et al., 2003; Tolman and Chalikov, 1996; van der Westhuysen et al., 2007), the pulse-based quasi-linear model for the white capping term proposed by Hasselmann (Hasselmann, 1974) remains in use in third generation wave models (SWAN team, 2010; Tolman, 2009). This approach successfully reproduces the fully developed wind-sea when used in conjunction with efficient quadruplet nonlinear wave interaction formulation referred to as the Discrete Interaction Approximation (DIA) (Hasselmann et al., 1985), and rescaled wind input formulation of Snyder et al (Komen et al., 1984; Snyder et al., 1981). These sets of equations are used in the WAM cycle 3 model and are referred to as WAM-3 hereafter.

Advancements in understanding of wave growth in open water led to a theoretical description of the wind input term, which results in an acceptable level of agreement with *in situ* measurements (Janssen, 1991). The WAM cycle 4 model (WAM-4) employs wind-wave energy transfer parameterization based on quasi-laminar theory, and also considered quadratic dependence of dissipation on the wavenumber to provide more flexibility in the formulation for white capping dissipation (Janssen, 2004). This formulation also became part of many recent third generation wave models (Sorensen et al., 2004; SWAN team, 2010; Tolman, 2009).

The third generation model, SWAN has been well suited for both parameterizations, WAM-3 and WAM-4, and hence provides a tangible platform to compare and contrast their performance. Although originally developed for shallow water, SWAN incorporates all source and sink terms for generation and propagation of waves in deep and shallow water, and has been verified for several geographic settings and for different met-ocean conditions (Kagan et al., 2008; Moeini and Etemad-Shahidi, 2007; Palmsten, 2001; Rogers et al., 2003; Rogers et al., 2007; Zhang et al., 2003; Zijlema and van der Westhuysen, 2005; Zubier et al., 2003). The free coefficients of wave models, in this case SWAN, are conventionally set so that the model can reproduce saturation level spectra, among which the one suggested by Pierson-Moskowitz (P-M) is probably the most popular (Massel, 2007; Pierson and Moskowitz, 1964). However, Rogers et al. (Rogers et al., 2003) stated that the wave models reach the saturation energy level too slowly.

[1] Reprinted by permission of the Journal of Applied Ocean Research (see Siadatmousavi et al, 2011b)

Moreover, it is not possible to calibrate the model for all possible wind speeds, because the P-M spectrum scales with wind speed while the model formulations are scaled with friction velocity. Finally, tuning the model for unlimited time and fetch conditions may not be a realistic representation of wave growth in real-world situations. Therefore, in this study, the free parameters are determined by comparing the simulated significant wave height (H_s), peak wave period (T_p), and averaged wave period (T_a) with *in situ* observations.

In this study, instead of calibrating the model against the P-M spectrum, a classical approach to adjust the model parameters is implemented, in which the model is calibrated and verified using *in situ* measurements (Kamphuis, 2000). However, as a reference, the performance of the calibrated model is compared with the same model tuned for the P-M spectrum. In addition, Rogers et al. (Rogers et al., 2003) showed that using a higher order wavenumber term in white capping formulation of WAM-3 enhances the model performance when compared with the *in situ* observations; An in-depth analysis of this model performance along with similar modifications to WAM-4 are presented in this study. The same modifications are also applied to the steepness term in the white capping formulation of WAM-3 (see section 2.2) which has been assumed to be constant without any clear scientific explanation. Therefore, the main objective of this study is to evaluate the effect of possible modifications in WAM-3 and WAM-4 white capping formulations when compared with known fetch-limited and fully-developed wave data as well as long term *in situ* measurements.

2.2 Methods

The wind input source term in SWAN can be described by a superposition of linear and exponential wave growth terms:

$$S_{in}(\sigma,\theta) = A + B\,E(\sigma,\theta) \tag{2.1}$$

in which E is energy density over relative frequency σ and propagation direction θ. The linear growth rate A, is based on the expression proposed by Cavaleri and Malanotte-Rizzoli (Cavaleri and Rizzoli, 1981) and is generally important during the early stages of wave growth. There are two different formulations for the coefficient B in the exponential wave growth term in WAM-3 and WAM-4. In WAM-3 the rescaled version of the experimental formulation of Snyder is employed (Komen et al., 1984; Snyder et al., 1981) whereas in WAM-4, a set of equations presented by Janssen (Janssen, 1991) is used. The latter formulation is based on quasi-linear theory of wave generation, and the energy exchange from wind to wave is taken into account by interaction of atmospheric boundary layer and sea surface roughness length (Janssen, 1989).

The white capping formulations implemented in SWAN for WAM-3 and WAM-4 are given as:

$$S_{wc\_WAM3} \equiv -C_{ds}\left(\frac{\tilde{k}^2}{\tilde{s}_{PM}^2}E_{tot}\right)^n\left(\frac{k}{\tilde{k}}\right)^m \tilde{\sigma}\,E(\sigma,\theta) \tag{2-2}$$

$$S_{wc\_WAM4} \equiv -C_{ds}\left[(1-\delta)+\delta\left(\frac{k}{\tilde{k}}\right)^{m}\right]E_{tot}^{2}\,\tilde{k}^{3}\,k\,\tilde{\sigma}\,E(\sigma,\theta) \tag{2-3}$$

in which $\tilde{k}$, $\tilde{\sigma}$ and E_{tot} denote the mean wave number, mean frequency and total energy respectively. Moreover, $\tilde{s}_{PM}=\sqrt{3.02\times10^{-3}}$ denotes steepness of the P-M spectrum. The parameters $n=2$ and $m=1$ are fixed in the original model, and the main tuning coefficients are C_{ds} and δ which are conventionally determined to reproduce H_s; resulted from a fully developed P-M spectrum. There are some recent studies that shows WAM-3 can perform better in terms of the T_a estimation, when $m>1$. However, it also leads to overestimation of H_s (Rogers et al., 2003; van der Westhuysen et al., 2007). In this study, a similar investigation is made for WAM-4 to evaluate the effects on the simulated bulk wave parameters, by using higher order wavenumber terms in the white capping sink term. While having some fair support from measurements (Kraan et al., 1996; Lafon et al., 2004), the original $n=2$ in Equation 2-2 was originally introduced by Komen (Komen et al., 1984) for a fully developed spectrum. Because the steepness of the spectrum would not change in such an asymptotic condition, choosing any different value for n was equivalent to redefining the coefficient C_{ds}. This is not the case for a "young sea" in which the steepness of the wave field is evolving. Thus, the effect of higher order dependence of the dissipation term on the steepness is also worthy of investigation. Our initial numerical efforts showed that using $n<2$ could initiate numerical instabilities in shallow waters, that persist for long time periods. Therefore, only larger values of n were further pursued.

The tuning coefficients pertaining to white capping were determined by comparing the bulk wave parameters with *in situ* observations (see Figure 1.1 for station locations). Since wave hindcasting is critically dependent on the accuracy of wind data (Janssen, 2008; Sarkar et al., 2000), the quality of the input model wind used in the modeling was carefully analyzed. The NARR wind data for the period 15-31 March 2007 were shown to be very consistent with measured wind at all available stations (Siadatmousavi et al., 2011a) and therefore were used for the model calibration.

A total of 16 different configurations, as listed in Table 2.1, were used to evaluate the performance of WAM formulations in SWAN. For the WAM-3 formulation, the calibration was based on the bisection method on the parameter C_{ds} (Burden R.L and Faires, 2001). In order to compare the simulations, the H_s Scatter Index (Equation 1.5) was calculated for each station. The average of SI (ASI) from all stations was used as a measure of performance, and the calibration was terminated when ASI changed less than 0.1%. The WAM-4 formulation is a function of C_{ds} and δ. The parameter δ was changed from 0.1 to 0.9 (0.1 increment) and the bisection method on the parameter C_{ds} was used to determine the minimal ASI. The optimal

values of tuning parameters were determined for each case and are presented in Table 2.1. Note that the values for n and m are assumed.

Table 2.1: List of model setups and the optimal values used for tuning white capping parameters Cds and δ.

	Case name															
Parameter	W3-1	W3-2	W3-3	W3-4	W3-5	W3-6	W3-7	W3-8	W3-9	W4-1	W4-2	W4-3	W4-4	W4-5	W4-6	W-Mix
n	2	2	2	3	3	4	4	5	5	---	---	---	---	---	---	2
m	1	1	2	1	2	1	2	1	2	1	0.5	1	1.5	2	2.5	---
Cds	2.36	1.2	1.14	0.76	1.06	0.46	0.99	0.28	0.85	4.5	2.0	1.75	1.5	1.0	0.75	2.02
δ	---	---	---	---	---	---	---	---	---	0.5	1.0	0.8	0.8	0.8	0.7	0.0

The simulated bulk wave parameters during an active cold front season, from December 2007 to the end of April 2008 were compared with NDBC buoys and WAVCIS stations. Several cold front events as well as intermittent fair weather (calm) periods provided a realistic verification environment for the performance of SWAN using optimized tuning parameters already determined from the calibration process discussed above.

Finally, it is interesting to compare the performance of the wave model with generally accepted saturation spectra and asymptotic fetch limited wave growth curves (Booij et al., 1999; Rogers et al., 2003; Tolman and Chalikov, 1996; van der Westhuysen et al., 2007). The idealized wave growth was performed with the structured 1-D non-stationary formulation of SWAN. The reference depth was assigned as 3000 m to ensure deep water condition for all resulting wave fields. In addition, the wind speed was considered to be 15 m/s over the entire computational domain. This value was the average wind speed in the database used to develop the P-M spectrum. Moreover, the median fetch relevant to the P-M (MFPM) database was approximately 350 (km) (Moskowitz, 1964).

There are several available formulations based on asymptotic wave conditions. The growth curves of Young and Verhagen (Young and Verhagen, 1996a) suggest a set of equations that compares well with available data for both young and developed sea states, and are based on measurements from Lake George, Australia. That database was revisited by Breugem and Holthuijsen (Breugem and Holthuijsen, 2007) and some outliers were removed due to coastline effects. The resulting growth curves are reduced to P-M values for H_s for long fetches and those of Kahma and Calkoen (Kahma and Calkoen, 1992) in fetch-limited condition. The JONSWAP experiment (Hasselmann et al., 1973) also provides high quality fetch limited wave growth database. The data were carefully studied by Kahma and Calkoen (Kahma and Calkoen, 1992) and the highly variable wind data were removed to decrease the scatter of the dataset around the regression line. Kahma also provided another regression relationship for wave growth parameters in unstable conditions, based on Bothnian Sea measurements (Kahma, 1981; Young, 1999). We took advantage of the revised formulations by Breugem and Holthuijsen (Breugem and Holthuijsen, 2007), Kahma and Calkoen (Kahma and Calkoen, 1992), and Kahma (Kahma,

1981) as well as the saturation level data from the P-M spectrum to evaluate the performance of different WAM formulations in the Gulf of Mexico.

2.3 Results and Discussion

Quantitative calibration results of SWAN's performance, based on the averaged scatter index (ASI) for bulk wave parameters, are shown in Figure 2.1. The cases W3-1 and W4-1 composed of the conventional default values suggested for WAM-3 and WAM-4 formulations respectively, based on the ability of the model to reproduce the P-M spectrum (Komen et al., 1994). The rationale in implementing all other model optimization simulations was to reproduce the *in situ* H_s with minimum ASI. Although all optimized H_s values are close, W3-4 and W3-5 cases resulted in slightly better agreement with measurements. The WAM-4 formulation performed significantly better in terms of T_a which is consistent with previously reported underestimation of T_a using WAM-3 (Ris et al., 1999). Using the quadratic wavenumber term instead of the linear form in the WAM-3 formulation, also suggested by Rogers (Rogers et al., 2003), addressed this problem (e.g. comparison of W3-2 and W3-3). This result is not surprising, because the higher order wavenumber terms in white capping formulation dissipates more energy in higher frequencies, resulting in lower mean frequency, or equivalently, higher T_a. The changes in $\tilde{k}$ and $\tilde{\sigma}$ further enhance this dissipation process.

Increasing the power of the steepness term in WAM-3 had negative impacts on bulk wave parameters when $n>3$ was used. A slight improvement in H_s was attained, using $n=3$ in Equation 2-2 in conjunction with either a linear or second order wavenumber term in the white capping sink-term; however, it also resulted in poorer results for T_a and T_p. Using higher order wavenumber terms in WAM-4, white capping formulation also yielded slightly better H_s estimations (best result was found for W4-5), however, leading to poorer results pertaining to T_a. Finally, the W-Mix case showed the best T_p estimation, and also better T_a estimation than all WAM-3 cases.

The performance of the model using different formulations with well-tuned calibration, were verified using an independent time period that lasted for five months. The verification results illustrated in Figure 2.2 confirm that the Equation 2-2 yields more realistic simulated T_a using the second order wavenumber term. It also validates the earlier conclusions regarding better performance of WAM-4 formulation in simulating T_a, and slightly better performance of W3-4 and W3-5 in simulating H_s. Similar to calibration results, case W4-5 yields better H_s prediction among WAM-4 formulations, and the W3-5 case shows the best H_s prediction among all cases. The better performance of W-Mix case as compared to all WAM-3 runs, in terms of T_a, shows that a significant portion of underestimation in wave period underscores inferior performance of the wind input formulation used in WAM-3 when compared to that used in WAM-4. Again, the W-Mix case also demonstrates the best T_p estimation.

The SI of wind speed at 10 m above the surface (U_{10}) at all *in situ* stations and SI of H_s resulted from case W4-3 is plotted in Figure 2.3. The stations are ordered based on their depth. A

slightly higher SI factor is obtained at shallow stations than at deep water stations; however, even at stations with water depths deeper than 120 m, which satisfy the deep water condition for T_p<12 sec, SI is high. Therefore, the ASI of H_s shown in Figure 2.2 is not a critical function of the depth of stations used in this study. Therefore, shallow water wave processes have minor effects on the model accuracy; which appears to be mainly controlled by wind accuracy.

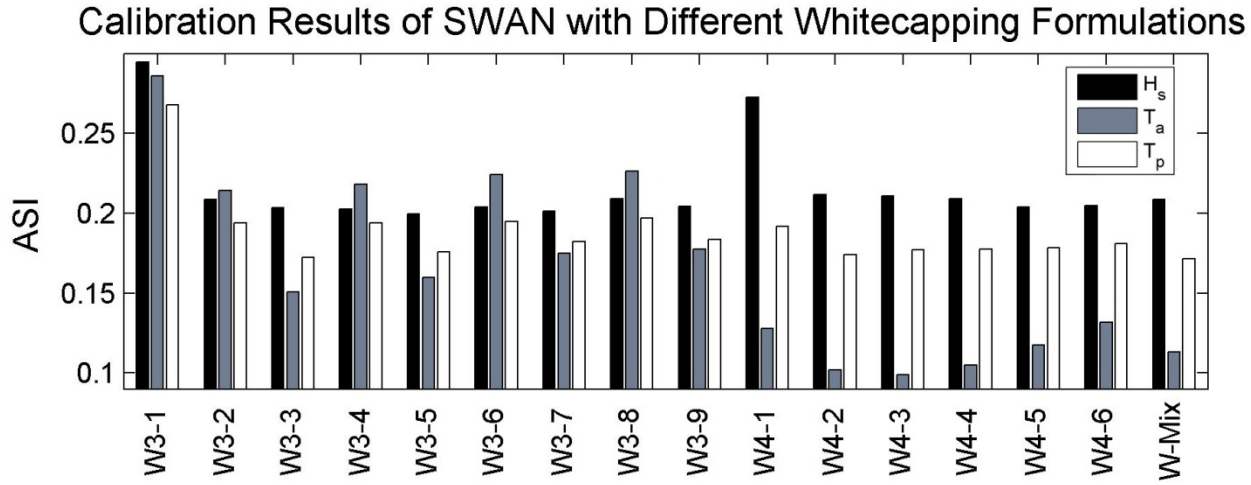

Figure 2.1: Calibration result of SWAN using white capping parameterizations provided in Table 2.1.

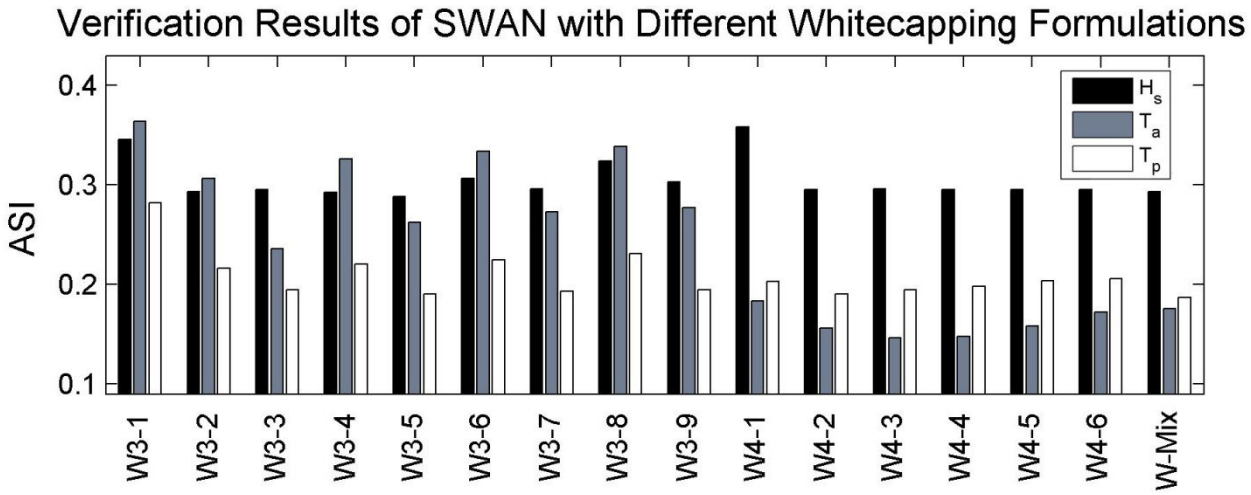

Figure 2.2: Verification result of SWAN using white capping parameterizations provided in Table 2.1.

It is also worthy of note that SWAN using the WAM-4 formulation, is approximately 30% more computationally expensive than the WAM-3 formulation. If the total time needed to

perform nonlinear interaction is considered as reference time t_{nl}, the white capping dissipation term in SWAN requires slightly more than $0.3t_{nl}$ using the WAM-3 or WAM-4 formulation. However, the wind input term in WAM-3 in SWAN requires of the order of $0.2t_{nl}$ whereas WAM-4, which is 10 times more computationally intensive, requires approximately $2.3t_{nl}$.

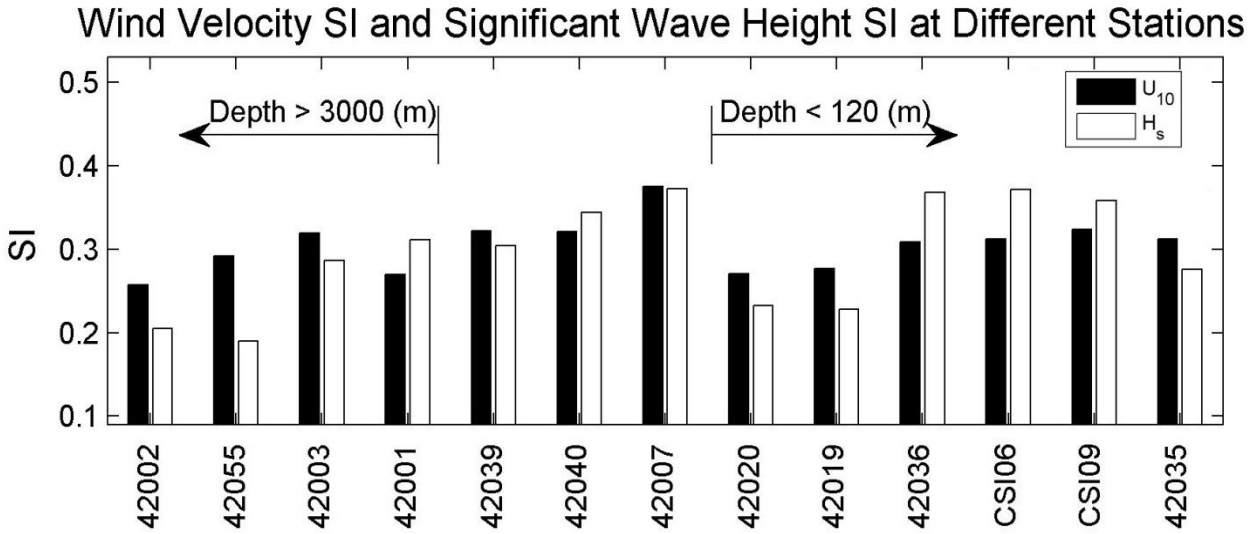

Figure 2.3: Scatter Indices of wind speed and significant wave height (based on case W4-3) at different stations in Gulf of Mexico during the verification period. The stations are ordered from left to right based on depth.

The effects of increasing the power of wave steepness as a function of bias of bulk wave parameters are depicted in Figure 2.4, for several representative WAM-3 alternatives. Panel (A) shows that case W3-2 (default value for steepness power) works well for wave heights larger than 1.4 m. However, case W3-4 predictions are slightly better for H_s smaller than 1.4 m which constitutes 68% of wave records used in the analysis. Therefore, over the entire wave record from all stations shown in Figure 1.1, case W3-4 outperforms the other cases. Panel (B) shows that case W3-2 performs better over a larger portion of the wave period range. As shown in Panel (C), W3-2 also shows a significantly smaller bias for T_a than all other cases. Therefore, increasing the coefficient *n* in Equation 2-2 consistently increases the bias in bulk wave parameters.

The effects of increasing the power of the wavenumber term in the white capping formulation of WAM-4, based on the bias of simulated bulk wave parameters, are presented in Figure 2.5. Panel (A) and (B) show that the modification has minor effects on the model performance in terms of H_s and T_p. The default value m=1 (case W4-3) works well for H_s larger than 1 m; however for smaller wave heights, case W4-2 leads to better model performance. Panel (B) shows that T_p is only affected for T_p<5 sec and decreasing the coefficient *m* in

Equation 2-3 results in slightly less bias. Although case W4-2 surpasses all other cases in T_p performance, case W4-5 has much less bias for T_a from 3.5 to 6 sec which constitutes 87% of the wave record. It also performs well for longer wave periods; while for smaller periods, W4-2 result in the minimum bias. Increasing the coefficient *m* in Equation 2-3 can ameliorate T_a underestimation for wave periods larger than 3.5 sec, although decreasing the coefficient *m* can enhance the model results for smaller wave periods. Also, it is noteworthy that the large relative errors in both Figures 2.4 and 2.5 for T_p>13 sec were resulted from a limited number of samples (this occurred only 6 times at all stations altogether) and can be explained in terms of significant overestimation of energy measured by buoys at the low end of the spectrum during calm conditions; as was reported recently by Work (2008).

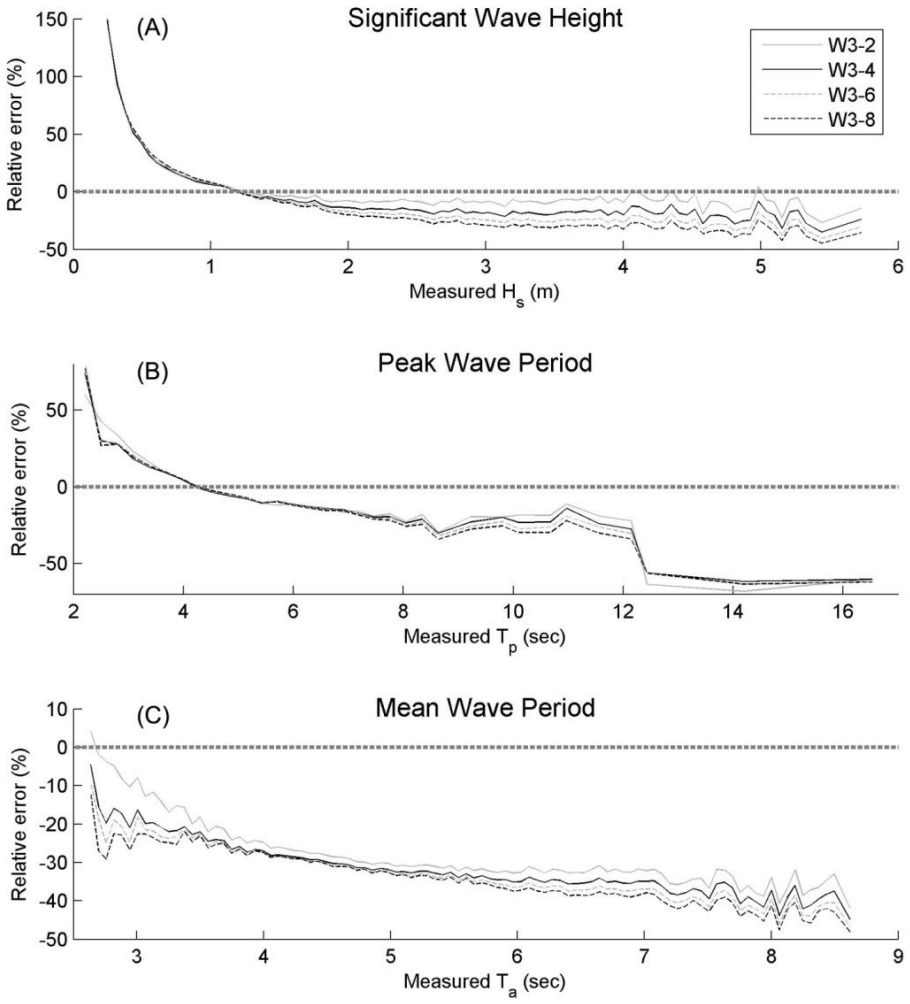

Figure 2.4: The effect of increasing steepness power in the white capping equation of WAM-3 on the simulation of bulk wave parameters. Note that the bias of scatter data was averaged over 0.05 m intervals for H_s, 0.3 sec for T_p and 0.05 sec for T_a, to remove fluctuations and keep the trend.

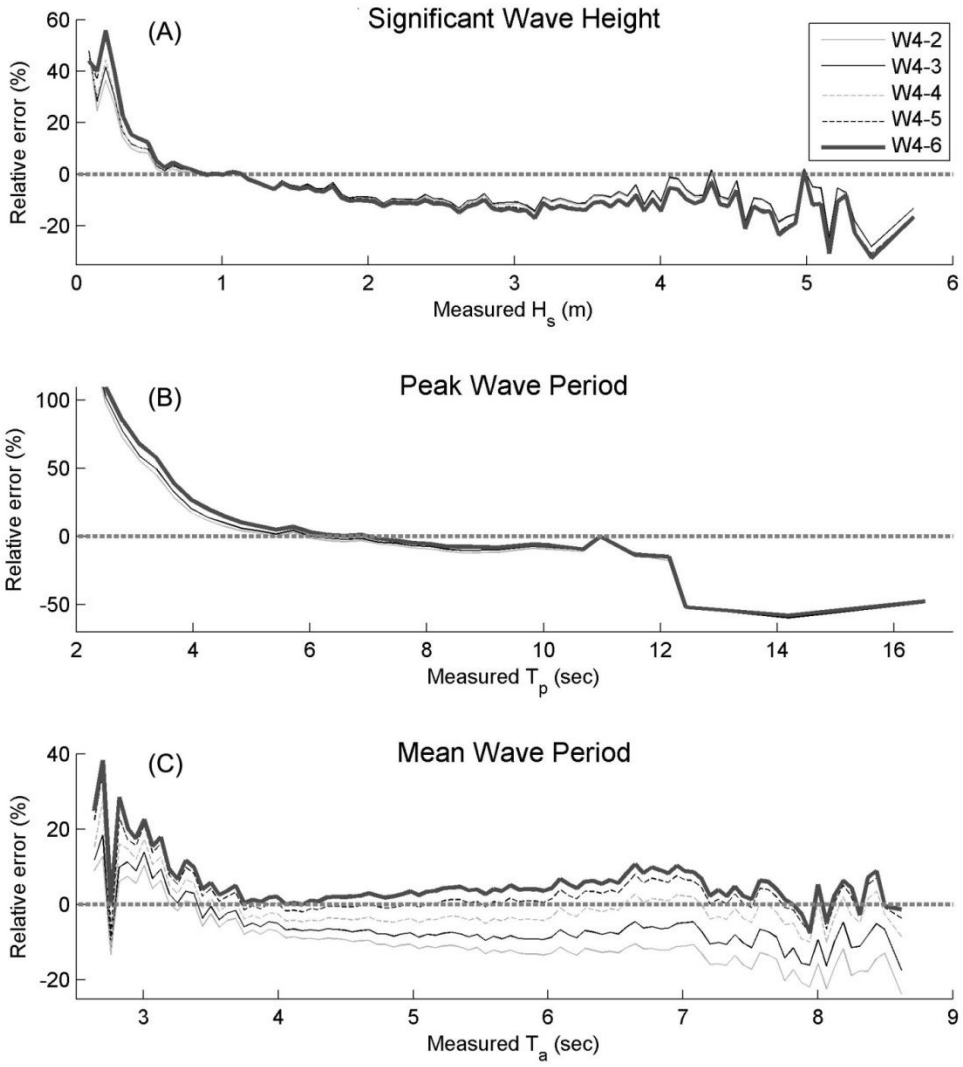

Figure 2.5: The effect of increasing wavenumber power in the white capping equation of WAM-4 on the simulation of bulk wave parameters. Note that the bias of scatter data was averaged over 0.05 m intervals for H_s, 0.3 sec for T_p and 0.05 sec for T_a , to remove fluctuations and keep the trend.

The simulated non-dimensional energy and peak wave frequency using WAM-3 and WAM-4 formulations are skill assessed with different *in situ* idealized wave growth datasets, as shown in Figures 2.6 and 2.7. It is apparent that all parameterizations overestimate the energy level for short fetches; and the overestimation is generally more intense using WAM-3 than WAM-4 alternatives. Moreover, all cases overestimate the peak frequency at MFPM. Comparison between the default WAM-3 (case W3-1) and default WAM-4 (case W4-1) parameterizations for wind input and white capping terms show that default WAM-3 parameterization reaches its saturation level at the fetch which is closer to MFPM. However, the

energy level is lower than P-M. The saturated energy level and also peak frequency are very close to P-M values when using WAM-4, although at a fetch which is one order of magnitude larger than MFPM.

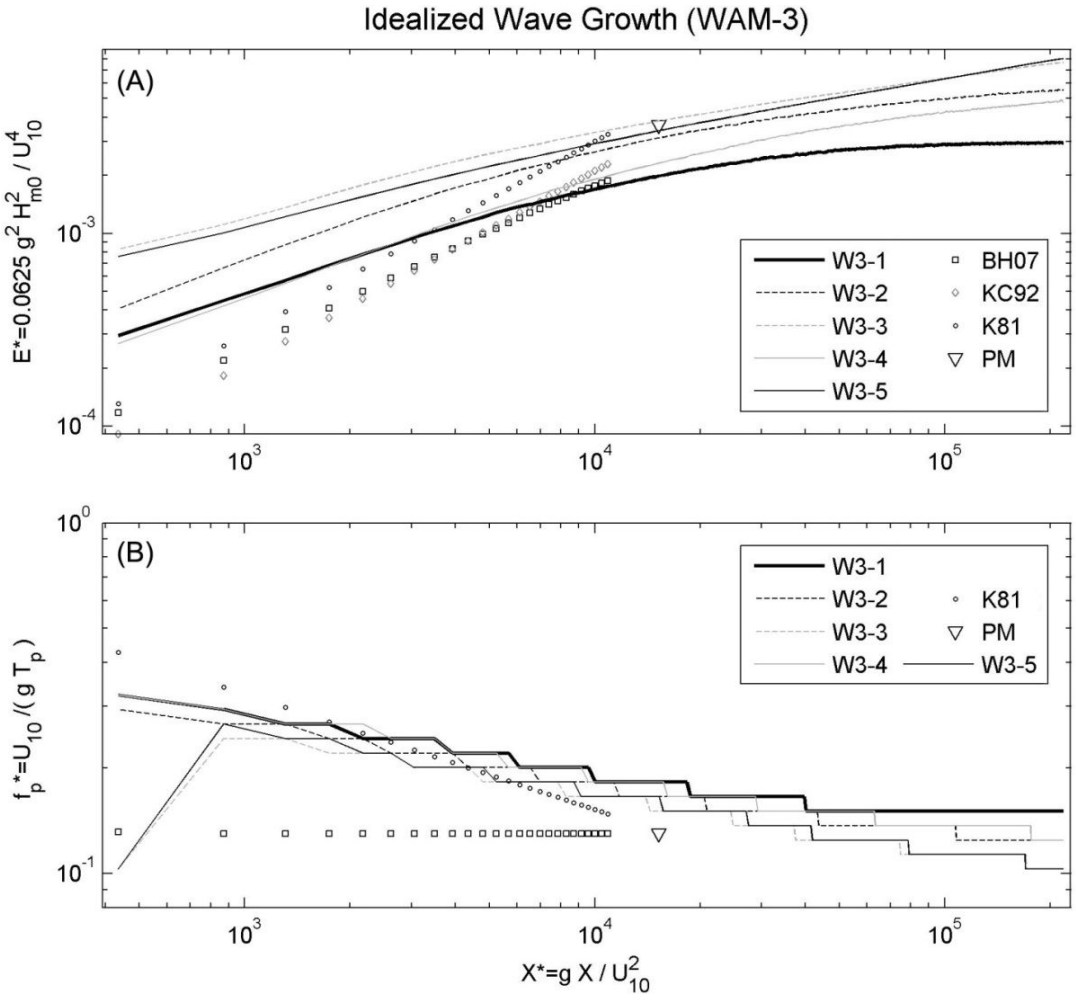

Figure 2.6: Deep water fetch-limited growth curve produced from WAM-3 alternatives and *in situ* measurements of Breugem and Holthuijsen (2007) (BR07), Kahma and Calkoen (1992) (KC92), Kahma (1981)(K81) and Pierson and Moskowitz (1964) (PM). The constant wind speed, U_{10}=15 m/s is used in all cases. The fetch value of X=350 (km) is used for the PM value which is the median of the database used to produce P-M spectrum. Note that the first moment of wave spectrum, H_{m0}, is used to calculate non-dimensional energy which is close to H_s is deep water.

The models calibrated using *in situ* measurements show better agreement with the P-M energy level and peak frequency, while, similar to W3-1 and W4-1, require longer fetch than MFPM to reach the saturation energy levels. Except for W4-5, the rest of WAM-4 formulations

and also the W-Mix case, perform better than WAM-3 formulations in limited fetches. All cases except W3-3, W3-5, and W4-5, lead to good agreement with peak frequency in short fetches; and WAM-3 alternatives (excluding W3-3 and W3-5) result in higher peak wave frequency than WAM-4 alternatives in long fetches.

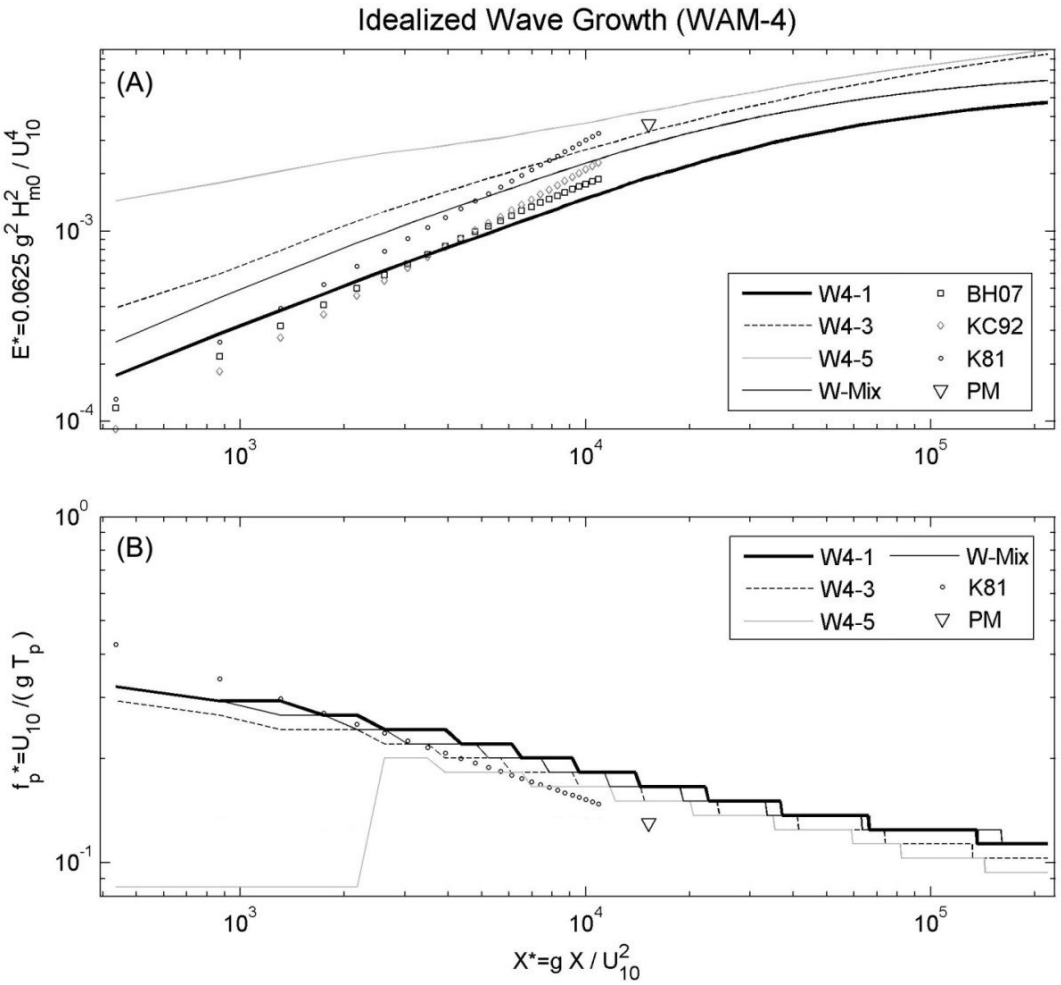

Figure 2.7: Deep water fetch-limited growth curve produced from WAM-4 alternatives and *in situ* measurements of Breugem and Holthuijsen (2007) (BR07), Kahma and Calkoen (1992) (KC92), Kahma (1981)(K81) and Pierson and Moskowitz (1964) (PM). The constant wind speed, U_{10}=15 m/s is used in all cases.

Comparing cases W3-2 and W3-4 reveals that increasing the power of the steepness term can significantly improve the WAM-3 results in short fetches. The energy level computed for long fetches is also in better agreement with the P-M value; however, a longer fetch is needed to reach the P-M energy level. It is also interesting to note that the case W-Mix outperforms all *in situ* calibrated cases in short fetches, and the energy level at MFPM is close to P-M. The

saturation energy level for W-Mix is also close to that of the P-M spectrum. This result again confirms that wind input parameterization plays an important role on model performance, and part of WAM-3's poor to average performance may be a consequence of oversimplifications in the wind input term.

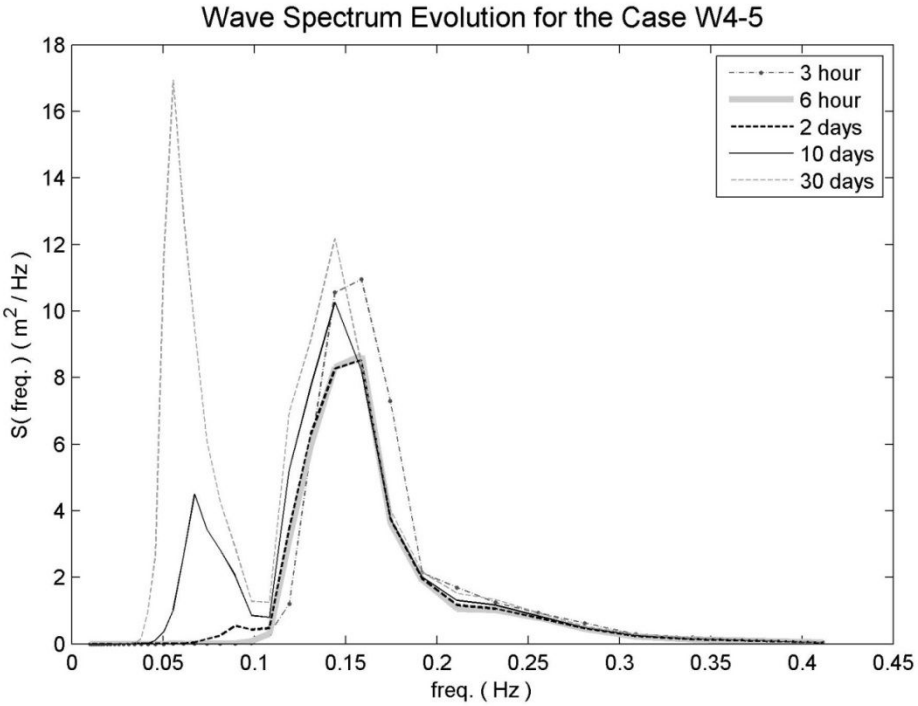

Figure 2.8: The evolution of wave spectrum at X=35 (km) (X*≈1526) for the case W4-5.

Significant overestimation associated with short fetches and high energy gradients over the entire fetch ranges, for the cases with higher order wavenumber terms (cases W3-3, W3-5, W4-5), reveal the inability of these models to reach a saturation level. In addition, these models show peculiarly low peak frequency for short fetch scenarios. The spectrum evolution (e.g. Figure 2.8) explains the reason for both of these abnormal behaviors. The nonlinear wave interaction redistributes energy from peak frequency towards lower and higher frequencies. Increasing the power of the white capping term in Equations 2-2 and 2-3 results in less dissipation in low frequencies, and part of this transferred energy may have been retained with time. The accumulation of the residual energy generates an unrealistic bimodal wave spectrum for wind-sea conditions if the energy transfer from DIA continues (e.g. during steady wind conditions). Since the white capping dissipation is small in low frequencies, there is no mechanism to dissipate the energy of low frequency peak; therefore it continues to grow slowly, and eventually becomes the dominant peak in the wave spectrum as shown in Figure 2.6 for W3-3 and W3-5, and in Figure 2.7 for W4-5.

The time needed for each case to attain the wave growth independent of wind duration, and for a fixed fetch of 350km (X=MFPM), is presented in Table 2.2. The values were determined by seeking the first time step for which both H_s and T_p exceed 95% of their final values (after 30 days). The Moskowitz (Moskowitz, 1964) database used for the P-M spectrum shows the median time equals 12 hours; However, unlike the simulation, the initial conditions were not calm. Hence, all cases except for W3-3, W3-5, and W4-5 are considered to be in good agreement with the Moskowitz measurements. The long durations determined for cases W3-3, W3-5, and W4-5 reaffirms that the energy accumulation at low frequencies deprives the model from reaching any equilibrium stage.

Table 2.2: Time needed for different cases at the fetch equal to MFPM to reach duration-unlimited saturation condition.

Case	W3-1	W3-2	W3-3	W3-4	W3-5	W4-1	W4-3	W4-5	W-Mix
Time (Hours)	15	14	139	15	305	17	174	375	15

2.4 Conclusions of Chapter 2

Based on the work presented in this chapter, the following summary and conclusions are presented:

Parallel unstructured mesh implementation of the third generation wave model, SWAN, was used to compare the performance of the most common formulations of white capping and wind input, WAM-3 and WAM-4. Traditionally, the model parameters were calibrated using bulk wave parameters of fully developed conditions such as the P-M spectrum; however, in order to avoid the recent criticism associated with this approach, in this study the model was first calibrated and validated using *in situ* H_s measurements from NDBC buoys and WAVCIS stations from the Gulf of Mexico. This process significantly enhanced the performance of SWAN in the simulation of bulk wave parameters for the Northern Gulf of Mexico.

The calibration process was repeated for several alternatives of WAM-3 and WAM-4 with higher order steepness and wavenumber terms. Although all configurations resulted in a similar level of accuracy for H_s, the performance of SWAN with each configuration was different in simulating wave period and reproducing idealized wave growth spectra.

Increasing the power of the steepness term in the WAM-3 formulation from 2 to 3 (case W3-4) slightly decreased the ASI of H_s and also improved the resulting bias for small H_s and short T_p. However, these changes in ASI and bias were not apparent for H_s larger than 1.4 m. Over the entire wave record, the bias effect was negligible for H_s and T_p; although not the case for T_a hindcasting. Lower values for the power of the steepness term than the default n=2 in the WAM-3 formulation resulted in numerical problems in shallow water, implying that n should be kept in the range of 2 to 3. Surprisingly, the use of n=3 and parameters determined from *in situ*

calibration outperforms the original P-M calibrated WAM-3 case in reproducing fetch-limited growth curves as well as the P-M saturation level for the wave spectrum.

The results show that all WAM-3 alternatives underestimate T_a. Increasing the wavenumber power from 1 to 2 can considerably address this problem by direct dissipation of energy in the high frequency end of the wave spectrum, and indirect effects of changing the mean wavenumber and wave frequency. However, the model is unable to maintain any saturation level, and the spurious energy transfer to the low frequency portion of the wave spectrum could result in a bimodal wave spectrum for steady wind-sea conditions. It is concluded that case W3-3 is more successful than all other cases in the Gulf of Mexico. However, it is not suitable for steady wind conditions. Case W3-4 is recommended for such weather conditions.

The use of m=2 instead of 1 in the white capping formulation of WAM-4 has negligible effects on H_s and T_p. It also enhances the bias of T_a when T_a>3.5 sec. However, it slightly increases the ASI. Incorporation of higher order wavenumber terms in WAM-4 also results in the model being prone to developing a bimodal energy spectrum and unlimited wave growth in unlimited fetch and time duration conditions. Therefore, case W4-3 is the recommended model parameter in the WAM-4 formulation in the Gulf of Mexico.

Although WAM-4 wind input is 10 times more computationally expensive than WAM-3 wind input formulation and results in approximately a 30% extension in total computational time, it enhances the overall performance of the model. The use of WAM-4 wind input formulation in conjunction with WAM-3 white capping formulation was the most successful combination in hindcasting T_p. It also outperforms all WAM-3 alternatives in the estimation of T_a, while avoiding the potential spurious bimodal spectrum observed using *in situ* calibration of the WAM-4 dissipation term. Indications are evident that the wind input formulation also plays an important role in the performance of wave models, and part of their below par performance can be resolved by modifying the wind input term instead of the white capping term.

CHAPTER 3: ON THE IMPORTANCE OF HIGH FREQUENCY TAIL IN THIRD GENERATION WAVE MODELS[2]

3.1 Introduction

As explained in section 2.1 several packages have been suggested for energy transfer from wind to waves and wave energy dissipation, to be implemented in third generation wave models. Equations 2-2 and 2-3 show that the dissipation of energy in both WAM formulations is a function of mean wavenumber and steepness. The dependence of wave dissipation on mean wavenumber and steepness in WAM formulation resulted in erroneous over-prediction of wind sea in the presence of swell waves (van der Westhuysen et al., 2007). The field evidences do not confirm the enhanced growth of wind sea in combined sea-swell environment (Ardhuin et al., 2007; Young and Babanin, 2006). To solve this problem, van der Westhuysen et al. (2007) suggested a nonlinear saturated-based white capping equation which was entirely local in the frequency domain (Westhuysen hereafter). Their package also included the wind energy transfer of Yan (1987) which was in better agreement with observations than Snyder et al. (1981) during strongly forced waves. Tolman and Chalikov (1996) suggested two different mechanisms for dissipation of energy in the high and low end of the spectrum. In their source package (TC hereafter) the low frequency dissipation term was based on the analogy with turbulence, while an empirical formulation was used for the high frequency constituents. The energy transfer formulation of Chalikov (1995) and Chalikov and Belevich (1993) was employed in TC, which takes into account energy transfer from waves to wind when the waves move faster than wind or travel at a larger angle to the wind direction.

Nonlinear wave interaction is another active process that controls the shape of the wave spectrum, especially during rapid growth of waves. As its name implies, nonlinear wave interaction is not at all local in the frequency domain; i.e., computation of nonlinear energy transfer for a specific frequency component f_i, requires information about energy content at frequencies higher and lower than f_i. However, in order to numerically compute the nonlinear term, a third generation model needs to compute source/sink terms on a limited number of frequency components. To calculate the energy transfer due to quadruplet wave-wave interaction at f_i, DIA requires energy level at 0.75 f_i and 1.25 f_i. Because the forward face of a typical spectrum is steep, the assumption of zero energy for frequencies lower than the first frequency component (f_1), is justifiable if f_1 is selected small enough. The recommended value for f_1 is 0.03-0.04 Hz (Janssen, 2008). However, wave energy decays slowly at the rear face of the spectrum. Therefore, beyond the highest frequency considered in the prognostic region of the wave spectrum, f_H , a diagnostic frequency tail is added in third generation wave models.

---

[2] Reprinted by permission of the Journal of Coastal Engineering (see Siadatmousavi et al, 2012)

This high frequency tail is used to calculate bulk wave parameters as well as the quadruplet wave-wave interaction (Hasselmann, 1988), and has the following general form:

$$F(f,\theta) = F(f_H,\theta)\left(\frac{f}{f_H}\right)^{-n} \qquad for\ f > f_H \tag{3.1}$$

in which θ denotes wave direction, and n is a constant . The main objective of this chapter is to evaluate the sensitivity of advanced wave models to n and f_H, and thereby to provide a good estimation of n, based on skill assessment of the model against data from an array of NDBC buoys in the Gulf of Mexico (shown in Figure 3.1); which in turn would help in eventual optimization of oceanic scale application of well-known third generation wave models.

Several theoretical and experimental studies have been carried out over the last few decades to describe the high frequency end of the spectrum. Phillips (1958) envisaged a saturation upper limit on the spectral level, independent of the strength of forcing wind. In this theory, when the local downward acceleration exceeds *g*, the wave breaks and transfers its energy to turbulence. Based on similarity arguments, it resulted in k^{-3} power law for a one dimensional wavenumber spectrum, and f^{-5} power law for frequency spectrum. Mitsuyasu (1977) found this theory valid for $0.6 < f < 4$ Hz, while the wind speed $U_{10.5}$ was 8 m/s and fetch was 2 km. However, he found f^{-4} relation for $4 < f < 15$ Hz. Kitaigordskii et al. (1975) suggested the incorporation of water depth, h, to Phillips' (1958) theory to make it applicable in shallow water also. Using a similar method, they suggested $h f^{-3}$ would work well for a shallow basin with a mean depth of 4 m. Based on the similarity argument on wave speed, c, instead of acceleration, Thornton (1977) suggested the high frequency tail form of $c^2 f^{-3}$, which can be simplified to f^{-5} power law in deep water and $h f^{-3}$ in shallow water.

Toba (1973) argued that the equilibrium range of spectrum above peak frequency must also depend on wind friction velocity, u_*, and proposed the form of $u_* f^{-4}$. Anctil et al. (1993) observed f^{-4} relation on high frequency band of a NDBC buoy with a 0.5 Hz cut-off frequency. Several other datasets are also available in favor of the f^{-4} relation (Donelan et al., 1985; Kahma, 1981). Based on the existence of the Kolmogoroff-type equilibrium range for water waves, Kitaigorodskii (1983) proposed a theoretical explanation for the f^{-4} tail form. The direct measurements of energy input from wind to waves showed that energy transfer to waves were not concentrated at wavenumbers close to the spectral peak (Snyder et al., 1981), which was in direct contradiction with the assumptions of Kitaigorodskii (1983). The most comprehensive theory in support of the f^{-4} shape was proposed by Phillips (1985) which assumed that deep water source and sink terms were important in the equilibrium range of the spectrum. Also, note that the nonlinear interaction plays an important role in the existence of an ordered high

frequency tail, and tends to maintain an f^{-4} tail form in the absence of other source terms at frequencies higher than $1.5 f_p$ (Resio and Perrie, 1991), in which f_p was the peak frequency of the spectrum.

However, there are some recent studies which are in general agreement with the f^{-5} power law (Banner et al., 1989; Hwang et al., 1996). The high variability in the slope of spectrum at high frequency range was observed in different datasets. Leykin and Rozenberg (1984) measured the frequency spectra from the Caspian Sea up to 10 Hz, and found that the frequency range of 2.4-7.2 Hz follows the power law model with the exponent varying between -3.2 to -4.8. They also claimed a fair agreement with the f^{-4} relation for $1.2 < f / f_p < 3.2$ Hz. Based on recorded wave data from the Great Lakes, Liu (1989) reported that the exponent varied from -3 to -5. He suggested the f^{-4} relation for growing young wind seas and the f^{-3} relation for fully developed spectra. The data from a series of wave gauges established in lake George, Australia, also suggested the use of variable exponents when discussing the spectral evolution (Young and Verhagen, 1996b).

Different explanations were suggested for the uncertainty in the high frequency tail of the wave spectrum. Rodriguez and Soares (1999) attributed this to intrinsically random variability of wind-generated waves. Another group of studies relates the variability of the exponent to the range of frequencies used to determine the power law model. Those studies suggested that close to spectral peak, a f^{-4} power law holds while at frequencies higher than $(2.5 - 3.5) f_p$, the tail maintains a f^{-5} form (Ewans and Kibblewhite, 1990; Forristall, 1981; Hansen et al., 1990; Mitsuyasu et al., 1980; Rodriguez et al., 1999). Banner (1990; 1991), assumed a k^{-4} tail form for two dimensional wavenumber spectrum (corresponding to k^{-3} tail form for an omni-directional wavenumber spectrum), and showed that the change in slope of frequency spectrum could be explained by frequency dependence of the directional spread of energy. He also showed that the Doppler shifting effect caused by orbital velocity of dominant wave component becomes important for $f / f_p > 3$ and may modify the f^{-5} tail shape.

3.2 Third Generation Wave Models and High Frequency Tail

In their pioneering study, Komen et al. (1984) showed the success of third generation wave models in reproducing the saturation spectrum. However they assumed a power law for the high wavenumber end of the spectrum to reduce the computational needs. Use of a different tail power showed insensitivity of the model performance to the value of n used in Equation 3.1 (Komen et al., 1994). This insensitivity of the model results to the tail form was in agreement with studies that demonstrated a weak coupling between the tail of the spectrum and spectral peak (Hasselmann, 1963; Young and Vanvledder, 1993); However, the detailed analysis by Banner and Young (1994) bolstered the importance of frequency tail in the evolution of wave

spectrum. That particular study showed that, as a result of nonlinear wave-wave interaction, the model with an unconstrained tail (with a corresponding large f_H, so that the model would calculate the energy content at frequencies a few times above of the peak frequency) had much more energy in the high frequency end of the spectrum, and hence slower growth close to the spectral peak. Their modeling results demonstrated that variants of WAM dissipation terms could not reproduce reasonable energy in the frequency tail and directional spread simultaneously. The study also concluded that a reasonable estimation from wave model was critically dependent on establishing an artificial diagnostic tail.

The cut-off frequency is determined either statically or dynamically in different third generation wave models. The idea behind dynamic cut-off frequency is to save the computational resources by skipping the calculations for frequencies which are far from the peak frequency. In this study, SWAN with default coefficients for WAM-3, WAM-4 and Westhuysen formulations was used as a representative of the wave models with static cut-off frequency. The highest frequency, f_H, in Equation 3.1 could be set by the user as a constant number (1 Hz and 0.515 Hz were compared in this study). The exponent n in Equation 3.1 is set to $n = 4$ for WAM-3 and Westhuysen formulations in SWAN while $n = 5$ is set for WAM-4 formulation.

The highest frequency f_H in WAVEWATCH-III follows the original WAM dynamic cut-off frequency, and set as maximum of a) 2.5 times the mean frequency of current wave spectra, b) 4 times of the mean frequency of the Pierson and Moskowitz (1964) frequency. The first limit was used for young seas, and equilibrium range was expressed in terms of mean frequency instead of peak frequency because it was numerically more stable. The second limit was designed for fully developed conditions. Moreover the calculated value for f_H cannot exceed the user defined value (the cutoff frequency of 0.515 Hz was used for simulations in this study).

According to Tolman (1992a), the dynamical integration scheme used in WAVEWATCH-III results in a smoother high frequency tail, if $n = 4.5$ is used for the WAM-3 formulation. However, $n = 5$ is the default value for the high frequency part of the spectrum in the TC formulation of WAVEWATCH-III.

3.3 Methods

In order to run SWAN, the unstructured mesh shown in Figure 1.1 is used. A structured grid with spatial resolution of 0.1° (~10 km) was used in WAVEWATCH-III. In both models, directional resolution was set at 10°, and frequency exponential was 1.1 and the lowest frequency was set to 0.035 Hz. The highest frequency close to 0.5 Hz is a typical choice for present-day wave forecasting systems (Janssen, 2008) therefore 0.515 Hz is used as highest cut-off frequency in WAVEWATCH-III. However, for SWAN, it is suggested to use 1 Hz as the cut-off frequency (SWAN team, 2010). Therefore two sets of simulations were performed with SWAN, using the two high cut-off frequencies, viz., 0.515 and 1 Hz. Moreover, the code of

WAVEWATCH-III was also modified to use WAM-3 with static cut-off frequency, to compare the performance of a model using dynamic and static cut-off frequencies.

Two simulation periods, corresponding to two contrasting high energy met-ocean conditions, were considered in this study to evaluate the performance of wave models with different assumptions for the high frequency end of the spectrum. The first period, 0000 UTC on 22 August 2008 to 2100 UTC on 16 September 2008, includes hurricane Gustav and hurricane Ike, as well as a period of fair weather conditions in between. The tracks of these hurricanes as well as the locations of *in situ* observations are shown in Figure 3.1. The details on Hurricanes Gustav and Ike, and pre-processing of wind data used for wave simulation are presented elsewhere (Berg, 2008; Beven and Kimberlain, 2008; Siadatmousavi et al., 2009). Another longer simulation period, from 0000 UTC on 20 October 2007 to 0000 UTC on 1 May 2008, was also considered to evaluate the performance of models during the passage of extra-tropical winter storms (cold fronts) as well as for the intermittent fair weather (calm). Since the models were initiated with *cold start* conditions, no output from the first two days for the first simulation, and the first 10 days for the second simulation, were used in skill assessments of the models.

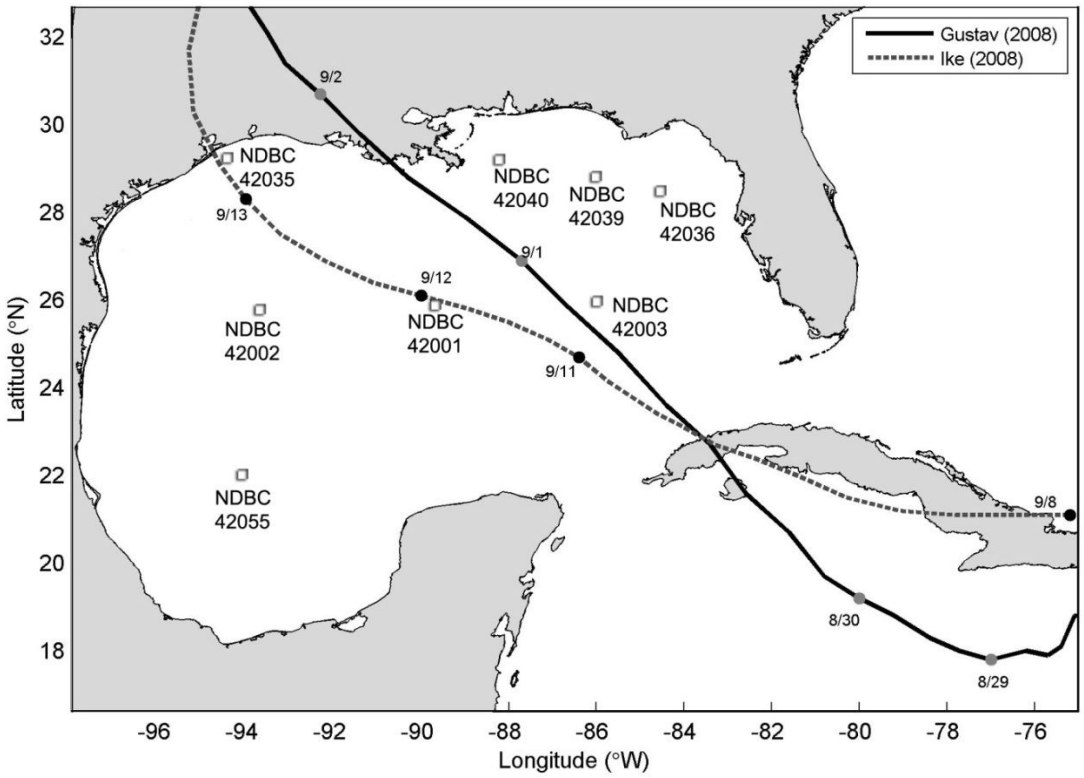

Figure 3.1: The track of Hurricanes Gustav and Ike in Gulf of Mexico and the Caribbean Sea. (Data courtesy: National Hurricane Center). The locations of NDBC Buoys used in this study are also provided.

3.4 Results and Discussion

Significant wave height (H_s), peak period (T_p) and average period (T_a) computed by SWAN for the first time period (hurricane conditions) were compared with data from NDBC 42040 in Figure 3.2. In this case, WAM-3 formulation of SWAN with $f_H = 1$ Hz and n=4 and n=5 as tail exponents, were used.

Note that T_{m02} (square root of the ratio between zero- and second-moment of frequency spectrum) was used to estimate T_a, from the wave spectrum. To be consistent with *in situ* observations, all bulk wave parameters were estimated based on the wave spectrum up to 0.485 Hz.

The wind speed used for simulation and the measured wind speed at the buoy location (NDBC 42040) are provided in panel (a), for reference. As shown in panel (b), when H_s<1 m, the simulated H_s was significantly affected by the exponential term in Equation 3-1. In this lower range of H_s, WAM-3 performs better with n=5 rather than n=4. Panel (c) shows the same improvement in terms of T_p prediction using n=5 in fair weather conditions. Panel (d) confirms that T_a shows a systematic increase when using n=5, rather than the default value n=4.

In Figure 3.3 spectral evolutions are compared for the two frequency tail configurations against *in situ* measurements from NDBC buoy 42040. It is clear that spectra simulated by both model configurations are too wide compared with the buoy measurements. However, n=5 leads to more realistic and narrower distribution of energy, especially the energy levels at the high frequency end of the spectra are lower for n=5. As shown with more extended contour lines over the frequency band of 0.15-0.25 Hz, the wave energy is dissipated with slower pace for n=5 than n=4, which is in accordance with buoy data shown in panel (c).

Changing the exponent n from 4 to 5 resulted in the same effects on the bulk wave parameters and wave spectrum at all stations shown in Figure 3.1, when using the WAM-3 formulation. In order to demonstrate the effects of the change in high frequency shape on the model's performance at all measurement locations, it is ideal to use some statistical parameters. Although the Scatter Index (SI), root mean square error (RMSE), correlation coefficient (R^2) and bias are the most common statistical parameters used to evaluate the performance of wave models over the years (Alves et al., 2002; Ardhuin et al., 2010; Janssen, 2008), these parameters are best for the description of average behavior of models over an extended period of time; or for a dataset with some sort of similarities. The first simulation period encompasses both fair weather and two severe hurricane conditions; while the overall performance of the wave model, covering both energetic and calm weather conditions, was the main interest of this study. In addition, it is better to avoid separation of these two conditions, because it would make the outcome of the analysis subjective to the criteria used for such a separation. Therefore, a normalized RMSE (NRMSE) is used to measure the overall performance of the wave model in both calm and severe weather conditions. The following definition is used for NRMSE in this study:

$$NRMSE = 100 \times \sqrt{\frac{1}{N}\sum_{i=1}^{N}\left(\frac{X_{Oi} - X_{Mi}}{X_{Oi}}\right)^2} \qquad (3.2)$$

in which X_{Oi} and X_{Mi} denote ith data resulted from observation and model respectively, and N is the total number of data points. Note that the data with observed H_s below 0.3 m were removed before calculating statistical parameters, to avoid any sensitivity to division by small numbers, as well as low signal-to-noise ratio for the data measured at such a calm weather conditions.

For all NDBC stations shown in Figure 3.1, which did not fail during the passage of Hurricanes Gustav and Ike in 2008, the statistical parameters were computed from SWAN simulations, using the WAM-3 formulation with n=4 and n=5, and presented in Figure 3.4. The bulk wave parameters were calculated based on instrument cut-off frequency which was at 0.485 Hz for buoys. Using n=5, instead of n=4, could systematically decrease the NRMSE and bias of T_a at all stations. It also lowered the NRMSE of T_p and H_s due to better predictions during fair weather conditions. The use of n=4 resulted in negative bias (under estimation) of T_p in all stations but n=5 partially fixed the underestimation of T_p. Note that the H_s bias was not markedly affected by the change in the power of high frequency tail; and in terms of NRMSE, in all stations, n=5 resulted in better agreement with *in situ* measurements.

The mean value of Bias and NRMSE for the result of SWAN using different formulation at all stations are presented at Figure 3.5. It illustrates that the interaction of the high frequency end of the spectrum and the performance of the wave model depends not only on the formulations used for wave dissipation and energy tranfser from wind to waves, but also on the assumptions for high frequency cut-off used in the model.

Surprisingly, the use of a static cut-off frequency of $f_H = 0.515$ Hz, instead of the default value of 1 Hz, in SWAN using WAM-3 markedly improves both $\overline{Bias}$ and $\overline{NRMSE}$ for all bulk wave parameters. However, when the WAM-4 or Westhuysen formulations of SWAN were employed, little improvement was observed in term of $\overline{NRMSE}$. The more constrained tail ($f_H = 0.515$ Hz) resulted in a lower bias of T_a, but in some cases slightly increased the bias of T_p when compared with corresponsing higher cut-off frequency case ($f_H = 1$ Hz).

Among different formulations for SWAN, the WAM-3 formulation was more sensitive to the exponent used in the frequency tail equation; and the use of n=5 resulted in better performance of the wave model than n=4. However, the WAM-4 formulation offered slight improvement only for T_a in terms of $\overline{Bias}$ using n=5 instead of n=4. The statistical indicators computed for all bulk wave parameters showed that the combnation of $f_H = 0.515$ Hz and n=5 also results in the best agreement with measurements for both WAM-4 and Westhuysen formulations.

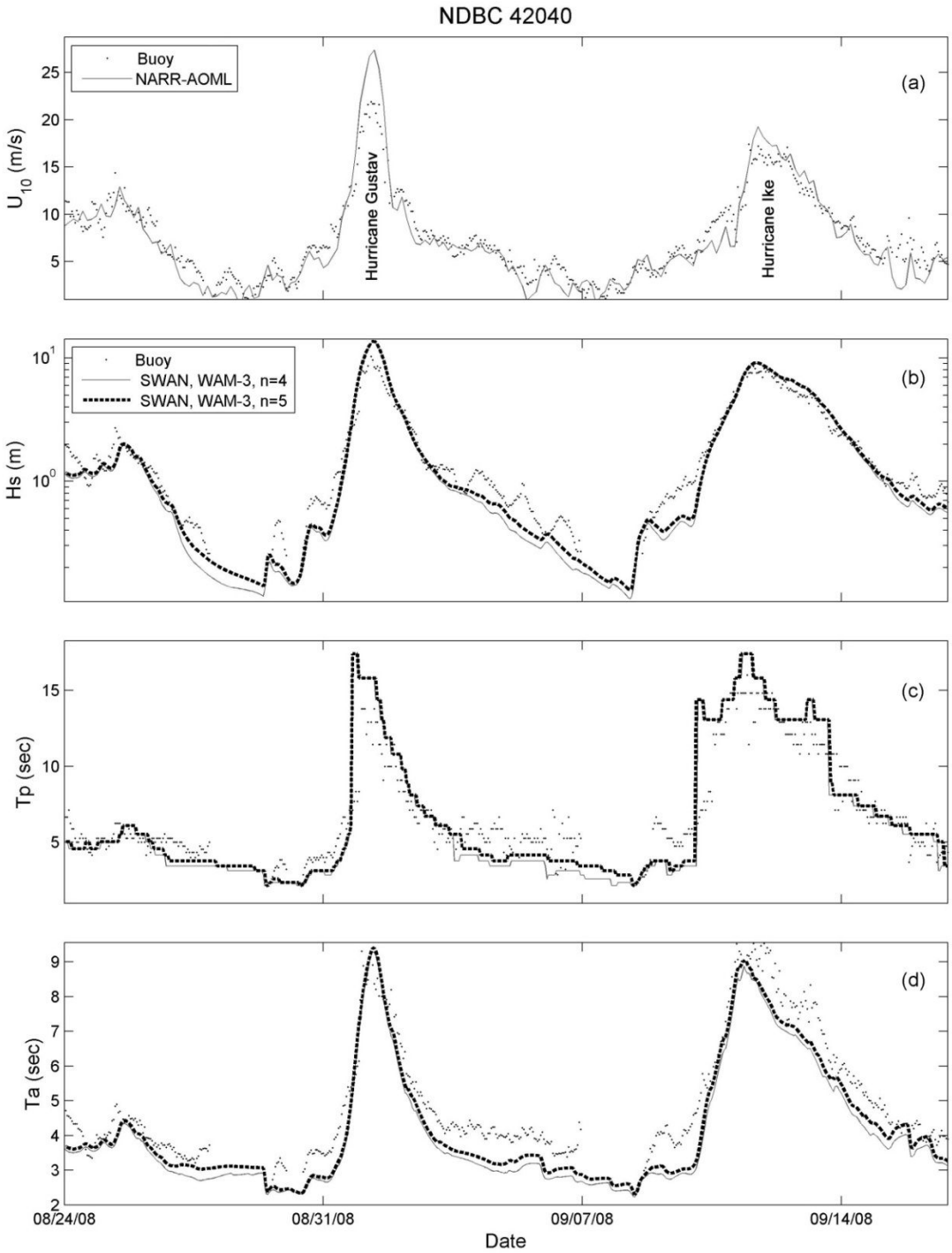

Figure 3.2: Skill assessment of WAM-3 formulation of SWAN using n=4 and n=5, in terms of bulk wave parameter; using *in situ* data from NDBC 42040: a) time series of wind speed at 10 meter above sea level plotted against a high resolution blended wind (AOML H* wind and NARR/NCEP); (b) Significant wave height; (c) Peak wave period; (d) Average wave period. Note that a logarithmic scale is used for wave height to show the performance of wave model in both severe and calm weather conditions.

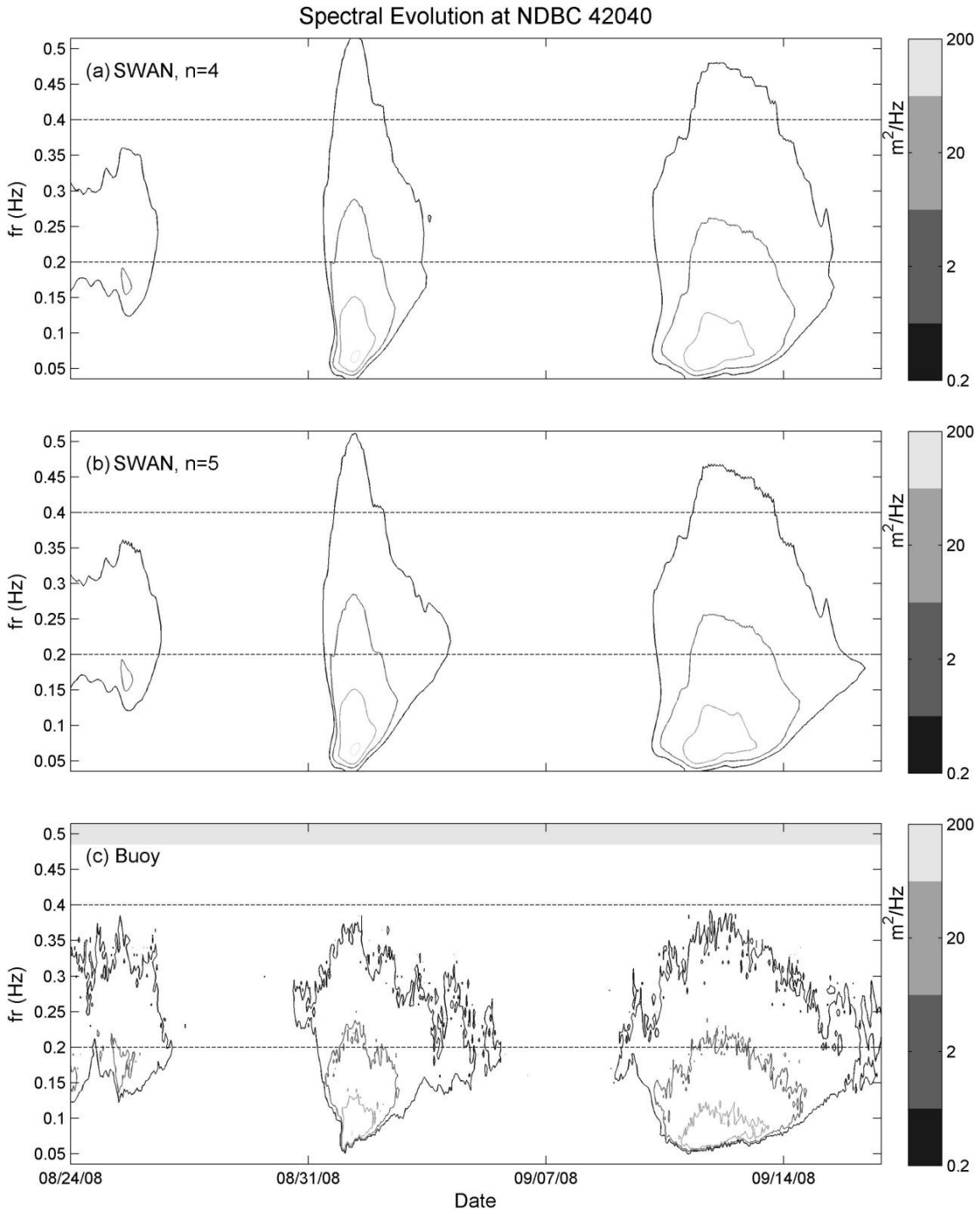

Figure 3.3: The spectral evolution computed at NDBC buoy 42040 for the first time period (2008 Hurricane conditions) for a) SWAN with WAM-3 formulation and exponent of n=5 in tail formula; b) SWAN with the WAM-3 formulation and exponent of n=4 in tail formula; c) spectra measured by the buoy. The maximum frequency reported at buoy 42040 was 0.485 Hz. The dash lines at 0.2 Hz and 0.4 Hz were also plotted for reference. Note that the contours are in logarithmic scales.

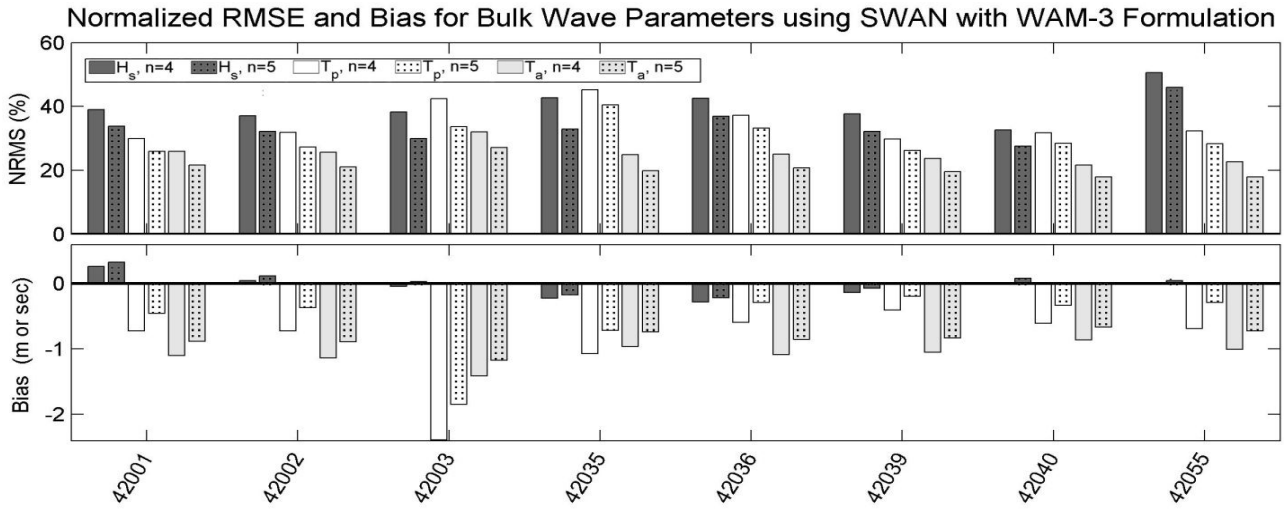

Figure 3.4: The skill assessment of SWAN using the WAM-3 formulation with n=4 and n=5, at all stations, for the first simulation time period, in terms of: a) Normalized root mean square error; b) Bias of bulk wave parameters.

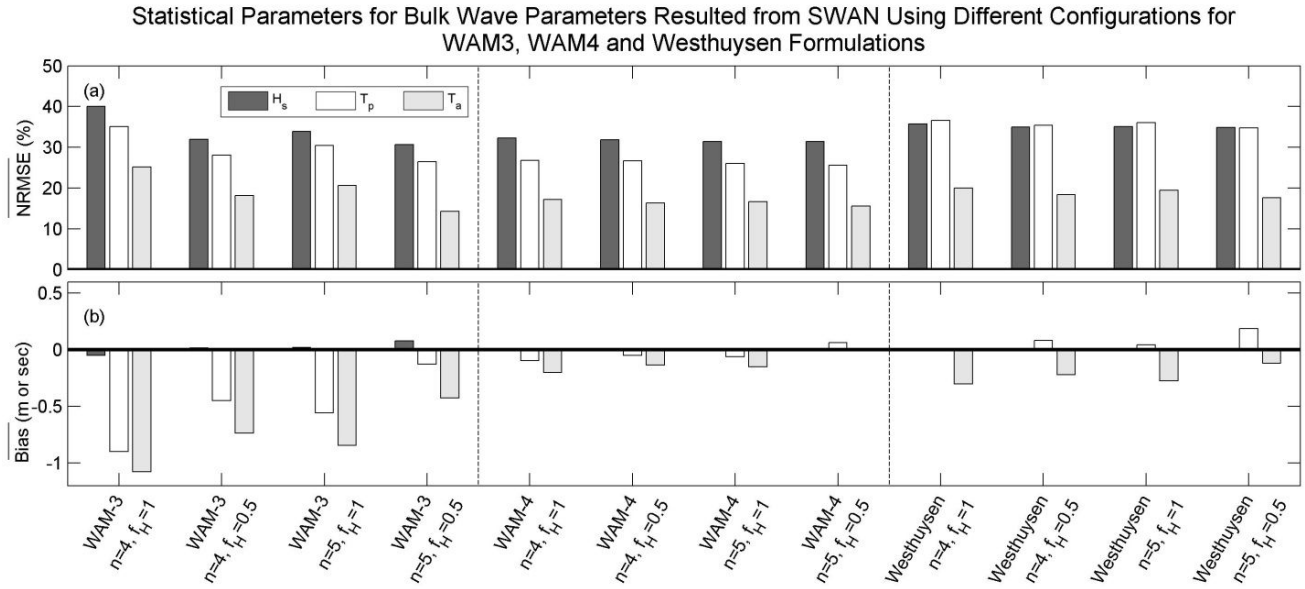

Figure 3.5: The skill assessment of SWAN with different formulations and configurations based on all stations shown in Figure 3.1 during the first simulation time period, in terms of: a) Average of normalized root mean square error; b) Averaged bias of bulk wave parameters.

The performance of these formulations were also evaluated during an active cold front season at Gulf of Mexico; from November 2007 to May 2008. Since the dataset was long enough, the conventional definition of RMSE (Equation 1-4) was used to evaluate the error. The parameter $\overline{RMSE}$ is then calculated based on the average value of $RMSE$ for all available

NDBC buoys (see Figure 3.1). Better performance of SWAN using n=5, rather than n=4, in WAM-3 is apparent from Figure 3.6. Moreover, regardless of the exponent used in the tail formulation, the use of $f_H = 0.515$ Hz rather than $f_H = 1$ Hz resulted in better $\overline{RMSE}$ and $\overline{Bias}$. The use of n=5 in tail form and $f_H = 0.515$ Hz also enhanced the results of SWAN simulations using WAM-4 and Westhuysen formulations, but the improvements were not as conspicuous as in WAM-3.

Note that Figures 3-5 and 3-6 demonstrate that SWAN with the WAM-3 formulation systematically underestimated T_a. The spectrum evaluation in Figure 3.3 shows that the energy levels at the rear face of the spectra were much more than the observed values. This overestimation of energy at the high frequency end of the spectrum is a well-known problem for SWAN using the WAM-3 formulation (Ris et al., 1999). The dissipation term of WAM-3 is a linear function of wavenumber normalized by mean wave number. As discussed in Chapter 2, Rogers et al. (2003) showed that the use of a quadratic dependence of dissipation on wavenumber can partially tackle the underestimation of period. Although this approach was successful for field conditions in which wind speed and direction continuously varied, the use of this method for an idealized case and locally calibrated coefficients for the Gulf of Mexico, resulted in a spurious secondary peak in the front face of the spectrum (see Figure 2.8).

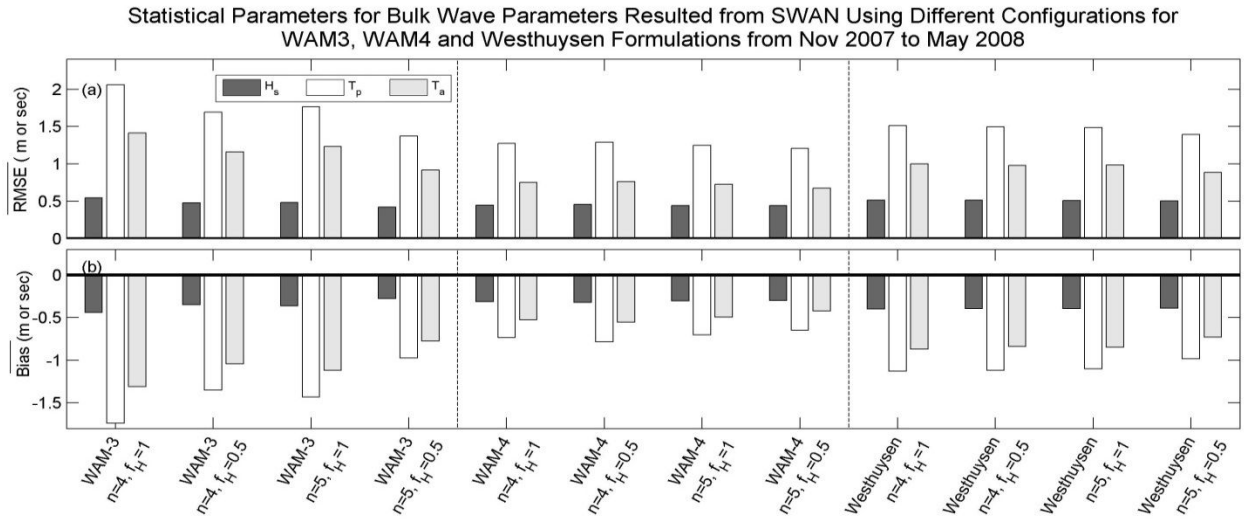

Figure 3.6: The skill assessment of SWAN with different formulations and configurations, based on all stations with available data, during the second extended simulation time period (2007/2008 winter-spring cold front season) , in terms of: a) Averaged root mean square error; b) Averaged bias of bulk wave parameters.

It can be seen from Figures 3-5 and 3-6 that the use of WAM-3 with the n=4 exponent and constant high cut-off frequency, $f_H = 0.515$ Hz, outperformed the same configuration except

with $f_H = 1$ Hz for the Gulf of Mexico. The use of smaller cut-off frequencies resulted in lower energy levels in the tail, and higher energy levels close to the spectral peak compared to the simulation with $f_H = 1$ Hz. Therefore, exclusion of the frequency band 0.515-1 Hz from a prognostic frequency range for model applications could partially ameliorate the underestimation of T_a by WAM-3 formulation.

The other two formulations of SWAN also showed better performance when $f_H = 0.515$ Hz was used as cut-off frequency rather than the default $f_H = 1$ Hz. The better performance of the model using lower cut-off frequency implies that none of the implemented formulations were capable of reproducing the physics of energy exchange and dissipation at the high frequency tail of spectrum. Therefore, more advanced formulations are needed to extend the capabilities of phase averaged models such as SWAN, for the accurate prediction of high frequency gravity waves.

Note that the interaction of rear side of wave spectrum and frequencies close to the spectral peak depends on the formulation used for wind input, and for wave energy dissipation. The spectral evolution resulted from the WAM-4 or Westhuysen formulation was less sensitive than WAM-3, to variability in exponent of the high frequency tail. However, $n = 5$ still resulted in lower energy at the tail end and higher energy level close to the spectral peak, when compared with n=4. The lower sensitivity of those formulations can be explained by higher energy dissipation imposed on the rear side of the spectrum. Therefore, less energy is available for nonlinear interactions, which is a cubic function of the local spectral density function (Phillips, 1985).

The results from the WAVEWATCH-III simulations with a dynamic cut-off frequency of $f_H = 0.515$ Hz and different formulations are provided in Figure 3.7. Note that n=4.5 was used, instead of n=5, in WAVEWATCH-III with WAM-3 formulation, as suggested by Tolman (1992a) to avoid noise in the high frequency end of the spectrum, due to dynamic time step algorithm used in the model. The use of n=4.5, rather than 4, improved the WAVEWATCH-III performance in terms of $\overline{Bias}$ of mean wave period. The $\overline{Bias}$ of T_p was also enhanced while the effects of using n=4.5 on H_s was insignificant.

The code of WAVEWATCH-III was modified such that it used the static cut-off frequency. The results from this modified model simulations are demonstrated in Figure 3.7. Although the error statistics derived from simulations using static cut-off frequency were close to corresponding simulations using dynamic cut-off frequency, the bias was slightly increased for all bulk wave parameters, especially during high energy events.

The TC formulation showed different patterns compared with WAM formulation and worked better with n=4 than n=5; especially in terms of $\overline{NRMSE}$ of wave height. Also the $\overline{Bias}$ was smaller when n=4 for the frequency tail. Note that TC results were worse than WAM-3 for both $\overline{Bias}$ and $\overline{NRMSE}$ of H_s.

The better performance of WAM-3 formulation using n=4.5 in WAVEWATCH-III, rather than n=4, was also confirmed from the extended simulation of the 2007-2008 active cold front season. As shown in Figure 3.8, both $\overline{RMSE}$ and $\overline{Bias}$ for T_a and T_p were in better agreement with observation when higher value for n was used. Moreover, the statistics were close for both static and dynamic cut-off frequency of $f_H = 0.515$ Hz. Unlike WAM formulations, the TC formulation worked better with n=4, as observed for the first simulation period.

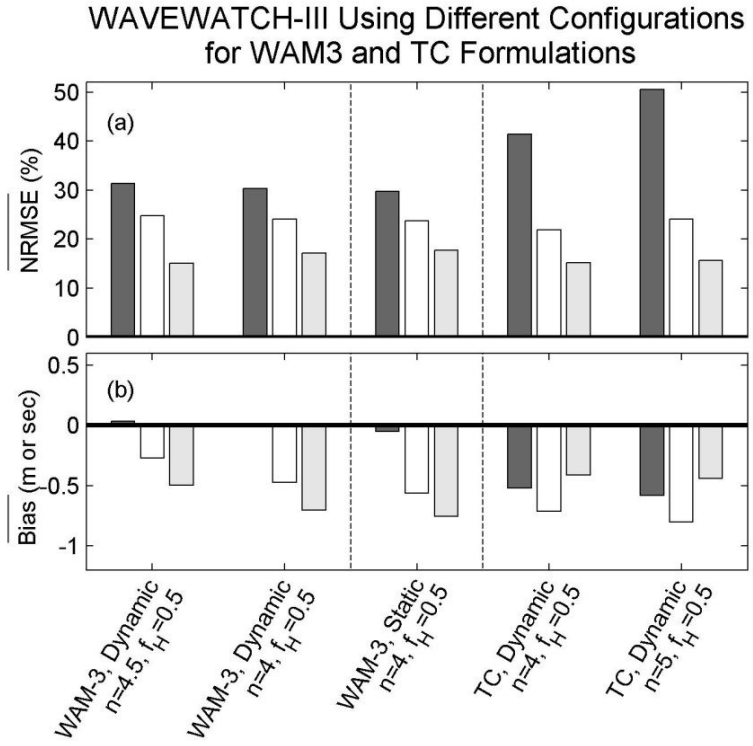

Figure 3.7: The skill assessment of WAVEWATCH-III with different formulations and configurations based on all stations during the first simulation time period, in terms of: a) Average of normalized root mean square error; b) Averaged bias of bulk wave parameters.

As shown in Figures 3.7 and 3.8, the uses of WAM-3 formulation with similar configurations but with a constant cut-off frequency of $f_H = 0.515$ Hz, slightly worsen the performance of the WAVEWATCH-III. It is suggested that the use of a dynamic high cut-off frequency can not only optimize the model calculations, but also improve its performance on oceanic scales, such as for the Gulf of Mexico. According to the definition of dynamic cut-off frequency given in section 3.2, it differs from static one only when 2.5 times of the mean frequency is less than user-defined value for cut-off frequency. Since the peak frequency (and

therefore mean frequency for usual mono-modal spectrums) is inversely related to wind speed (e.g., parametric formulation of Hasselmann et al.(1973)), the mean wave frequency decreases with increase in wave height for wind seas. Therefore, the difference between static and dynamic cut-off frequency becomes more important for energetic events. In order to bolster this finding, the following analysis was pursued.

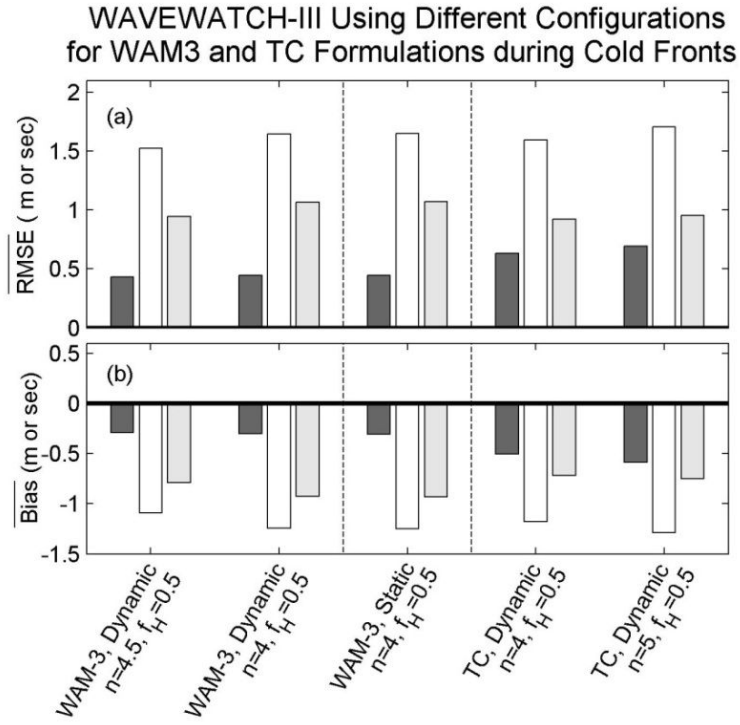

Figure 3.8: The skill assessment of WAVEWATCH-III with different formulations and configurations based on all stations with available data during the second extended simulation time period (2007/2008 winter-spring cold front season) , in terms of: a) Averaged root mean square error; b) Averaged bias of bulk wave parameters.

The difference between H_s and T_a simulated from WAVEWATCH-III, at all NDBC stations shown in Figure 3.1, and using a static and dynamic cut-off frequency of $f_H = 0.515$ Hz, are normalized with simulated bulk wave parameters from model with dynamic cut-off frequency ($H_{s,Dyn}$ and $T_{p,Dyn}$ respectively). The mean value for the change in normalized H_s and T_a , from all *in situ* observations, are plotted in Figure 3.9 against $H_{s,Dyn}$,with a bin size of 0.2 m for $H_{s,Dyn}$. During energetic events, the static cut-off frequency is higher than equilibrium range of spectrum, and nonlinear interaction pumps part of energy beyond equilibrium range. Therefore, the wave spectrum evolves at slower pace during high energy events, when constant cut-off is employed in the model. This result is consistent with the Banner and Young, (1994)

argument on excessive energy transfer to the high frequency tail by the WAM-3 formulation and its slower growth rate when the unconstrained tail was used. As waves become more energetic, the mean frequency decreases and the gap between cut-off frequency and end of equilibrium range increases. Therefore, the difference between two model configurations increases.

It is important to note that the high cut-off frequency is treated as a static value in SWAN, given the fact that this model was originally formulated for shallow water simulations, in which complex wave fields make it difficult to delineate one main active wave system with smooth and a stable dynamic cut-off frequency (Booij et al., 1999). Therefore, for oceanic scales, it is recommended to use dynamic cut-off frequency to decrease the computational cost as well as to facilitate more realistic energy transfer to high frequency tail of the spectrum.

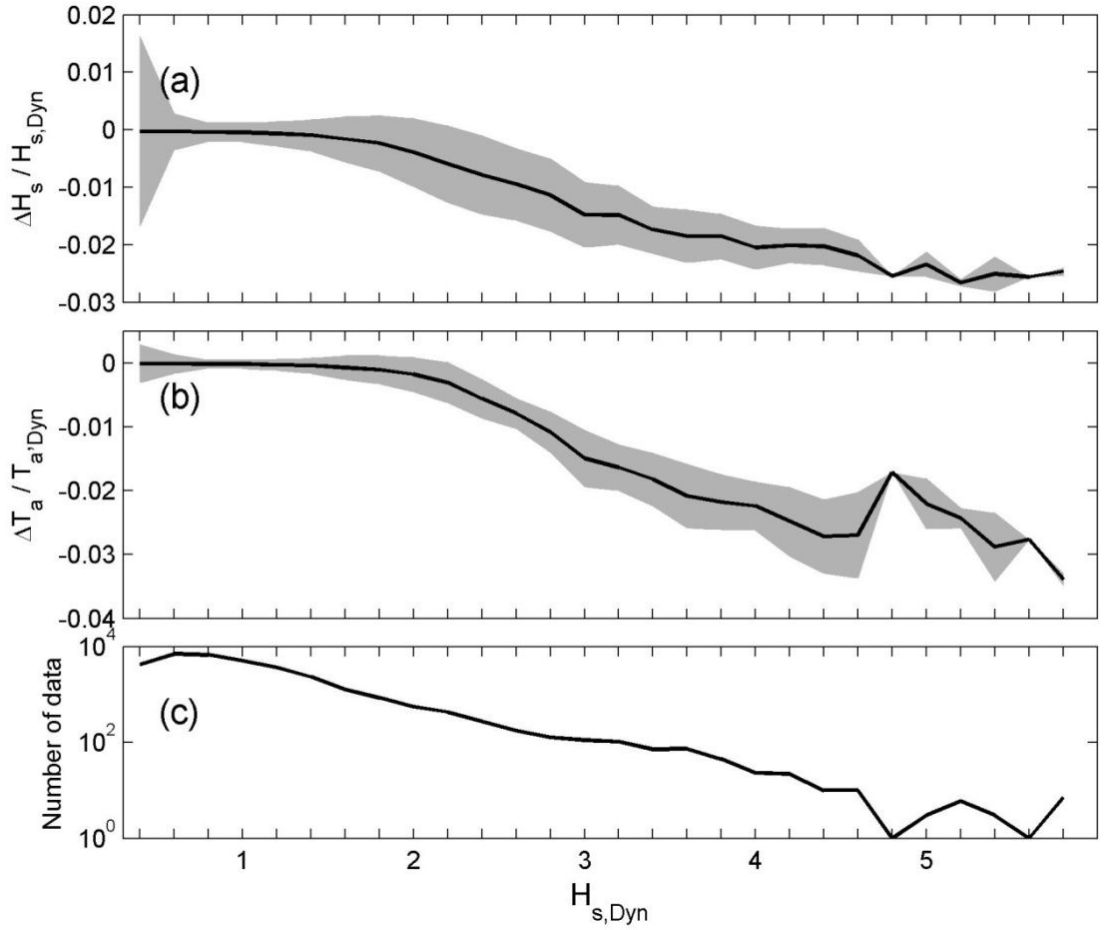

Figure 3.9: a) The difference between simulated wave height from the WAM-3 formulation with dynamic and static cut-off frequency ($H_{s,static}$-$H_{s,dynamic}$) normalized by $H_{s,dynamic}$ versus $H_{s,dynamic}$; b) The normalized difference of T_a versus $H_{s,dynamic}$; c) The number of data points occurred within each bin (bin size was equal to 0.2 m). The shadings show one standard deviation higher and lower than mean value at each bin.

Figures 3.7 and 3.8 also show that the use of $n = 4$, rather than $n = 5$, in TC formulation of WAVEWATCH-III resulted in a better estimation of the bulk wave parameters (especially H_s). The disparity between TC formulation and WAM-3 in WAVEWATCH-III is caused by severe underestimation of energy in low frequencies. Ardhuin et al., (2010) also reported negative bias and low performance of TC formulation in Lake Michigan (see Table 2 in their paper). Based on the good performance of TC formulation in open oceans, they concluded that there is a scale-dependency in TC equations. It was mentioned in section 3.1 that the dissipation term of TC composed of two terms: a low frequency constituent and one dedicated formulation for the contribution of high frequency waves. The difference between the modeled and observed wave spectrum was normalized with the spectral peak of the measured spectra for 2007/2008 winter-spring cold front season, and the mean value was plotted versus normalized frequency in Figure 3.10. As highlighted, the underestimation mainly occurred close to the mean frequency; therefore low frequency constituent of TC dissipation term needs to be adjusted before modifying the tail parameters, which could have secondary effects on the results of simulation.

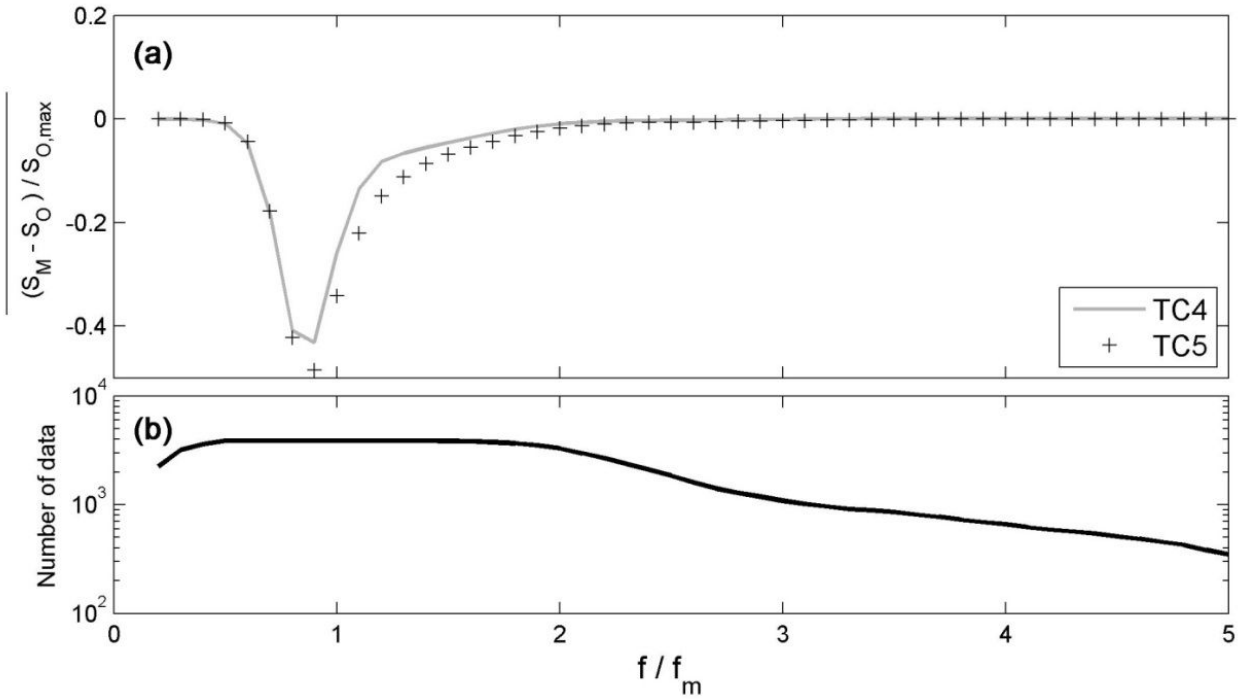

Figure 3.10: a) The average of normalized spectrum bias using TC formulation for the second extended simulation time period (2007/2008 winter-spring cold front season); b) The number of data points occurred within each bin (bin size was set to 0.1).

The directional distribution of energy from model also depends on the formulations used for whitecapping and wind input. To quantify the directional spread of energy, a non-

dimensional directional width parameter can be defined, similar to the spectral width parameter (e.g., Massel, (2007)):

$$\nu_D^2(f) = \frac{\hat{m}_0(f)\,\hat{m}_2(f)}{\hat{m}_1^{\,2}(f)} - 1 \qquad (3.3)$$

in which $\hat{m}_i(f) = \int_\theta \theta^i\, F(f,\theta)\, d\theta$.

When the energy is concentrated in a directionally narrow band within a specific frequency bin, $\nu_D^2 \to 0$ for that frequency bin; otherwise, ν_D^2 increases for directionally broad energy distribution.

The computed directional width parameter at the NDBC 42040 location using SWAN with WAM-3 and WAM-4 formulation, during the hurricane period, is provided in Figure 3.11. The data correspond to WAM-3 (left panels) and WAM-4 (right panels) formulations, at 5 discrete time steps during the passage of hurricanes Gustav and Ike through Gulf of Mexico: the start of intensification of H_s due to Hurricane Gustav (panels a and f); peak H_s of Hurricane Gustav from the simulations, which occurred 3 hours after maximum H_s measured at NDBC 42040 (panels b and g); calm weather window between the two hurricane events (panels c and h); peak H_s of Hurricane Ike, from the simulations, which was again with a 3 hour time lag from the maximum H_s measured at the buoy (panels d and i); and relatively calm conditions after Hurricane Ike (panels e and j). It is clear from all the different scenarios that WAM-3 led to a directionally broader tail as opposed to WAM-4. Moreover, WAM-3 was more sensitive to the change in the exponent of the frequency tail and the selection of f_H.

The use of n=5 in WAM-3 resulted in a reduced energy in the tail, but the change of ν_D^2 at the spectral peak was negligible. However, the use of a lower f_H in WAM-3 broadened the distribution width at spectral peak during calm weather conditions (panel c) and the relaxation phase after the passage of a hurricane (panel e). Note that plots associated with peak waves of hurricanes were truncated before 1 Hz, because the peak energy was several orders of magnitude larger than the tail energy, and the truncated value of normalized energy level was zero at the high frequency tail in SWAN outputs.

Banner and Young (1994) showed that the use of a higher order dissipation term in WAM-3 also results in a narrower directional spreading at the rear face of the spectrum and broader directional spreading near the spectral peak. As shown in Figure 3.11, the suggestion of using lower cut-off frequency or a higher exponent value in the WAM-3 formulation of SWAN resulted in the same behavior at the rear face of the spectrum. However, a lower cut-off frequency also broadened the directional width close to the spectral peak. On the other hand, WAM-4 formulations were not sensitive to decrease in f_H. This feature also can be used to decrease the computational time needed to complete the simulation.

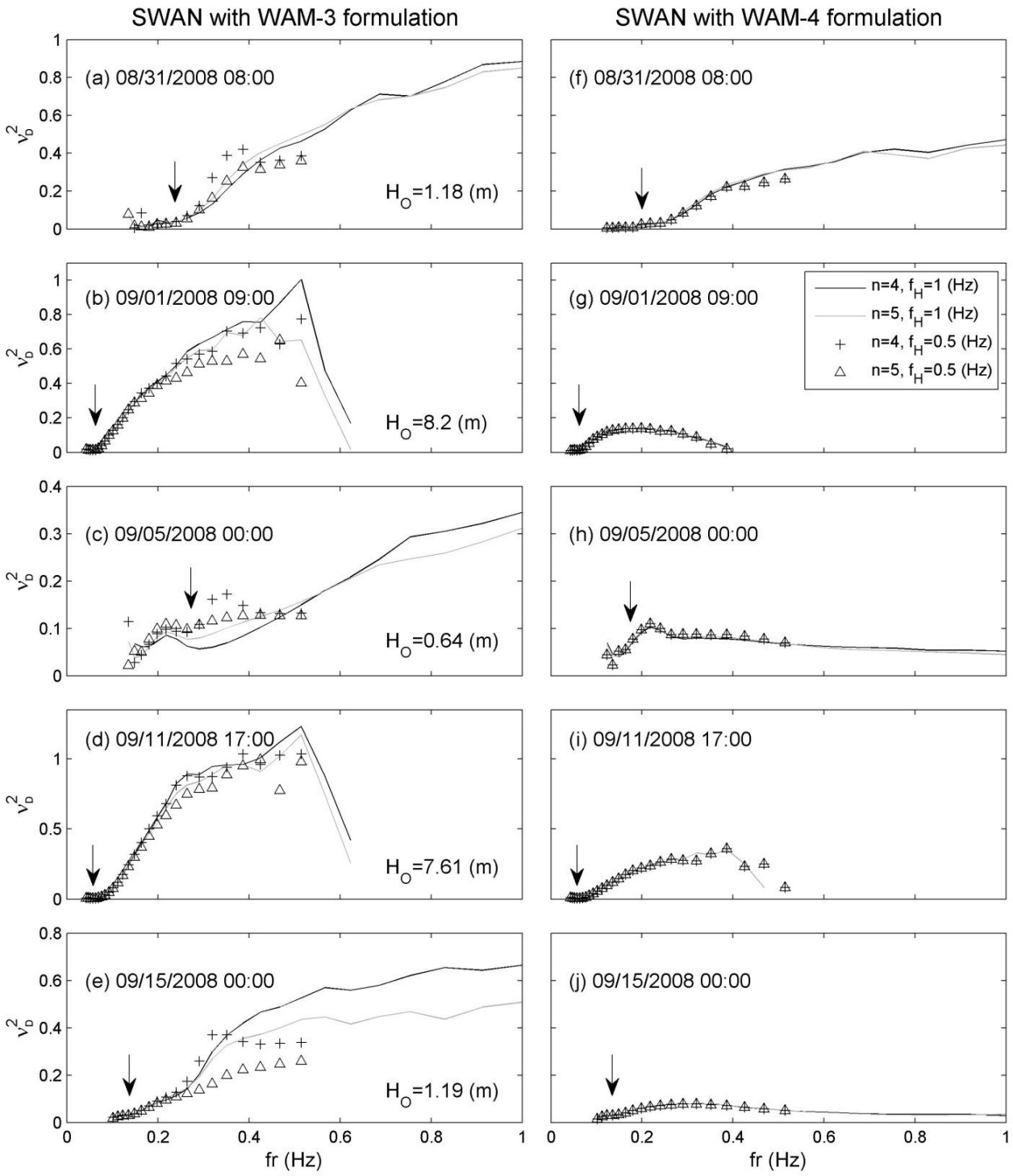

Figure 3.11: The directional width of energy spread for different configurations of SWAN with WAM-3 (left panels) and WAM-4 (Right panels), at different time steps during the passage of Hurricanes Gustav and Ike in 2008; at the location of NDBC buoy 42040. The location of the simulated peak frequency is shown by arrow. The wave heights measured by NDBC buoy 42040 at each time step are also provided in the left panels.

Note that all results presented here shows that the use of n=5 in the model leads to a better agreement with observation. It can be supported by previous studies, that affirmed the validity of theory of Phillips (1958) for the frequency spectrum at frequencies higher than $(2.5-3.5)f_p$; unless it is affected by the Doppler shifting effect. Therefore, it raises a question why SWAN uses n=4 in the high frequency end of wave spectrum with most of its formulations? Note that the original value of the exponent in Equation 3-1 was $n=5$ in original WAM-3 model (SWAMP Group, 1985) and WAM-4 model (Komen et al., 1994). Although not mentioned in the SWAN manual, the value of $n=4$ is more suitable for application in shallow water, in which the exponent is smaller (as discussed in section 3.1). Moreover, SWAN was originally designed for coastal area applications, in which the fetch is limited for most wind directions. There are several parametric wave growth curves for deep water in which peak frequency, f_p, is proportional to X^m, in which X is fetch length and the coefficient m varies from -0.23 to -0.33 (Donelan et al., 1985; Hasselmann et al., 1973; Kahma, 1981). Similar inverse dependency exists for shallow water wave dynamics (e.g., see Figure 7.17 in Young (1999)). Therefore in fetch limited area, the peak frequency is higher, and therefore equilibrium range of spectrum (less than $3f_p$) is more extended. As discussed in section 3.1, $n=4$ is in better agreement with observed data in equilibrium range. On the other hand, the original value of $n=5$ in WAM-4 was not changed. One explanation can be the fact that the calculation of wind induced shear in WAM-4 formulation was reported to be sensitive to the value of n (Komen et al., 1994).

3.5 Conclusions of Chapter 3

Parameter evaluation of SWAN and WAVEWATCH-III models for simulating calm and severe weather conditions in the Gulf of Mexico yielded the following conclusions:

The WAM-3 formulation was very sensitive to the assumed high cut-off frequency and assumed power law for the diagnostic frequency tail. Moreover, the numerical simulations confirmed better performance of the model with n=5 in the diagnostic tail in terms of bias and root mean square error of bulk wave parameters. Hence, in oceanic scales, the use of n=5, rather than the default value of n=4, is recommended for SWAN.

The use of WAM-3 formulation for wind input and whitecapping dissipation in wave model resulted in too much energy in the frequencies beyond the equilibrium range of spectrum which was the main reason for a well-known underestimation of average wave period. Therefore, in oceanic scale wave modeling, the use of the more limited range ($f_H = 0.5$ Hz rather than $f_H = 1$ Hz) for prognostic part of the wave spectrum is suggested for SWAN when WAM-3 formulation is employed.

The use of WAM-3 in WAVEWATCH-III with a dynamic high cut-off frequency slightly outperformed the corresponding simulation using constant high cut-off frequency, when implemented for the Gulf of Mexico. This result indicates that, to use SWAN in the oceanic

scales, the implementation of dynamic cut-off frequency can not only decrease the computational cost but also enhances the simulation results.

The WAM-4 and Westhuysen formulations in SWAN for simulations conducted in the Gulf of Mexico were least affected by the exponent used for the exponential tail form or the assumed high cut-off frequency. This feature can be used to optimize the time needed to perform a simulation by using a lower f_H, and compensate for more calculations needed for a wind energy term of WAM-4; or whitecapping term of Westhuysen formulation when compared with corresponding formulation of WAM-3. The higher dissipation imposed on the rear side of the spectrum in these formulations resulted in a reduced energy level in the frequency tail, even when prognostic region of the wave spectrum is extended to 1 Hz. The low energy content in the high frequency end of the spectrum indicates less energy exchange by nonlinear wave interaction; which could explain narrower energy distribution in the rear side of the WAM-4 simulated spectrum, when compared with WAM-3 results.

The non-WAM formulation of WAVEWATCH-III, proposed by Tolman and Chalikov (1996) package with its default values for its free parameters resulted in considerably too strong energy dissipation for the Gulf of Mexico. A new calibration process is needed to remedy the underestimation of wave height simulated by this formulation.

CHAPTER 4: THE EFFECTS OF BED FRICTION ON WAVE SIMULATION: IMPLEMENTATION OF AN UNSTRUCTURED THIRD-GENERATION WAVE MODEL, SWAN[3]

4.1 Introduction

When waves propagate across intermediate and shallow waters, wave transformation processes such as bed friction become important. In shallow water, bed friction is as important as nonlinear wave-wave interaction (Graber and Madsen, 1988). Bed friction dissipates the energy transfer toward lower frequencies due to nonlinear wave interactions, which leads to the shift in the spectral peak toward higher frequencies (Graber and Madsen, 1988). While several different formulations have been proposed to include the bed friction effect in wave models, the simplest approach referred to as the JONSWAP model (Hasselmann et al., 1973) is generally used due to its simplicity. This formula has been reported successful under many practical conditions (Tolman, 1994). In addition, many wave models' dependence on bottom sediment size distribution is weak for small domains, such as those having a few kilometers in length and width (Kagan et al., 2008). Moreover, the JONSWAP formula is not a function of bed lithology/fabric characteristics, which makes it more practical to use for large scale simulations, where a uniform distribution of sedimentological data may not be available for the entire domain.

Since a reasonably good sediment classification study has been completed by the U.S. Geological Survey (USGS) for the northern Gulf of Mexico (usSEABED), it offers a unique opportunity to take advantage of these field measurements to run well-calibrated wave models with more complex bed friction formulations and the opportunity to evaluate the importance of bed formulation in their performances. The usSEABED project is a joint effort between the United States Geological Survey (USGS) and the University of Colorado, resulting in a compilation of seafloor sediment characteristics around the United States from the beach to the deep waters. The data source includes surficial and sub-bottom data from physical sampling equipment (grabs and cores) and virtual sampling such as descriptions based on interpretations of seafloor photographs. The database has already proven to be very effective in Louisiana coastal ecosystem restoration programs as well as in sediment mobility studies (Buczkowski et al., 2006).

Among different bed friction models, the Madsen drag law formulation has been proven to be one of the most accurate bed friction dissipation models that depends on near bottom orbital velocity as well as bed roughness (Madsen et al., 1988). Although considered to be computationally expensive compared to the JONSWAP method, unlike most eddy viscosity

[3] Reprinted by permission of the Journal of Coastal Research (see Siadatmousavi et al, 2011a)

equations, it scales with friction velocity (Luo and Monbaliu, 1994). This scalability makes it more appropriate to use in the wave action balance equation in third generation wave models such as SWAN (Janssen, 2004; Komen et al., 1984; Rogers et al., 2003).

The purpose of this chapter is to determine the effects of inclusion of the bed grain size distribution in model on the simulated wave height. Depending on the goal of wave simulations, quantification of the difference between two bed friction formulae can be studied by either incrementally changing the mean wave height over a relatively long period of time (Georgiou and Schindler, 2009; Nielsen, 1992) or changes to the wave height during an extreme high energy event. The former criterion is useful for long-term response studies such as sediment transport while the latter is more important in studies of hurricane impacts on offshore structures and along the coastline. An additional objective of this study is to perform simulations over a time period of a few discrete cold front passages during Spring 2007 as well as for an active cold front season, from Dec. 2007 to Apr. 2008, for the first approach, and during Hurricane Dennis (2005) pre-landfall met-ocean conditions for analyzing the second approach.

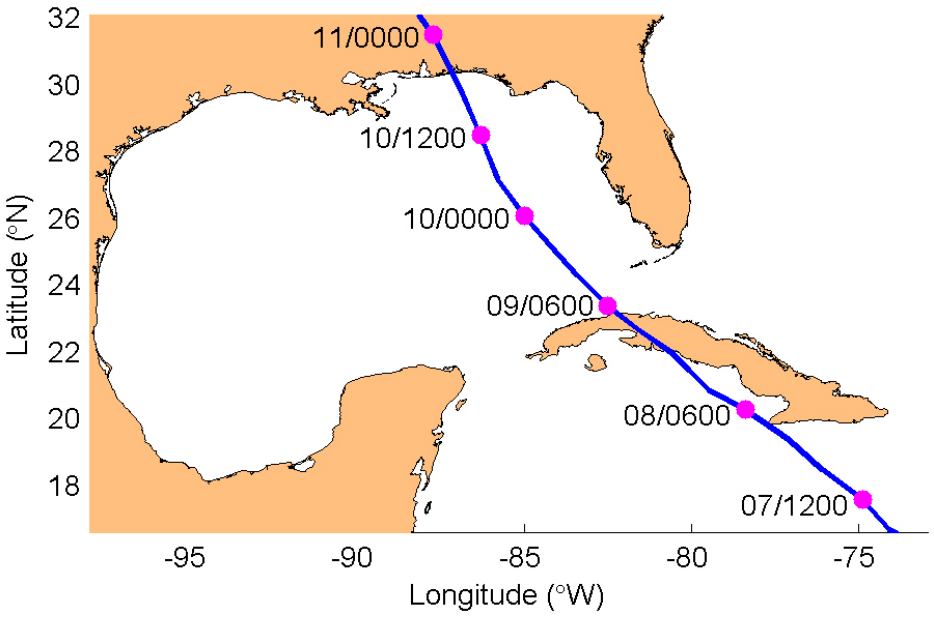

Figure 4.1: The track of Hurricane Dennis in Gulf of Mexico (Data courtesy of Beven, 2006).

Although August and September are generally the most common months for Atlantic hurricanes to form (Grenci and Nese, 2006), Dennis originated from a tropical wave on 29 June, 2005 and transformed into a tropical depression on 4 July 2005 near the southern Windward Islands, in the Caribbean. While moving northwestward it intensified and became a tropical storm on 5 July and later reached hurricane status on early 7 July 2005. Hurricane Dennis

reached Category 4 status before making two successive landfalls in Cuba (see Figure 4.1) with sustained wind speed of 222 km/h (120 kts) on 8 July 2005. It weakened considerably after crossing Cuba and emerged in the Gulf of Mexico at 0900 UTC on 9 July 2005 as a Category 1 hurricane. As it tracked northward, Dennis strengthened after being significantly influenced by warmer waters from a well-established Loop Current in the eastern Gulf of Mexico, and again became a Category 4 hurricane on 10 July 2005 with wind speeds attaining 241 km/h (125 kts). Due to mid/upper level dry air, Dennis weakened to a category 3 hurricane before final landfall at Navarre Beach, along Santa Rosa Island, Florida, at 1930 UTC on 10 July 2005 (Beven, 2006; Morey et al., 2006).

4.2 Methods

The general spectral form of the bed friction term can be expressed as:

$$S_{bot}(\sigma,\theta) = -C\frac{\sigma^2}{g^2 \sinh^2 kh} E(\sigma,\theta) \tag{4.1}$$

in which $E(\sigma,\theta)$ is the two dimensional frequency spectrum, σ is angular frequency, θ is the direction of the wave component, k is the wave number, and h is local water depth. Coefficient C depends on the friction model used for the computation and in the simplest model, JONSWAP method, can be considered as the constant value: $C_{JONSWAP} = 0.038$ (Hasselmann et al., 1973). Our sensitivity analysis shows that a 100% increase of $C_{JONSWAP}$ can result in a 5-10% decrease in simulated H_s in coastal stations shown in Figure 3.1; i.e. WAVCIS stations CSI06 and CSI09 as well as NDBC buoys which are relatively closer to the coastline, such as 42007, 42019, 42020 and 42035. It has been shown that the coefficient C in Equation 4.1 is not constant and depends on wave-induced bed velocity (Young and Gorman, 1995). For example, it can be evaluated from more complex models such as the eddy-viscosity model of Madsen et al. (1988) in which the following set of equations are solved:

$$C_{MADSEN} = \frac{g}{\sqrt{2}} f_w U_{rms} \tag{4.2}$$

$$U_{rms} = \sqrt{\iint \frac{\sigma^2}{g^2 \sinh^2 kh} E(\sigma,\theta)\, d\sigma\, d\theta} \tag{4.3}$$

where U_{rms} is the root mean square bottom orbital velocity. Since the flow is usually assumed to be turbulent (Tolman, 1992b), the friction factor f_w can be solved by iteration from the following set of equations (Jonsson, 1967)

$$\frac{1}{4\sqrt{f_w}} + \log_{10}\frac{1}{4\sqrt{f_w}} = m_f + \log_{10}\frac{a_b}{K_N} \tag{4.4}$$

$$a_b = 2\sqrt{\iint \frac{1}{\sinh^2 kh} E(\sigma,\theta)\, d\sigma\, d\theta} \qquad (4.5)$$

in which a_b is the near-bottom excursion amplitude (Madsen et al., 1988), $m_f = -0.08$ is constant (Jonsson and Carlsen, 1976) and K_N is the bed roughness height and depends on the sediment properties. The term K_N is of the order of $1-10d_{50}$ for flat beds, in which d_{50} is the median sediment grain size, and of the order of $100d_{50}$ in ripple beds (Nielsen, 1992). Moreover, the K_N values ranging between 2 and 5 cm were proved to result in satisfactory performance of wave models (Tolman, 1991). Assuming the average value of $K_N = 4\ cm$ for typical sand with a mean grain size of 0.2 mm, and a linear relationship between K_N and d_{50} lead to $K_N = 200d_{50}$, which is the relationship selected in this study. The constant value of 200 used in this study is also very close to the average of the data shown in Figure 3.6.4 of Nielsen (1992). Moreover, the lowest and highest possible values for K_N were set to 0.1 cm and 10 cm respectively. Since the default bed friction implemented in SWAN is based on a sandy bottom, the above mentioned filter will effectively replace non-physical values of K_N, computed from a wide range of sediment size data. Sensitivity analysis was performed by applying $K_N = 250d_{50}$ for the first time period which led to less than 5% change in H_s at NDBC 42007 (The remaining stations show less H_s change). Note that SWAN also uses $f_w = 0.3$ for values of $\frac{a_b}{K_N}$ smaller than 1.57 instead of the value from Equation 4.4 (Jonsson, 1980).

For this study, the sediment grain size distribution data for the Gulf of Mexico were collected from the usSEABED database. The data on mean grain size distribution were scarce for the southern half of the Gulf of Mexico. Therefore, the average value of roughness height for the region north of 24° latitude was calculated and applied for the entire domain south of 24° latitude. This approximation is assumed to have negligible effects on the overall outcome from this study, given the fact that, as will be discussed in later sections, the bed material affects the simulated wave height mainly in shallow water. Hence, the simulated wave parameters from shallow water south of 24° latitude are rarely included in this study to evaluate the performance of the model. More than 16000 data points, predominantly concentrated along the shallow US coastal water, are used for interpolation of d_{50}, ranging from very fine clay to coarse sand. However, most of the samples were within the range of very fine silt to medium sand.

4.3 Results and Discussion

The mean H_s was calculated during the last two weeks of March 2007 (referred to as the cold front period hereafter), using both JONSWAP and Madsen et. al (1988) formulae, to

determine the effect of the friction formula on bulk wave parameters. The maximum H_s computed using either of two methods were approximately 3 m and the average H_s of hourly outputs over the entire Gulf of Mexico were approximately 1.2 m. The absolute value of the difference between hourly-averaged H_s over the entire Gulf of Mexico using two different formulations of bed friction is depicted in Figure 4.2. It shows that change in the average H_s can exceed 15% of the averaged wave height (shown in red) at isolated locations, viz., Golfo de Batabano, Cuba; Waccasassa Bay, Florida Gulf coast; and the south-central Louisiana coast. Although the bed friction effect is considered important for shallow water wave transformation, when $k_p h < \pi$ (Young and Gorman, 1995) in which k_p is the peak wave number, it is also important regarding the inter-relationship between the characteristics of bed materials and the water depth. This approach implicitly includes hydrodynamic conditions because it depends on the simulated wave fields during the study period. However, it is more convenient to present it by the influence of water depth in which one should also expect the complex interaction of waves with bed sediment characteristics. Comparing 15 m isobaths with contours of 5% and 10% change in the mean H_s, shows that the region of significant change in mean H_s is mainly shallower than 15 m. However, along the Waccasassa Bay, west of Florida, the 5% change extends to the 20 m isobath.

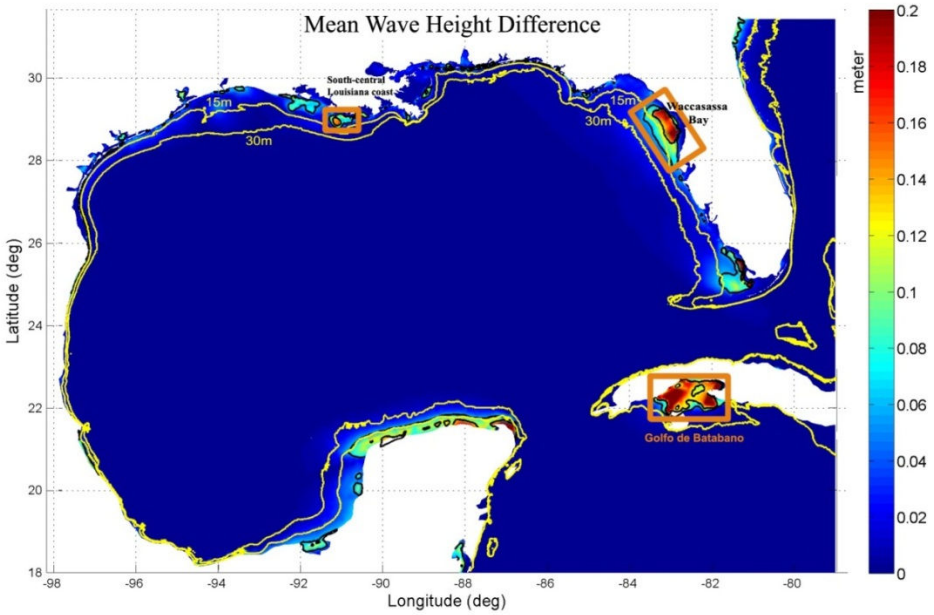

Figure 4.2: Change in hourly-averaged significant wave height over the entire Gulf of Mexico for cold front period. Black lines show contours of 5% and 10% change in significant wave height, and yellow contours represent the 15 m and 30 m isobaths. The boxes show the locations where significant changes in simulated mean significant wave height were computed.

In order to have a better understanding of the importance of bottom friction formulation in wave models, the H_s distribution was simulated when Hurricane Dennis moved across the Gulf of Mexico. Figure 4.3A presents the wave height distribution at 0000 UTC on 10 July 2005, when Hurricane Dennis was located off the south west coast of Florida (see Figure 4.1 for the hurricane trajectory).

The difference between computed wave height using JONSWAP and Madsen's bed friction formulations is provided in Figure 4.3B. It is evident that the JONSWAP formulation generally results in higher wave height than the Madsen formulation. Moreover, the difference between two formulations is spatially extensive and the wave height difference of 1.5 m is observed near the Waccasassa Bay, west Florida. Panel (C) shows that the relative change in wave height can exceed 25% along the coasts, in water depths less than 30 m. During extreme weather events, such as Hurricane Dennis, the relative difference of 40% can be found in water depths shallower than 15 m. Note that 15 hours later, when Hurricane Dennis moved closer to the Florida Panhandle, the difference between both formulations remained substantial.

Although *in situ* wave data were not available along the Florida Gulf coast during Hurricane Dennis, directional wave data from CSI06, off the south-central Louisiana coast, were analyzed (see Figure 4.3F) for this duration. The data from CSI06 were further used to evaluate the performance of bed formulations and the results are presented in Figure 4.4. The stations of WAVCIS were equipped with both ADCP and Paro-scientific® pressure sensors and the good agreement between two datasets guarantees the accuracy and reliability of *in situ* observations from this program.

Note that both formulations resulted in the same values for H_s during fair weather condition at this station. However, as H_s increased and wave interaction with the bottom increased, the difference between simulated H_s using the two methods increased. After a few hours, the H_s decreased; hence the effect of bed friction on wave propagation decreases considerably, and the two simulated H_s became similar again. Based on the research presented here, the bed friction formulation of Madsen et al (1988), was in better agreement with *in situ* observations secured during this storm event than that of the JONSWAP formulation. It was also important to note that use of the Madsen model for bed friction in the simulation took an additional 4% of computational time when compared to the JONSWAP formulation.

4.4 Conclusions of Chapter 4

The third generation wave model SWAN was implemented on an unstructured mesh grid to simulate wave fields generated from cold fronts and during the approaching phase of Hurricane Dennis. Measured bulk wave parameters from deep water NDBC buoys and shallow water WAVCIS stations were used to evaluate the performance of the wave models. The model was used to study the effect of bed friction formulations and the advantage of using the bed sediment characteristics in wave height computations.

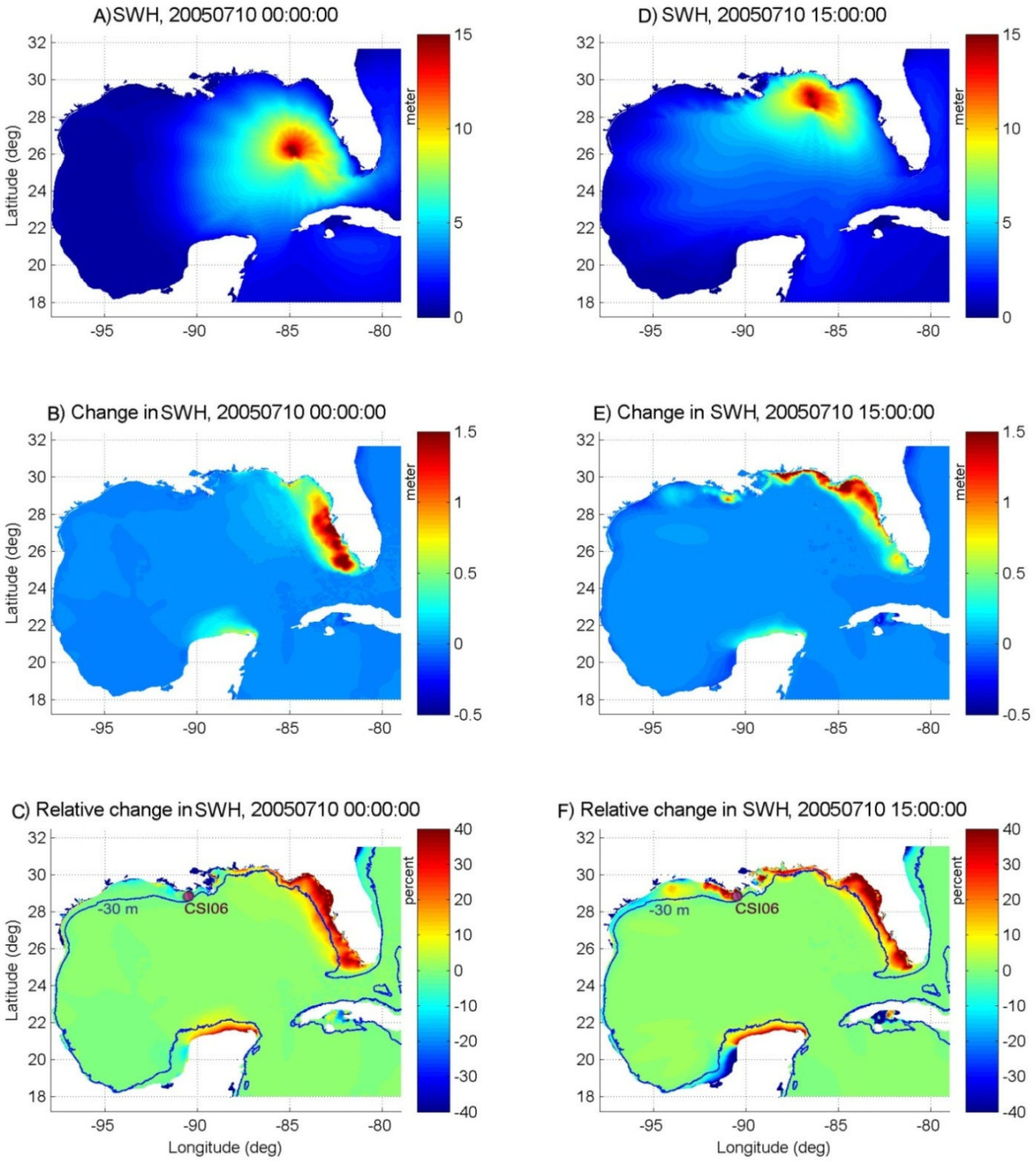

Figure 4.3: Wave height simulation results during Hurricane Dennis. Left panels: A) significant wave height using JONSWAP bed formulation, B) Difference in significant wave height using Madsen bed friction formulation instead of JONSWAP formulation, C) Relative wave height difference between two bed friction methods. Right panels are similar to left panels, except with results from 15 hours later. Blue lines in (C) and (F) are 30 m isobaths.

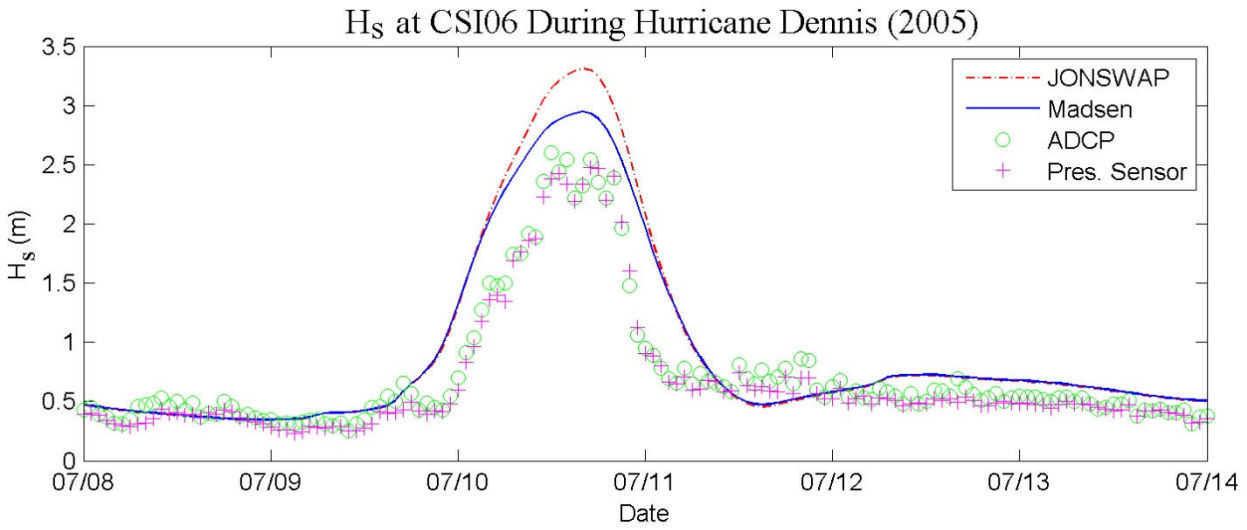

Figure 4.4: Comparison between hindcast H_s at WAVCIS station, CSI06, during Hurricane Dennis computed using JONSWAP and Madsen bed friction formulations in SWAN. Measured data from ADCP and pressure sensor at CSI06 are also provided.

The results showed that the JONSWAP bed friction model with default values generally underestimated the energy dissipation due to bed friction, which resulted in an overestimation of H_s in shallow water. During severe storms and hurricanes, such as Hurricane Dennis, the difference between JONSWAP and Madsen et al. (1988) formulations exceeded 1.5m or 40% of local wave height. The spatial extension of the difference between two formulations depended on the intensity of the wave field and this effect exceeded beyond (seaward) of the 30 m isobath. However, in terms of average wave height during fair-weather and storm conditions, the discrepancy between two formulations became largely confined to shallower water, i.e. landward of the 15m isobath. The study also showed that using the Madsen et al. (1988) formulation with usSEABED sediment data, resulted in a superior hindcast with negligible increase in computational time needed to perform the simulations.

CHAPTER 5: WAVE AND BOTTOM BOUNDARY LAYER DYNAMICS OVER THE SAND SHOALS OFF THE ATCHAFALAYA SHELF DURING COLD FRONTS

5.1 Introduction

This chapter describes the extended deployments during low and high discharge periods of the Atchafalaya River, and data analysis of meteorological, hydrodynamic and bottom boundary layer parameters from Tiger and Trinity Shoals. Part of these processes data is used in the next chapter to validate the wave model, SWAN.

The Atchafalaya-Vermilion Bay system is the largest estuary along the Louisiana coast, receiving between 15-30% of total flow of Mississippi River and nearly 40-50% of its sediment load through Atchafalaya River (Allison et al., 2000; Mossa and Roberts, 1990). Based on the river discharge data archived over the 1952-1989 period, at Simmesport station, LA (160 km north of Marsh Island), average sediment load of the Atchafalaya River is 84 million tons per year which includes 17% sand (Allison et al., 2000). The bay system is 2-3 m deep and predominantly blanketed by a thick layer of mud outside of the Wax Lake and Atchafalaya delta in Atchafalaya Bay. There are several scattered relict sand shoals on the low gradient shelf southwest of Atchafalaya Bay and south of Marsh Island (e.g. Tiger and Trinity Shoals shown in Figure 5.1). Away from sand shoals and oyster reefs on the inner shelf adjacent to Marsh Island, the mean particle diameter of bottom sediments is 2-7 μm, which is the same as suspended particle size from the lower Atchafalaya River (Sheremet et al., 2005; Wells and Kemp, 1981).

The tides are diurnal and the mean amplitude is less than 0.5 m, producing tidal currents with average speed of nearly 0.1 m/s, landward of 10 m isobaths (Walker and Hammack, 2000; Wells and Roberts, 1980), and waves are the dominant force for local resuspension of sediments (Jaramillo et al., 2009). Simultaneous measurement of waves and suspended sediment concentration (SSC) from an offshore station on Atchafalaya shelf (CSI 03 in Figure 5.1) showed that SSC could reach 0.5 g/liter, throughout the water column, during the passage of Hurricane Claudette. By the beginning of the waning phase of the storm, sediments accumulated at bottom layers of the water column and a persistent high SSC remained at 1 m above bottom (mab) (Sheremet et al., 2005).

High concentrations of mud close to the bottom were also reported during the passages of winter storms, from a station along the seaward margin of the Atchafalaya subaqueous delta (approximately 60 km to the east of station TT2 in Figure 5.1) and further westward of the delta front (approximately 20 km to the east of station TT1 in Figure 5.1) by Jaramillo et al. (2009). Based on measured data from the same location off the Atchafalaya Bay, as discussed in Jaramillo et al. (2009), Safak et al. (2010) demonstrate nearly monotonic relation between Reynolds stress and sediment concentration; and concluded that suspended sediments near the bed are locally entrained into water column by surface wave influence.

The turbid plume exiting the Atchafalaya bay system, that is advected to the west along the Louisiana coast, is referred to as mud stream (Wells and Kemp, 1981). The mud stream is confined to water depth less than 10 m (Kineke et al., 2006), moving westward due to a sustained westerly low frequency circulation of Texas-Louisiana shelf during non-summer months (Cochrane and Kelly, 1986). The presence of the mud stream significantly influences the wave characteristics of western Louisiana coast. Deploying an array of wave sensors approximately 40 km west of Marsh Island, Elgar and Raubenheimer (2008) demonstrated the rapid dissipation of wave energy when it propagates across the Atchafalaya mud stream. Sheremet and Stone, (2003) compared the time series of wave height and period measured at CSI03 (see Figure 5.1) with another station located 150 km east of the Bay in a sandy environment, having the same depth. They found that mud-induced dissipation affects not only the long period waves but also the high frequency waves, which in turn interact scantly with the sea bottom.

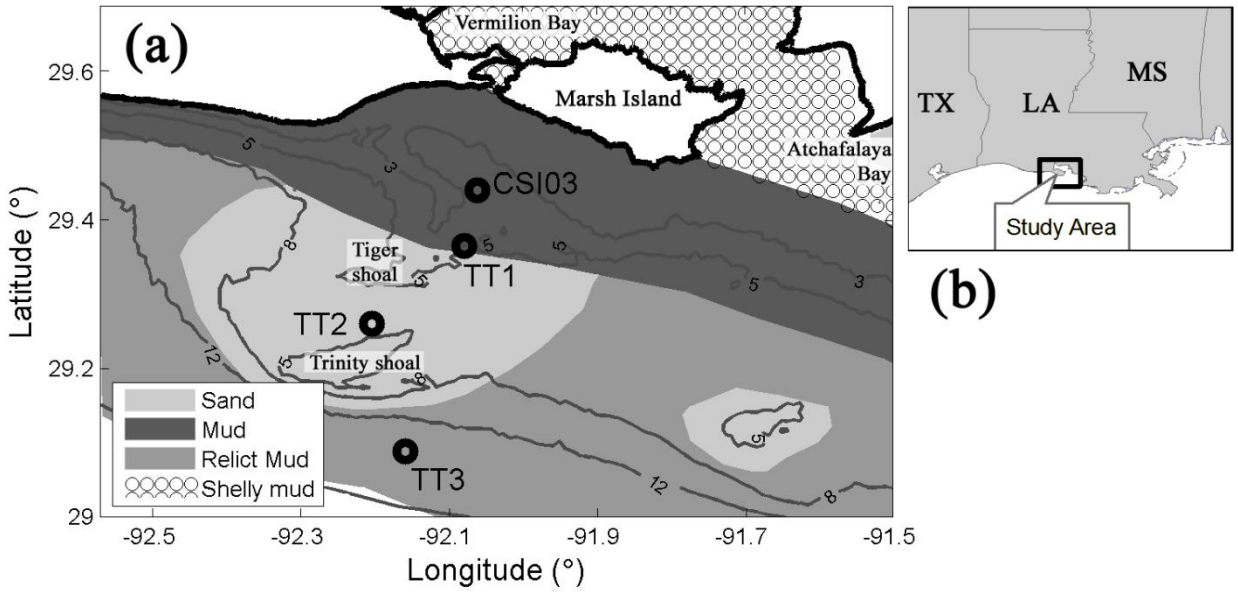

Figure 5.1: a) The study area, Atchafalaya Bay and the surrounding shelf. The location of three deployment sites at the Tiger and Trinity Shoal Complex are also shown. CSI03 station, part of WAVCIS network, also is included. The shadings represent a qualitative map of sediment type in the Atchafalaya shelf (modified from Jaramillo et al., (2009)); b) the location of study area with respect to the northern Gulf of Mexico.

During the passage of a cold front over the inner shelf opposite Atchafalaya Bay, which occurs every 4-7 days in winter/spring seasons, the wind direction changes clock-wise from pre-frontal southeast direction to south, west, and eventually to north. West winds disrupt the westward movement of mud stream and Ekman transport contributes in extending the sediment plume farther to the south. The prefrontal water level set-up along the Atchafalaya Bay would

also be released once the front passed through the region (Feng and Li, 2010). North wind during the cold fronts also results in rapid seaward flushing of sediment-laden river plume (Walker and Hammack, 2000) and the low salinity area can extent up to 50 km offshore (Allison et al., 2000). Based on the data from a transect south of Marsh Island (see Figure 5.1), Allison et al., (2000) showed that during early stages of a frontal passage, the SSC in entire water column can exceed 1 g/l in water depth shallower than 5 m. After a few hours of wind speed weakening, accumulation of sediments close to bed can form a fluid mud with concentration more than 25 g/l.

Most of the previous research on bottom boundary layer and wave-mud interaction from the Atchafalaya shelf were based on data measured from mud dominated environments. For this study, we have focused on the influence of cold fronts on wave transformation and sediment resuspension and transport over transgressive sand shoals on the inner shelf off the central Louisiana coast, eg. Tiger and Trinity Shoals. Although the Tiger and Trinity Shoals are physically away from the river mouth, Atchafalaya River discharge and sediment load may interact with the hydrodynamics of the shoal environment. Therefore, extra-tropical winter storm-induced hydrodynamics, bottom boundary layer parameters, and sediment resuspension at Tiger and Trinity Shoal Complex were investigated during low and high discharge from the Atchafalaya River. The interaction of high frequency waves generated by frontal passages and offshore swells waves with resuspended fine sediments were also discussed in more detail. Finally, the opportunity to employ diverse range of acoustic and optical instruments to simultaneously measure waves and SSC from the shoal complex helped us to compare their performance in a mud dominated coastal environment.

5.2 Experimental Setting

A transect across the Tiger and Trinity Shoal complex was identified based on the bathymetry and general orientation of the shoal complex. Three locations were selected for seasonal deployment of instrument tripods, which included acoustic and optical instruments for recording waves, sediment concentration, and current profiles. The stations were designated as TT1, TT2 and TT3 in Figure 5.1. The tripod location at TT2 was located on the northern flank of the Trinity Shoal because no offshore oil platforms, or any other sturdy structures were identified on the shoal crest for safely tethering the tripod. Inshore of station TT1, a permanent observation station, noted as CSI03 in Figure 5.1, provided the meteorological as well as hydrodynamic conditions close to the shore. This station is part of the Wave, Current and Surge Information System (WAVCIS), designed to provide continuous observation of met-ocean conditions from the northern Gulf of Mexico (Stone et al., 2001). A qualitative map of bed sediment type from the Atchafalaya shelf is also provided in Figure 5.1.

Since the discharge of fresh water and sediments from the Atchafalaya River may affect the bottom boundary layer characteristics of the shoal complex, two time periods were selected for deployments. According to the recorded mean flow at Simmesport station, close to the

diversion point in the upper Atchafalaya basin, the river discharge is approximately 5000 m^3/s with the maximum discharge occurring between January and June (Kineke et al., 2006). In the first deployment, hereafter referred to as experiment A, a Pulse Coherent Acoustic Doppler Profiler (PCADP) and an Acoustic Doppler Current Profiler (ADCP) were deployed at TT1, during Dec 3, 2008 to Dec 18, 2008.

Comparison between the performance of these two acoustic devices in measuring wave characteristics, and monitoring the flow energetics and sediment dynamics over Tiger Shoal, before the start of high discharge season, were the main objectives of this deployment. Quantification of the wave attenuation over the muddy environment between TT1 and CSI03 was another goal for this test deployment.

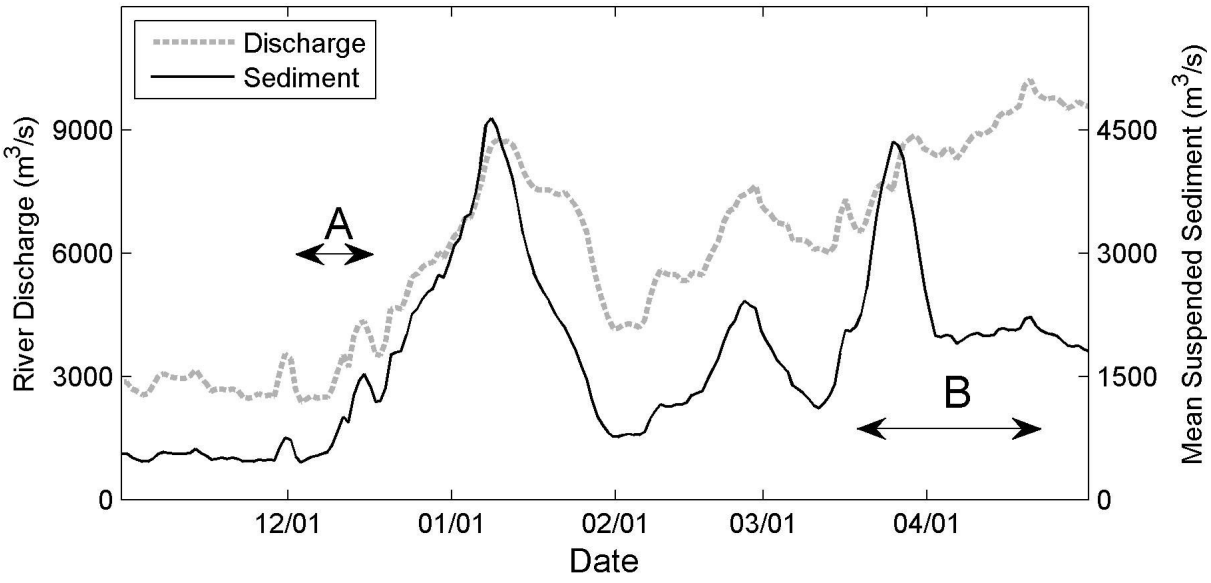

Figure 5.2: Daily mean discharge of Atchafalaya River and its mean suspended sediment load, measured at Simmesport station, LA (Data courtesy USGS). The time period of experiments A and B are shown by double arrows.

In the second deployment, hereafter called experiment B, three tripods were deployed at TT 1-3, to measure the wave and current parameters and sediment concentration close to the bottom, over both Tiger and Trinity Shoals, from March 19 2009 to April 23 2009. However, due to malfunction of wave sensor deployed at TT3, the wave transformation could not be studied over Trinity Shoal.

The daily mean discharge and sediment load from the Atchafalaya River are depicted in Figure 5.2. As expected, the discharge was less than its mean value during experiment A, and

both river discharge and suspended sediment load increased uniformly during the December deployment. This low discharge and sediment load during experiment A was in contrast with the discharge scenario from experiment B, in which a higher than mean value for water discharge was observed for the entire deployment duration. A single peak in sediment load was also recorded.

In experiment A, the upper water column was monitored using an upward looking 1200 kHz RDI workhorse ADCP, which was fixed on the instrument tripod with sensor head at 75 cm above the bottom (cmab), and having 25 cm bin size and blanking distance of 62 cm above the transducer head. The ADCP recorded 2048 velocity and surface track data points for each hour, with sampling frequency of 2 Hz. Moreover, it had an inbuilt pressure sensor, with the same sampling frequency. A downward looking SonTek 1.5 MHz PCADP was also deployed to record high resolution velocity profiles close to the bottom. The transducer head was approximately 110 cmab, and 37 bins of 3.3 cm wide starting from 15 cm below the sensor. The sampling frequency of hourly records measured by PCADP (burst mode) and its built-in pressure sensor was 2 Hz. Two OBSs (Campbell Scientific and D & A model 3+ Optical Backscatterance Sensors) sampled at 2 Hz providing 2048 data points for each hour at 25 and 60 cmab.

Wave data were also measured at CSI03, from hourly 17 min records of pressure fluctuations; sampled at 2 Hz. At all WAVCIS stations, highly sensitive Paro-scientific® pressure sensors, used for measuring waves, were deployed at 1.5 m below water surface, to be able to resolve high frequency waves. Meteorological parameters were also sampled at 1 Hz for a 10 min period and the average values were recorded. Wind speed and direction were measured approximately 24 m above water surface; Because measurements of air and water temperature, humidity and barometric pressure were also available from CSI03 during both experiments, it was possible to convert the wind velocity to equivalent neutral wind, following the method of Liu and Tang (1996).

During experiment B, TT1 and TT2 had an identical PCADP and OBS sensor configuration, as in experiment A. However, the ADCP's were configured to record 10 minute-averaged current data for every 20 minutes. In addition, both tripods also housed two Seabird Microcats, which measured temperature, salinity and depth, at 50 and 100 cmab. Moreover, 6 m away from the main tripod at TT2, an additional SonTek downward looking 5 MHz Acoustic Doppler Velocimeter (ADV) was deployed at 50 cmab with sampling volume at 18 cm below the sensor head. The pressure data were also recorded using an external Druck pressure sensor at 70 cmab. The 2048 records were acquired at 4 Hz sampling frequency for every 30 minutes.

The tripod at TT3 (offshore station) included one downward looking ADV at 50 cmab with an internal pressure sensor. However, the data from this ADV were discarded after noticing several long gaps in most of the burst records. There were also 2 OBS sensors on this tripod, deployed at 25 and 50 cmab, which worked fine. The ADCP at CSI03 was also maintained before experiment B, which was an upward looking instrument having 0.5 m bin size and the

sensor head was located 50 cmab. Unfortunately the Paro-scientific® pressure sensor at CSI03 stopped working on March 24 2009, and the anemometer failed on April 1 2009.

5.3 Methods

The preprocessing of PCADP and ADV data were performed using the Hydratools toolbox (Martini et al., 2005), a MATLAB toolbox developed by U.S. Geological Survey consisting of several filtering and visual tools to detect and fix outliers in the dataset. The pulse-coherent technique used in PCADP determines the along-beam velocity based on the phase shift between two consecutive reflected signals. However, the phase shift is limited to $-\pi$ to π, resulting unambiguous velocity in the range of $-0.5V_a$ to $+0.5V_a$, and the velocities outside this range would fold into this range. The so called resolution velocity, V_a, depends on sound velocity, instrument frequency, resolution cell distance (0.6 m in both PCADPs) and time between consecutive emitted signals. Lacy and Sherwood (2004) modified the SonTek procedure to resolve velocity ambiguity by low-pass filtering of resolution velocities, and use of the time series to identify ambiguity errors, and reported superior performance of their algorithm than the original SonTek algorithm. Therefore, the algorithm of Lacy and Sherwood (2004) was used in this study.

Wave spectrum was determined from pressure data and two components of horizontal velocity using DIrectional WAve SPectra (DIWASP) Toolbox (Johnson, 2008). Hashimoto (1997) showed the superior performance of Extended Maximum Entropy Method for estimating the directional wave spectrum when three quantity measurements were taken at the same location. Therefore, EMEP was used for processing all directional wave spectra for ADV and PCADP data. However, the preliminary evaluation of the performance of EMEP implemented in Teledyne RDI software package, WavesMon, for processing ADCP data, showed that during low energy conditions, EMEP failed to converge; most likely due to low signal-to-noise ratio. Therefore the Iterative Maximum Likelihood Method (Pawka, 1983) was employed for three top layers of velocities measured by ADCP to determine the directional wave spectrum. Note that wave analysis was done for PCADP data using the central cell to avoid negative and positive bias due to near sensor effects and interference of the reflection from bottom (Lacy and Sherwood, 2004).

The 2048 burst pressure sensor records were demeaned and then partitioned into 15 subsets with 50% overlap. Each sequence was filtered using a Hanning window, and the spectrum having about 22 degrees of freedom and frequency resolution of 0.0078 Hz was calculated. The depth correction was also applied. Note that the same frequency resolution was used for final spectra from all wave sensors, and the directional resolution of 4 degree was employed for directional spectra of ADCPs, ADV and PCADPs.

Due to shallow sensor depth, linear water theory predicts that horizontal wave velocity and pressure fluctuations are less than 2% of their surface values for a wave component with frequency f_r, which is beyond 0.47 Hz and 0.4 Hz in Tiger and Trinity data respectively.

Therefore a cutoff frequency of 0.4 Hz is used for all wave spectra computations and a power tail of f_r^{-5} is assumed beyond cutoff frequency, in accordance with the theory of Phillips (1958).

It is worthwhile to distinguish between components of waves which are locally driven by wind (wind sea) and the components which have been generated far offshore (swells). In order to separate different wave components, the wave partitioning procedure of Hanson et al. (2009) was employed. In order to separate wind sea and swells, the following wave age criteria was used, based on Hanson and Phillips (2001):

$$c_p \le (1.5) U_{10} \cos\delta, \qquad 0 \le \delta \le \frac{\pi}{2} \tag{5.1}$$

In which c_p denotes wave phase speed, U_{10} is wind speed at 10 m above mean sea level, and δ is the angle between wind and wave components.

During the passage of cold fronts, the wind veers rapidly and another criterion is needed to distinguish between wind sea and young swells, which are recently released from the influence of wind forcing. Following Hanson and Phillips (1999), the wind sea component should maintain energy above a threshold level estimated by the equilibrium range theory of Phillips (1985). In low energy conditions, there may not be any peak in the wind sea section of the spectrum. Therefore the wind sea part was assumed to be the same as the entire parabolic region of the spectrum separated by Equation 5.1.

The turbidity of water was measured using OBS sensors at 25 and 60 cmab, at TT1, TT2 and TT3. The OBS sensor is highly sensitive to suspended particle characteristics (Baker and Lavelle, 1984). The readings of OBS sensors were correlated to true corresponding SSC, using sediment samples collected from their respective deployment sites; as suggested by previous studies (Downing and Beach, 1989; Kineke and Sternberg, 1992).

In order to do the sensor calibration at the Lab following routine was adopted: OBS sensor was immersed in a black bucket, half filled with distilled water, and having a stirrer. The leading cable was connected to a data logger with the same setup configuration as it was in the field deployment. Sediment collected from the deployment site was added to the bucket incrementally and stirred gently. For each step, 100 readings (in counts) were recorded, until the mixture reached a uniform condition and the average count would represent the water turbidity. Moreover, samples were taken from the sediment-water mixture, each time following the OBS data recording. The collected samples were filtered, dried in an oven at 35^{o} C, weighed which represented SSC in mg/l. The maximum measured SSC during the experiment was 6 g/l and a linear regression curve was generated by plotting OBS readings against their corresponding measured SSC; following Kineke and Sternberg (1992). The linear behavior of the curve was confirmed by a correlation coefficient ranging from 0.94-0.99, from different deployment sites across the shoal complex, and all data points were within two standard deviations from the regression curve (Kineke and Sternberg, 1992).

The backscatter signal strength of an acoustic instrument also could be potentially used for estimating the SSC. The theories for estimation of SSC using acoustic devices were mainly developed for ADCP deployments and used successfully in different coastal environments (Defendi et al., 2010; Gartner, 2004; Hoitink and Hoekstra, 2005; Thorne et al., 1999). Fugate and Friedrichs (2002) used ADV, OBS and LISST to determine concentration of cohesive sediments in Chesapeake Bay, USA; and found that ADV was the best estimator for SSC in that environment. A detailed evaluation of performance of ADV in estimation of SSC is recently presented in Ha et al. (2009) which showed that the estimates of ADV was noisier than that from OBS, due to smaller sampling volume. More recently, Ha et al. (2011) also adopted the acoustic methods of SSC-estimation for PCADP, and showed their success in the estimation of SSC in both the lab and field environment.

For ADV, the sampling volume is few centimeter away from the transducer head (18 cm for 5 MHz ADVOcean used in this study). Therefore, the effect of absorption of signal by sediment or water was negligible and a linear regression curve was assumed between the logarithm of backscatter signal strength (measured in count=0.43 dB (SonTek, 2001)) and logarithm of SSC (Ha et al., 2009). However, for the case of PCADP, profiling range was much more extended and the acoustic inversion algorithm was more complex. Following Ha et al. (2011), the simplified sonar equation proposed by Deines (1999) with inclusion of sediment effects on the backscattering was employed in this study; which assumed the following relation in profiling range of PCADP:

$$10\log(SSC) - 2(\alpha_s + \alpha_w)R - 20\log(\psi R) = K_c E + C \tag{5.2}$$

where E is echo level (in counts), R is the distance between the transducer and measurement volume, α_w and α_s are attenuation due to water and the sediment concentration, and K_c and C are signal calibration coefficients. Close to the transducer, the assumption of spherical spreading is no longer valid, therefore the coefficient ψ is also used in Equation 5.2 to distinguish between near and far transducer fields, according to the equation proposed by Downing et al. (1995). The attenuation by water column is composed of pure water absorption and ionic relaxation processes of boric acid and magnesium sulphate. Francois and Garrison (1982) suggested a set of equations to calculate these components of α_w as a function of salinity, temperature, water depth, pH and frequency of the transducer (f). The attenuation of signal due to sediment, α_s, is itself the sum of two components: scattering loss (ξ_s) which is important for larger particles (>50 μm for f =1.5MH), and viscous absorption (ξ_v) which is dominant for fine-grain sediment. Finally α_s can be determined from the following equation (Ha et al., 2011):

$$\alpha_s = \frac{1}{R}\int_0^R (\xi_s + \xi_v)\, SSC(r)\, dr \tag{5.3}$$

In which r is the sub-distance from the emitter. A detailed parameterization of ξ_v and ξ_s can be found elsewhere (Richards et al., 1996; Thorne and Hanes, 2002; Thorne et al., 1991). Note that α_s depends on SSC, and therefore the Equations 5.2 and 5.3 need to be solved iteratively. Because the iterative feedback between SSC and α_s was positive, the under-relaxation of the solutions in each step was performed to avoid diverging to infinity (Hageman and Young, 2004; Thorne and Hanes, 2002).

5.4 Observations

The wind speed and direction at CSI03 during the experiment A is presented in Figure 5.3a. During this two week deployment, a strong cold front crossed the study area on Dec 10 and its effect, in terms of elevated wind, waves and currents lasted for 3 days. Another weak storm event also occurred during Dec 4-7. The time series of significant wave height measured by PCADP and ADCP and the sea and swell components of wave height are shown in Figure 5.3b-d. The time intervals in which the difference between PCADP- and ADCP-measured wave heights were more than 20 cm, or if a variation of 10 cm would happen at least twice in a 12 hour duration, they are labeled in Figure 5.3b. Note that label (I) represents neither of the aforementioned conditions, but labeled as a representative of the conditions in which sea and swell components were different but the total wave heights were in good agreement. Such differences happened mainly due to the fact that two different methods were used to estimate directional distribution of energy from ADCP and PCADP measurements. Therefore, the spectral domain corresponding to sea and swell components were also different. The good agreements of sea and swell peak period and direction shown in Figure 5.3k-n confirm this explanation. The significant variation between wave heights is demonstrated by label (V) in Figure 5.3b. The velocity data recorded by PCADP during this time period, as well as for the durations corresponding to labels (IV), (VI) and (VII), contain several spikes which have been introduced most likely by ambiguity resolution algorithm, as described in section 5.3. To quantify this error, any spike in u and v velocity which exceeded both previous and next recorded velocities by at least 30 cm/s and at least one standard deviation, was flagged as an erroneous jump. The Figure 5.3e demonstrates the maximum number of erroneous jumps in U and V velocities coincident with labels (IV), (V), (VI) and (VII) in Figure 5.3b.

The discrepancies in wave heights labeled as (III) and (VIII) can be explained in terms of non-uniform velocity profiles of currents in water column. The recorded current speed profiles are shown in Figure 5.3f-g for ADCP and PCADP respectively, and the corresponding current direction profiles are shown in Figure 5.3h-i. Note that the colors are selected according to the convention of "coming from" for the currents, to be consistent with conventional wind and wave directions as shown in panels (a), (m) and (n). In general, current direction during cold front passages was uniform throughout the water column and mainly controlled by the prevailing wind direction. By default, the ADCP would use velocity from the top layers to estimate wave spectrum while PCADP would use the velocity from bottom layers.

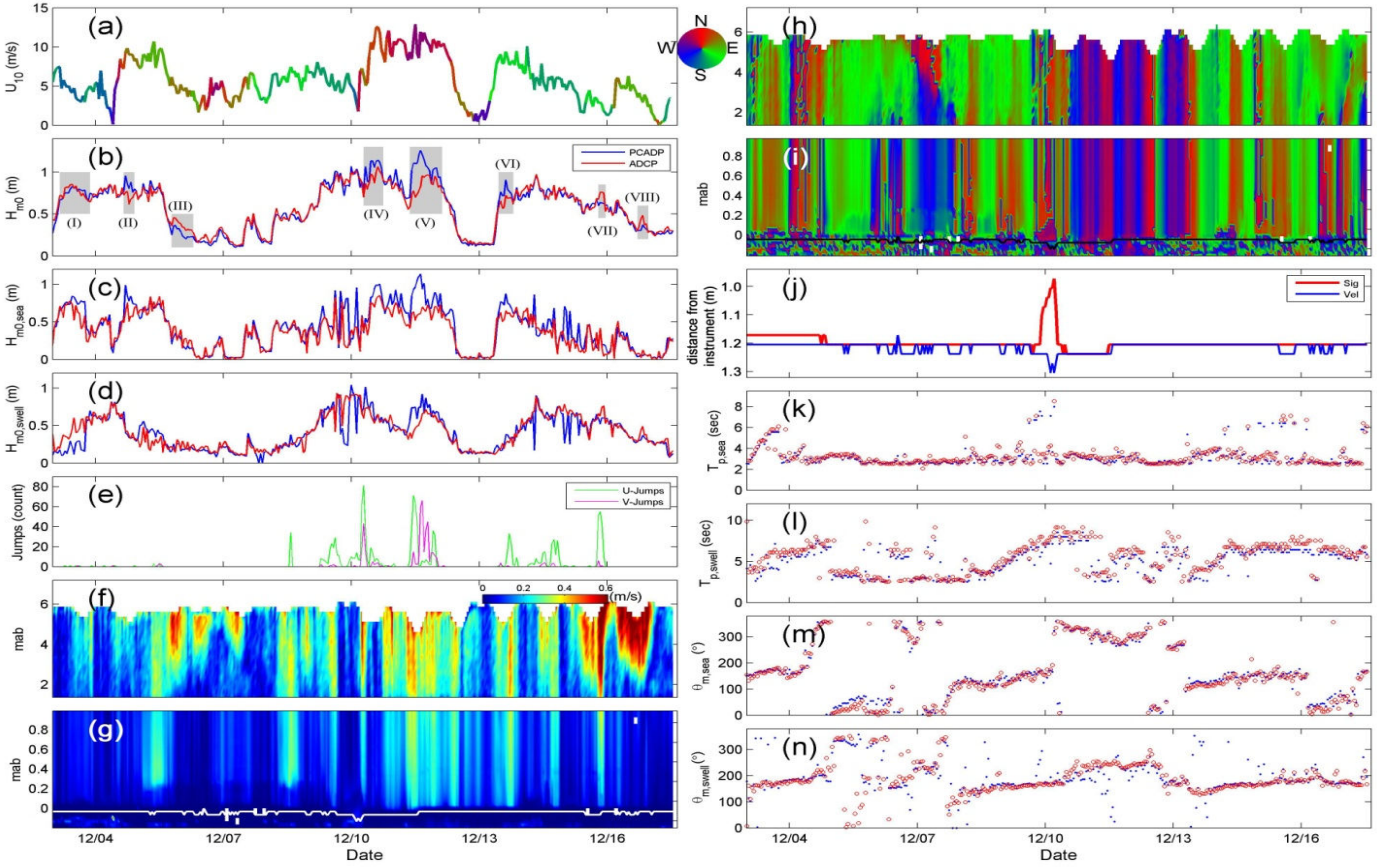

Figure 5.3: a) Time series of wind speed and direction measured at CSI03 during experiment A; b) Wave height measured by ADCP and PCADP. The shadow blocks and the labels represent the occasions when the instruments were not in good agreement; c-d) The sea and swell wave height; e) the number of suspicious jumps in measured velocity components by PCADP; f-g) horizontal current speed profile measured by ADCP and PCADP respectively; h-i) current direction (with "coming from" convention assumed); j) hydrodynamic bed (zero velocity) and the height of maximum reflectance measured by PCADP; (k-l) peak wave period of sea and swell component; (m-n) mean wave direction of sea and swell component. The black line in (i) and white line in (g) are hydrodynamic bed.

During events labeled by (III), the high frequency sea waves were coming from the northeast while the surface current was still from the southeast. The opposing direction of waves and surface currents resulted in higher wave height recorded by ADCP. During event (VIII) the same happened and the only difference was the fact that sea component was weak and the difference between the instruments came mainly from the swell estimation (see Figure 5.3c-d). Although the Doppler shifting effect has been implemented in WavesMon processing software, and resulted in better agreement of wave heights during time period (III) and (VIII), it also introduced discontinuities in the high frequency end of spectrum. Therefore the current-wave interaction was purposefully kept inactive for wave processing of ADCP records.

During the time period labeled as (II), the ADCP and PCADP pressure sensor were not in agreement. This time period coincided with the time in which the depth of maximum backscatter changed (see red curve in Figure 5.3j). Most likely at this time, the weak northerly currents, resulted from the cold front of Dec 4, resuspended the "fluffy mud" from the Tiger Shoal crest and the instruments were not stable enough to record reliable data. The level with maximum backscatter signal, referred to as LMBS hereafter (red line in Figure 5.3j) becomes one with the hydrodynamic bottom (position of zero velocity shown by blue line in Figure 5.3j) from this point onwards. Sediment samples collected from the site during the deployment survey revealed a thick mud layer over a stable substrate of shell and shell hash mixture. The samples collected two weeks later, during the retrieval survey, were predominantly shell and shell hash. The change in bottom fabric, from fluffy mud to shell and shell hash mixture, indicates significant resuspension and transport of bottom sediments during this two week winter deployment period. Figure 5.3j also shows a significant resuspension at early stages of the cold front on December 10.

As mentioned earlier, the ADCP is able to provide a frequency spectrum using three distinct methods; high frequency pressure sensor sampling, orbital velocity method and directly from surface tracking (RD Instruments, 2001). The average of wave frequency spectra, independently computed using the aforementioned three methods, are shown in Figure 5.4. The bimodal distribution of energy has a wind sea peak at about 0.31 Hz, and a swell peak at about 0.13 Hz. Note that the default method for wave calculation is based on orbital velocity, which has the advantage of being in good agreement with pressure sensor data in the lower frequency end of the spectrum; while the surface track method would perform poorly at this end of the spectrum. The orbital velocity method is also in good agreement with surface tracking method in higher end of spectrum when pressure signal at the ADCP head would be too noisy. Good agreement of these methods verifies the general performance of the ADCP in producing wave spectrum from a range of met-ocean conditions.

The time series distribution of barometric pressure, air temperature and sea surface temperature at CSI03 during experiment A are provided, along with wind vectors, in Figure 5.5a-c. Although water temperature gradually decreased during cold front passages, decrease of atmospheric pressure during prefrontal stage and drop in air temperature during the passage of

cold fronts, are always expected (Pepper and Stone, 2004). Change in wind direction is very dramatic during a cold front event and it changes from the prefrontal southeast direction to southwest, west, north and ultimately, with the passage of the front, return back to normal conditions. The 40-hour low pass filtered water depth was calculated at TT1 using data from pressure sensor of PCADP and atmospheric pressure at CSI03. As shown in Figure 5.5d, water level set-up was produced close to the coast by prefrontal southerly winds and released by northerly postfrontal winds. The difference of water level before and after frontal passage at Dec 10 exceeds 0.6 m.

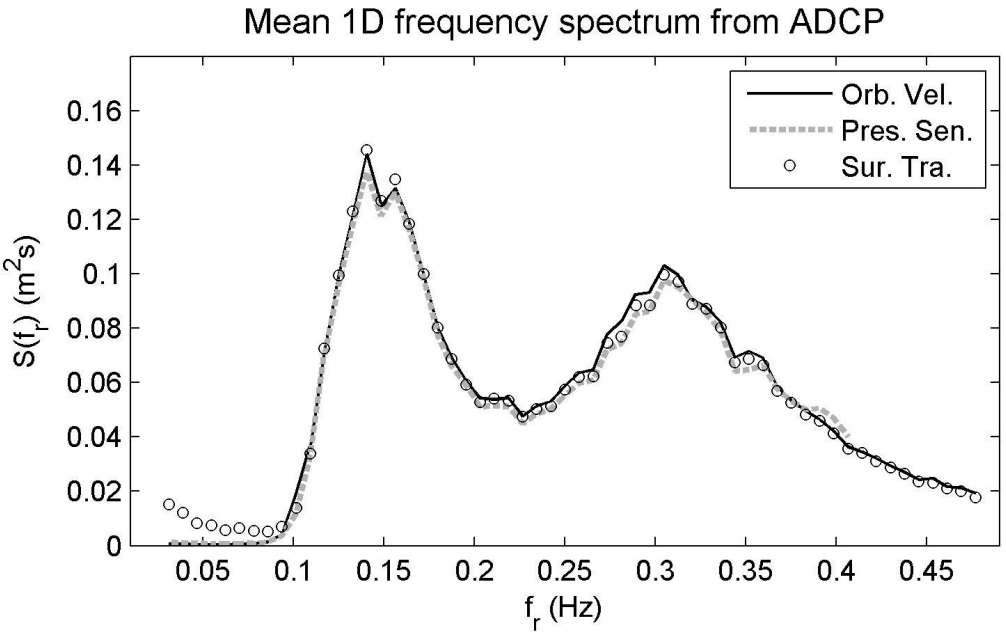

Figure 5.4: The average wave spectrum during experiment A (December 2008) at Tiger Shoal (TT1), measured by ADCP. Note the general agreement between the three discrete computational methods implemented for wave spectra.

Figure 5.5e shows the level of energy dissipation over a distance of approximately 9 km between Tiger station (TT1) and CSI03. Although the wave period did not show significant transformation (Figure 5.5f), the dissipation of wave height was highly noticeable and usually intensified during and after the passage of cold fronts. The SSC based on OBS and PCADP at 60 and 25 cmab are provided in Figure 5.5g-h. It is visually possible to evaluate the high correlation of wave energy dissipation, in terms of significant wave height (Figure 5.5e) and SSC (Figure 5.5g-h). During the cold front passage of Dec 10, the wave height measured at Tiger Shoal was almost 1 m for a few days following the frontal system passage, while the wave height recorded at CSI03 showed significant energy dissipation, after the SSC peak was recorded on December 10 at the offshore station.

The estimations of SSC based on PCADP backscatter intensity showed good agreement with both OBS sensors (see Figure 5.5g-h). The correlation coefficient was 0.79 for both OBS sensors, and the average SSC measured by OBS sensors at 60 and 25 cmab during the experiment A were 0.075 and 0.189 (g/lit) higher than the corresponding SSC estimated from PCADP data.

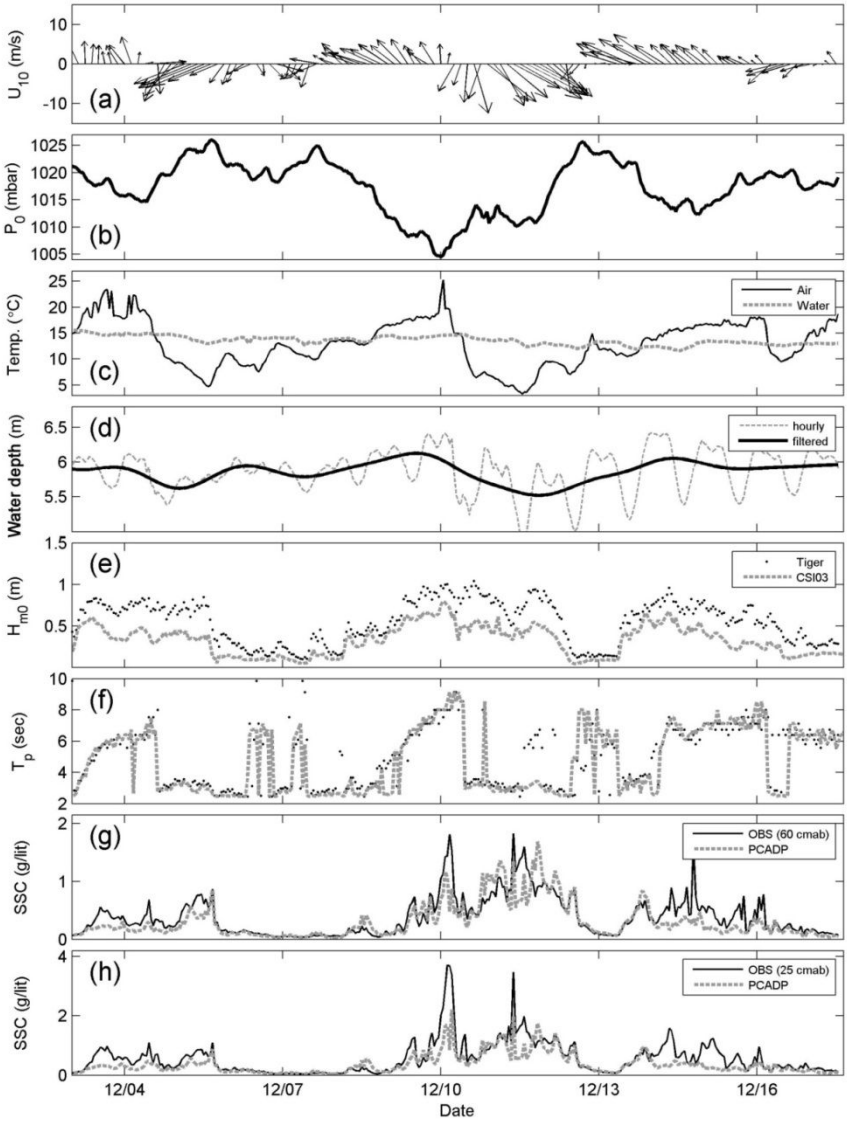

Figure 5.5: a) Wind speed and direction; b) barometric pressure; c) air and sea surface temperature measured at CSI03 station during experiment A (December 2008); d) Hourly water depth variation and its 40 hour butterworth low pass filter values at Tiger Shoal; e-f) wave height and peak wave period measured at Tiger Shoal and CSI03 station; g-h) suspended sediment concentration, estimated from OBS sensor and PCADP echo, at 60 and 25 cmab.

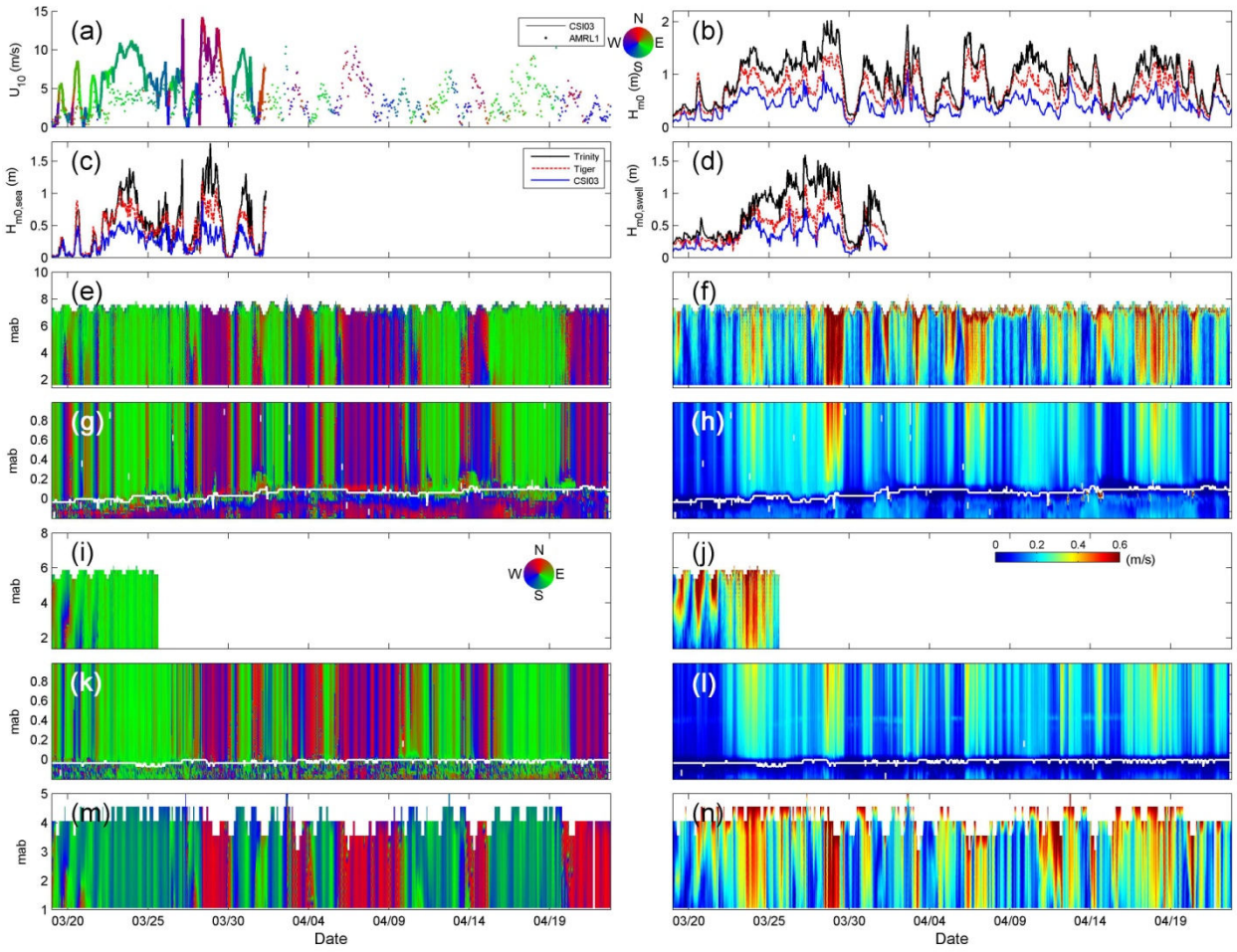

Figure 5.6: a) Wind speed and direction measured at CSI03 and NOAA AMRL1 (coastal station within Atchafalya Bay), during experiment B (March-April 2009); b) Significant wave height measured at CSI03, Tiger Shoal (TT1 in Figure 5.1) and Trinity Shoal (TT2 in Figure 5.1) ; c-d) The sea and swell wave height measured at the same three stations; e-f) Direction of horizontal velocity profile (upper water column) measured by ADCP at TT2; g-h) Corresponding horizontal velocity profile direction (for the bottom 1 m) measured by PCADP at TT2; i-l) repeating the e-h plots for TT1; m-n) repeating e-f plots for CSI03 station. The white curves in PCADP profiles show the hydrodynamic bottom.

The wind speed and direction measured at CSI03 during experiment B is shown in Figure 5.6a. The data from NOAA AMRL1 station are also shown in the same panel. This station is located approximately 40 km to the east of Marsh Island. Although the wind speed from AMRL1 station was lower than CSI03 due to coastal effects, the wind direction was in good agreement with CSI03 because the spatial scale of a cold front is of the order of 200-300 km. The time series distribution of significant wave heights at stations TT2, TT1, and CSI03 are shown in Figure 5.6b. Since the algorithm to separate wind sea and swell components requires

in situ wind speed and direction, these components could be calculated only when wind speed from CSI03 was available (see Figure 5.6c-d). It is evident that wind sea component closely followed the wind fluctuations for all stations. When wind speed was mild (< 5 m/s), all stations showed the same range in wind sea parameters. However, during more intense wind, the deeper stations had higher wind sea wave height. The swell component was lower for shallow waters, as expected, due to more dissipation from wave-bottom interaction as water depth would decrease. Energy of waves is proportional to the square of wave height; So, 10-70% of wave energy was estimated to dissipate between TT1 and TT2, and the wave energy decayed between TT1 and CSI03 by 30-90%. However, no significant trend was observed between the dissipation level of sea and swell wave components, Figure 5.6c-d.

The horizontal current direction and speed measured by ADCP for upper water column (Figure 5.6e-f) and PCADP for lower water column (Figure 5.6g-h), at TT2, show that wind was the main factor controlling the current field over Trinity Shoal during cold fronts. Similarly, current fields from the entire water column at TT1 and CSI03 locations, during the experiment B are provided in Figure 5.6i-l and Figure 5.6m-n respectively. Although generally decreased in deeper waters, the current speed exceeded 0.6 m/s at Trinity station (TT2), during frontal passages across the shoal complex.

The air pressure at CSI03 and wind vectors during experiment B are shown in Figure 5.7a-b which highlights the coincidence of air pressure drop and the corresponding change in wind vectors. As depicted in Figure 5.7c, the time series of surface water temperature at CSI03 and from 1 mab at TT1 and TT2 are aligned, and show slow response to cold front passages. However, air temperature dropped quickly once northerly cold air intruded from the continental USA into the Gulf of Mexico. Salinity variations measured 1 mab at TT1 and TT2 are demonstrated in Figure 5.7d. Low values of salinity at TT1 confirms the incursion of fresh water into the shoal complex, and, as expected, more dilution was noticed at TT1 than at TT2, given the proximity of the Tiger Shoal to the fresh water source from Atchafalaya River and also for its shallow bathymetry. The low pass filtered water depth variations at TT1 and TT2 during experiment B are provided in Figure 5.7e-f which show strong response of water level to wind direction. As expected, the wind-induced water level variation is more intense at TT1 because it is in a shallower water depth. It is important to note that beside wind stress, the change in atmospheric pressure and wave setup also contributes to water level variations (Li et al., 2011). The maximum water level variation during experiment B happened in the frontal passage on April 05 which exceeds 0.75 m and 0.55 m at TT1 and TT2 respectively.

The SSC estimates based on OBS readings and PCADP, at 25 and 60 cmab, at TT1 are shown in Figure 5.7gh. Unlike experiment A, there is low correlation between these two SSC estimates, especially after March 26 when high spring discharge from the River gradually began. Figure 5.7i provides similar pattern of SSC from station TT2. A high OBS reading is also found at TT3 (Figure 5.7j). The LMBS and zero velocity level from PCADP data were further analyzed to determine the shoal bottom, and the results are provided in Figure 5.7k-l for TT1 and

TT2 respectively. Unlike TT1 which had a stable bottom, TT2 experienced a series of resuspension events and a net sediment deposition after the passage of succeeding cold fronts. The deeper location of TT2, on the northern flank of Trinity Shoal, also might have contributed to this sediment accumulation with the passage of storms.

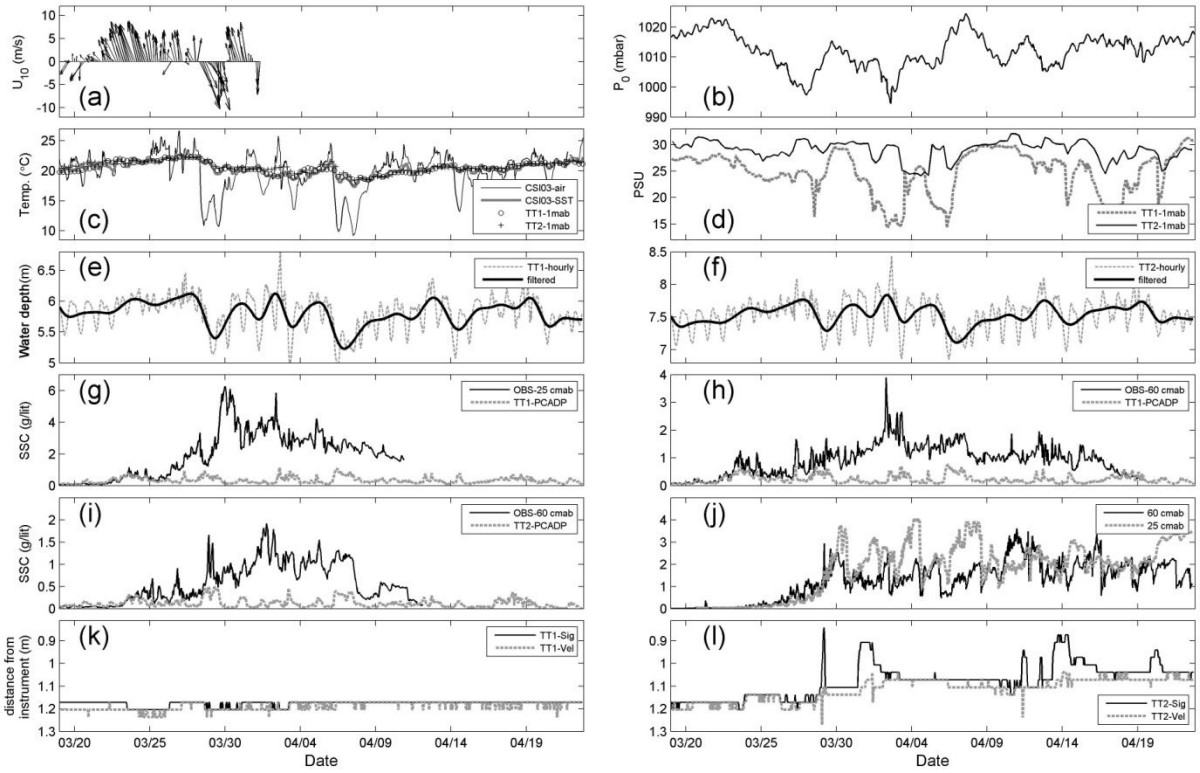

Figure 5.7: Time series of met-ocean data from the experiment B (March-April 2009): a) Wind vectors (incomplete due to instrument failure at CSI03); b) barometric pressure, c) air and sea surface temperature measured at CSI03 station as well as water temperature 1 mab at TT1 and TT2; d) Salinity distribution 1 mab at TT1 and TT2; e-f) Hourly water depth variation and its 40 hour butterworth low passes filter values at TT1 and TT2 respectively; g-h) suspended sediment concentration, estimated from OBS sensor and PCADP echo, at TT1, at 25 and 60 cmab respectively; i) Corresponding data as (h) from TT2 station; j) suspended sediment concentration, estimated from OBS sensor at TT3, at 60 and 25 cmab; k-l) hydrodynamic bed and the height of maximum reflectance measured by PCADP at TT1 and TT2.

The sediment samples from Tiger Shoal, before and after deployment in experiment B, were composed of 79-95% shell and shell hash. Unfortunately, no samples were taken farther north of TT1, on the Tiger Shoal, to determine the shoreward extension of shell materials.

However, the bed samples taken periodically from CSI03 during the last 10 years by WAVCIS field support group confirmed that the bottom material at CSI03 always consists of cohesive sediments, derived from the westward flowing Atchafalaya mud stream. Based on median grain size (D_{50}) of the non-shell fraction of the sediment samples at TT1, medium to fine sand forms the rest of the Tiger Shoal bed materials. The concentration of shell materials slightly decreased 1 km southwest of the TT1 to approximately 70%, and became less than 19% within 3 km southwest of TT1.

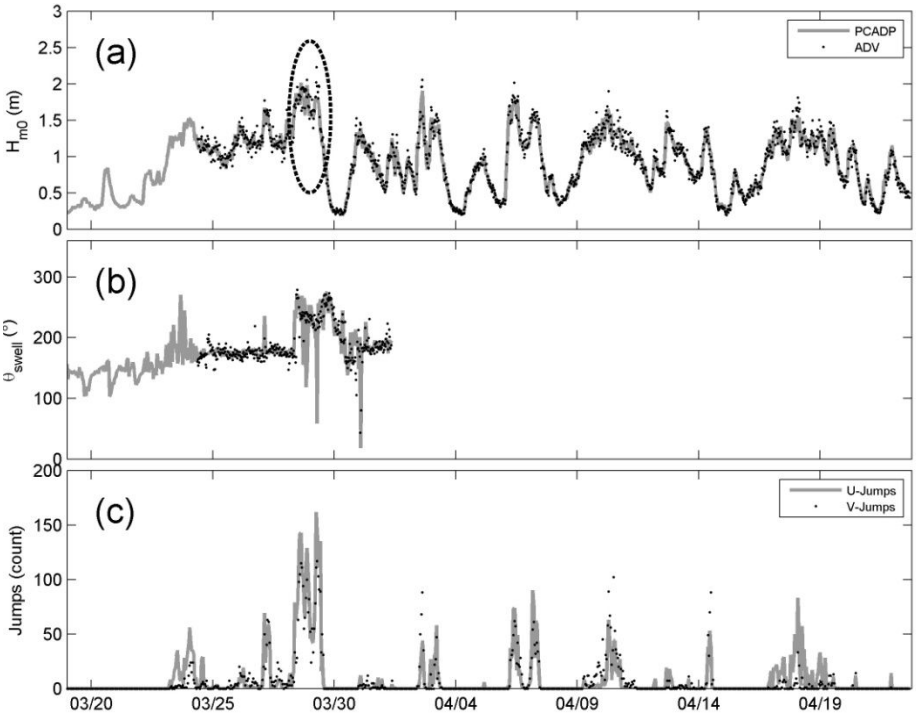

Figure 5.8: Comparison of PCADP and ADV in terms of a) significant wave height and b) swell wave direction; Panel (c) shows the number of suspicious jumps (u and v velocity components) in each burst for PCADP.

The sediment samples close to TT2 site had a dominant particle size of fine sand (D_{50}=0.125mm), before and after deployments. However, the samples collected from the shoal crest during the deployment survey contained more medium sand, while the samples taken during the retrieval survey had more fine sand, and in some samples, the secondary peak happened in the grain size curves close to D_{50}=0.088 mm. Over the Trinity Shoal, the grain size distribution showed more medium sand and less fine sands after the deployment. The change in grain size distribution was negligible in the samples taken 2 km south of Trinity Shoal before and after deployment.

The wave heights measured by PCADP and ADV at TT2 during experiment B are compared in Figure 5.8a. Considering the different sampling frequency of two instruments (4 Hz for ADV and 2 Hz for PCADP), there was a good agreement between the two measurements (R^2=0.99 and rms=0.07 m); however as identified in Figure 5.8a, there is a short interval in which the difference between the wave height recorded by two instruments exceeds 30 cm. The directions of swell component of the wave spectra from two instruments during that time period are also very different (see Figure 5.8b). The number of suspicious jumps in velocity is depicted in Figure 5.8c, which shows several significant maxima in the same time period. Therefore, beside the inherent difference in configuration of these instruments, the ambiguity resolution algorithm is also partially responsible for the difference between wave spectra recorded by ADV and PCADP.

5.5 Discussion

Because the Gulf of Mexico is a semi-enclosed basin, the waves recorded during both experiments from Tiger and Trinity Shoal complex should be composed of local wind sea waves, young swells recently released from wind force due to change in wind direction, and swell waves generated farther offshore in the Gulf of Mexico. In the range of 3-9 second waves, recorded in experiment A (see Figure 5.3k-l), the group velocity is smaller than wind speed, and therefore young swells cannot propagate in front of wind fronts. Linear wave dispersion relationship predicts linear decrease of peak wave period with time (Hanson and Phillips, 2001). However, an increase of peak period before cold front events of Dec 4 and Dec 10 (Figure 5.3l) showed that swell energy during these time periods originated from events that were not well represented as a persistent point source. Small variation of the mean swell direction during Dec 10-12 is in agreement with persistent 0.5-1 m swell waves (see Figure 5.3n); however slight increase in wave direction happened due to energy contribution from northerly young local swells generated by wind veering to the north .

The wave spectrum evolution, particularly during discrete events of cold front passages, can be used to analyze the wave energy dissipation in more detail. The change of frequency spectrum between TT1 and CSI03 during experiment A is demonstrated in Figure 5.9a. The dissipation of low frequency waves (swells), in the range of 0.1-0.2 Hz, is in accordance with long wave paradigm (e.g. Sheremet and Stone, (2003) and references therein). The complex transformation at the high frequency end of the wave spectra, particularly during the passage of cold fronts, is attributed to the interaction with southerly waves generated from fetch limited post-frontal northerly wind. Fetch is more limited for CSI03 than TT1 (approximately 13 km vs. 20 km for northerly wind) and therefore more energy is expected at TT1 during cold front passages. In other words, the modifications in high energy end of spectrum are at least partially due to local generation of waves and not directly from energy dissipation. However, there are several time periods in which there is significant energy difference in high frequency waves at TT1 and CSI03 while wind direction is persistently from the south; e.g. Dec 3-5, Dec8-9 or Dec

14-16. Note that during all of these time periods, the SSC close to bottom is relatively high (Figure 5.5g-h). Sheremet and Stone (2003) also report the dissipation of short waves at CSI03 and suggest that mud-wave interaction is responsible for dissipation of both high and low frequency waves. One mechanism for such energy dissipation in shallow water is the transfer of energy from energetic high frequency waves to low frequency (Infra-gravity) waves by nonlinear triad interaction. The interaction of Infra-gravity waves and bottom in shallow water can effectively dissipate the wave energy (Elgar and Raubenheimer, 2008; Kaihatu et al., 2007; Sheremet et al., 2011). Recently, based on a two layer wave-mud model and without inclusion of triad wave-wave interaction, Kranenburg et al. (2011) show that mud-wave interaction itself also can dissipate energy from either low or high frequency waves, depending on the viscosity and the height of fluid mud layer. This model is used in the next chapter to reproduce the wave spectrum during cold fronts.

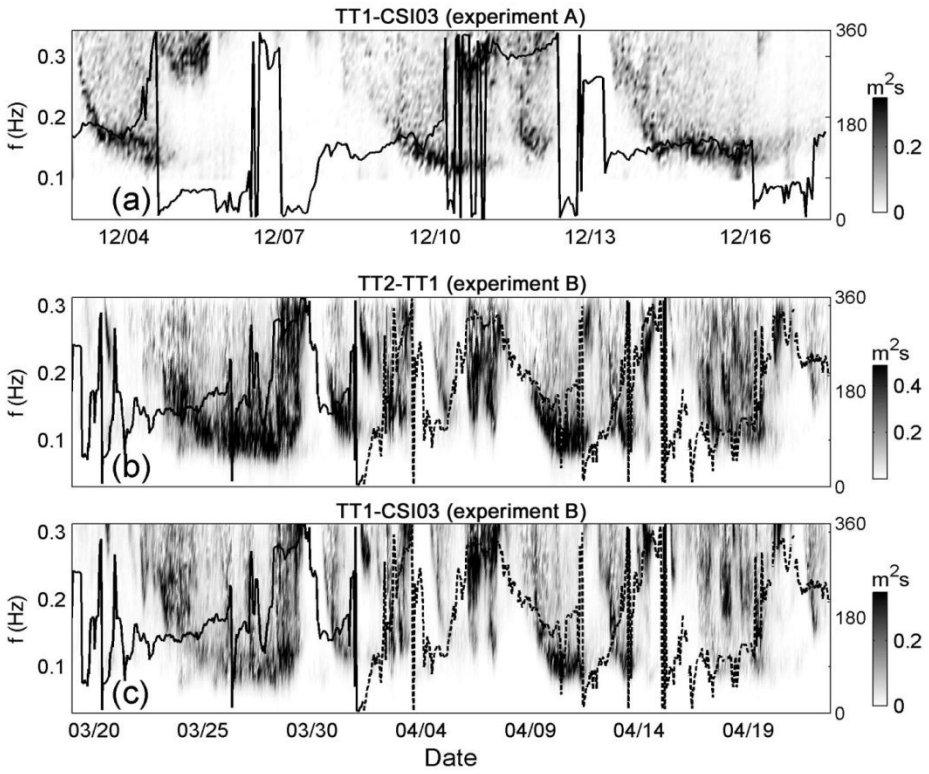

Figure 5.9: The contrast in energy level (as a function of time and frequency) measured a) by ADCP at TT1 and pressure sensor at CSI03, during experiment A; b) by PCADPs at TT1 and TT2 during experiment B; c) by PCADP at TT1 and ADCP at CSI03 during experiment B. The solid line is the time series of wind direction at CSI03. During experiment B, wind bird at CSI03 failed 10 days into the survey, thereafter wind direction from NOAA AMRL1 station, located approximately 40 km to the east of Marsh Island, is included in the plots, (see the dash lines).

Figure 5.9b-c show the same graphs for the difference between spectrum evolutions in TT2-TT1 and TT1-CSI03 respectively. Again, during experiment B, the time periods of Mar 23-25, Apr 8-11 and Apr 16-19 represent southerly winds while there was significant dissipation of high frequency waves. It is evident that fetch variation alone could not fully explain the energy evolution of high frequency sea waves, rather complex interaction with bottom suspended materials also should be accounted for both low and high frequency wave dissipation over the shoal complex.

The seafloor response to hydrodynamic forces during the deployments is also of interest. The sediment samples collected before experiment A showed a thick layer of fluffy mud over TT1 (Tiger Shoal) site, while the samples collected during the retrieval survey was dominated with shell and shell hash. The LMBS and hydrodynamic bottom can be used as a proxy to monitor seafloor variation, especially when the direct measurement of the bottom would be extremely difficult. Those estimates for TT1 site during experiment A are shown in Figure 5.3j. Note that the high concentration of sediment in water column may result in dissipation of signal before bed level and velocity estimation becomes unreliable for deeper levels. In such conditions, there is a big gap between LMBS and hydrodynamic bottom. In addition, on hard bottom in which the acoustic signal cannot penetrate into bed substrate, the maximum backscatter happens at the same level as zero velocity level.

The movement of bed material should be related to physical forces exerted on the bottom particles. The algorithm of Soulsby and Clarke (2005) was employed to estimate bed shear stress. The root mean square value of shear stress over wave cycles was used as a general measure of forces on sediment particles during random waves (Soulsby and Clarke, 2005; Whitehouse et al., 2000) and D_{50}=6 μm was used for experiment A. As shown in Figure 5.10a, the shear stress is high after few hours of deployment in experiment A, and exceeds 0.4 (Nm^{-2}) at late hours of Dec 4. At this time, there is a strong northward bottom current (Figure 5.3g,i) which might have flushed away the fine grain sediments. Therefore, the LMBS estimate of bottom coincides with hydrodynamic bottom after the Dec 5 storm event (Figure 5.3j). The only exception was few hours before and after Dec 10, when the computed shear stress reached its maximum value for the entire deployment in experiment A. High bottom shear stress at the early phase of cold front could move shell particles and let the finer grain sediments beneath them to release in water column, and produce a high concentration of suspended sediment close to bottom. These suspended sediments were swept southward by strong southward bottom currents, associated with the post-frontal northerly wind regime. Although not shown here, the change in bed level in TT1 was confirmed by the increase in mean water level difference between CSI03 and TT1 that happened after Dec 5. Because the CSI03 pressure sensor was connected to a stable rig of an oil platform, the change in mean water level difference can be interpreted as increase in water depth at TT1, which occurred due to erosion of mud layer.

The similar shear stress estimates for experiment B are presented in Figure 5.10b-c in which D_{50}=0.4 and 0.12 mm were selected for median grain size at TT1 and TT2 respectively,

based on pre- and post-deployment sediment samples. Relatively stable bottom at TT1 (Figure 5.7k) is in agreement with high concentration of shell in sediment samples before and after deployment. However, bed sediments at TT2 site was predominantly fine sand, and showed evidences for undergoing series of deposition and resuspension, during experiment B. Most of the peaks of high sediment suspension close to bed was in tandem with LMBS (Figure 5.7l) coinciding with high values of shear stress (see Figure 5.10c) and followed by a corresponding change in bed level. These depositional events happened in the early stages of the deployment when northerly wind, generated during the post-frontal phase of cold front passage, produced strong southward current in the entire water column, which also suggested that the sediment was brought in from farther north of the Trinity Shoal. However, on March 23, the bed level showed a noticeable elevation when strong southerly winds (see Figure 5.7a) generated relatively high waves (Figure 5.6b), and the northward bottom current exceeded 0.3 m/s. It is concluded that the sediment source of this level change might be originated from the Trinity Shoal itself.

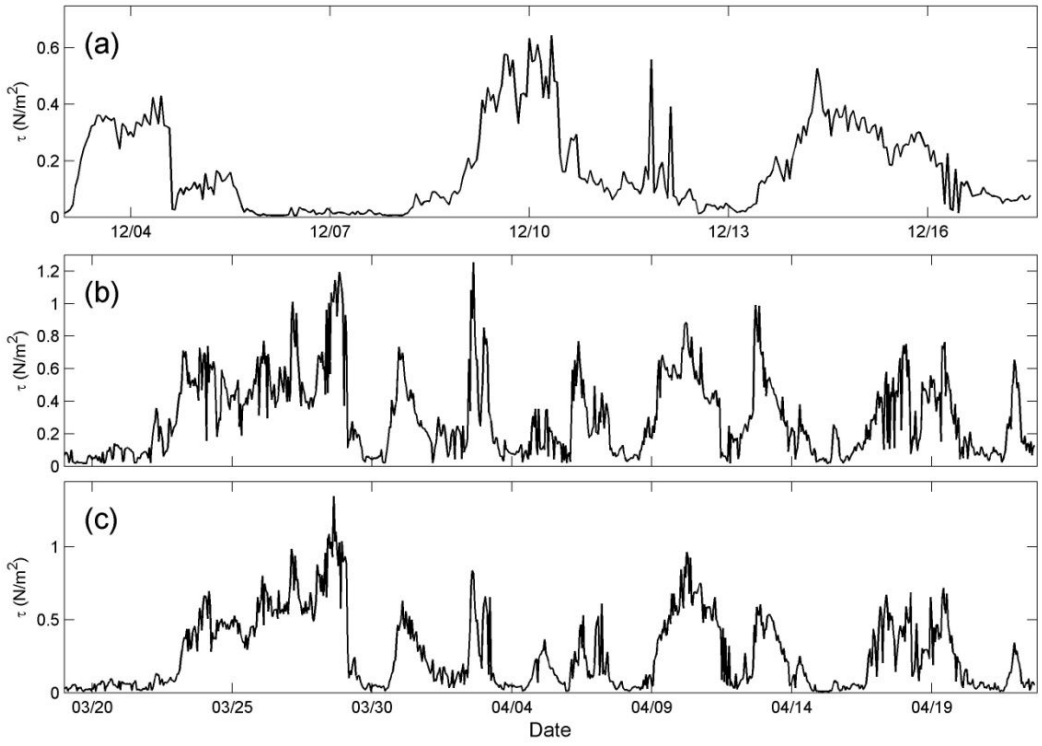

Figure 5.10: RMS values of shear stress (from waves) computed at a) station TT1 during experiment A; b) same station TT1 during experiment B; c) TT2 during experiment B.

Comparison of shear stress (Figure 5.10a) and SSC (Figure 5.5g-h) shows that the time period of high shear stress is in good agreement with the time period of high SSC, during experiment A. High values of shear stress can be caused by energetic southerly waves such as

during Dec 14-16, or pre-front waves such as on Dec 3 or Dec 9, and continued by high current speed and energetic high frequency waves generated by cold front passage events such as on Dec 4 or Dec 10-12.

During experiment B, at both Tiger and Trinity stations (TT1 and TT2), the suspended sediment concentration close to the bed, recorded by optical instruments (OBS at 25 and 60 cmab), differed significantly from corresponding acoustic estimates by PCADP (see SSC values in Figure 5.7g-i after March 26). The OBS sensor detects the sediments which are at most 20 cm away from sensor head (depending on the signal attenuation) and in its view angle (Downing, 2006) while the PCADP detects the particles within the corresponding cells (3 cm thick in the setup used in this study). However, the difference between SSC pattern and values suggests that different sampling volumes cannot explain the difference in SSC estimates of a PCADP and OBS. It is important to note that the backscatter echo of the PCADP did not follow linear regression with logarithm of SSC recorded at OBS level after March 26; therefore only the data from the first few days of deployment were used for PCADP inversion algorithm described in section 5.3.

The inconsistency between SSC estimates of PCADP and OBS possibly originated from the physical principles of these instruments and their limitations. Optical instruments are sensitive to cross-section of suspended particles while the acoustic instruments sense the particle volume (Ha et al., 2011; Lynch et al., 1994). Using the OBS reading from a settling tank experiment, Lynch et al. (1994) demonstrated that sensitivity of OBS to smaller particles led to overestimation of SSC. They suggested that for a mass concentration of a mixture of n classes of particle sizes, a factor proportional to a_n^{-1} was required to adjust the OBS reading, in which a_n was the representative particle radius of corresponding class. The sensitivity of OBS to particle size is reported by others too (Downing, 2006; Fugate and Friedrichs, 2002). The acoustic instruments had more complex response and needed an adjustment factor proportional to $f_n^2 a_n^{-1}$ in which f_n was called "form factor", which was a function of ka_n in which k was acoustic wave number. The functionality of the form factor on ka_n may result in drastic underestimation of acoustic estimates of SSC for smaller particles (Lynch et al., 1994; Thorne and Hanes, 2002). Using simultaneous measurement of particle size by a Laser In Situ Settling Tube, Lynch et al. (1994) showed that the ratio of optical and acoustic estimate of SSC is related to the change in the dominant size of suspended particles in water column.

Decrease in representative grain size at the beginning of a cold front passage is unexpected since the increase in shear stress usually results in suspension of coarser particle size. Several hypotheses can be assumed for such a decrease in particle size in water column before peak shear stress is attained. The presence of larger and lighter particles over finer and denser ones can result in such phenomena (Lynch et al., 1994). However, the extensive array of vibracore samples taken by Roberts et al., (2010) from Tiger and Trinity Shoals, with some locations in the near proximity to stations TT1 and TT2, do not support this assumption.

Another possibility is the condition in which fine particles from the surface layer of the bed were eroded by comparatively low energy events before March 26, and by erosion of coarser material on top, a deeper layer of fine materials are now exposed. However, relatively stable bottom at TT1 and depositions at TT2 are in contradiction with this hypothesis.

It is also possible to assume that the fine grained sediments from the river plume and resuspended cohesive material south of Marsh Island were brought southward, and retained in suspension for a longer time as observed by Sheremet et al. (2005) at CSI03, during Hurricane Claudette. A few clear true color images of MODIS satellite (not presented) processed by Earth Scan Lab, Louisiana State University (www.esl.lsu.edu) showed southward incursion of river plume, resulted in high surface SSC from March 28 to April 14. The peak in sediment load of the Atchafalaya River during experiment B happened in March 20-30 (exact peak on March 25) as shown in Figure 5.2, which could provide considerable amount of fine grained sediment into the wider Atchafalaya Bay/shelf. Therefore, the source of unconsolidated fine grained sediment was available at the northern boundary of the shoal complex, during experiment B. The high concentration of suspended fine grained sediments can result in the disparity between the performance of PCADP and OBS, due to the limitations of the particle size that can be detected by acoustic devices such as PCADP. Acoustic response of sediments having particle radius of a_p is maximum when $ka_p = 1$. The acoustic SSC estimation is inappropriate beyond this limit because the Rayleigh scattering model utilized in the computation with the assumption of SSC calculation is not valid for too large particles (Gartner, 2004; Reichel and Nachtnebel, 1994). The backscatter signal decreases drastically as ka_p decreases and the acoustic estimation of SSC is not appropriate when ka_p is too small. The values between 0.01-0.1 were suggested as a limit for minimum ka_p (Ha et al., 2011; SonTek, 1997; Urick, 1983) and we used 0.05 in this study as suggested in SonTek (1997). Therefore, for 1.5 MHz PCADP, the particle diameter outside the range of 0.016-0.32 mm cannot be efficiently sensed. Specifically, if the diameter of the particles in suspension is much smaller than 16 μm, they cannot be detected by PCADP, while heavily influence the OBS readings. It was confirmed by Ha et al., (2011) that PCADP was not an effective instrument to estimate SSC when kaolinite (D_{50}=2 μm) was mixed with fine sand.

In addition, the shear stress at TT1 and TT2 (Figure 5.10b-c) is better correlated with PCADP-derived SSC (Figure 5.7g-i) than OBS-derived estimates. This correlation is additional evidence to support the hypothesis of the advection of fine grained sediments from elsewhere, which were not locally eroded. These advected fine particles skewed the observations of SSC from OBS, leading to over estimation while hardly detected by acoustic instruments such as PCADP. However, the suspended sand particles on the shelf, which is a response to the bottom stress, were detected by PCADP.

In order to detect smaller particles than 16 μm, an instrument with higher frequency is needed. The ADV at TT2 during experiment B worked with 5 MHz frequency and can be used

to detect the particles in the size range between 0.005-0.096 mm. Unfortunately, the OBS at 25 cmab at TT2 malfunctioned, but it was still possible to calibrate the ADV with SSC estimated at 32 cmab from PCADP during March 19-26. The estimated SSC of ADV and PCADP are shown in Figure 5.11. Since ADV estimates were highly correlated with SSC estimates from PCADP for entire duration of experiment B, and do not show better correlation with the patterns of OBS readings in Figure 5.7i, it is assumed that fine grained suspended sediments should be smaller than 5 μm. Also, lower values for the estimates of ADV, in comparison to PCADP, suggest that resuspension of local sand particles with D_{50} close to 10 mm can be better sensed by the PCADP than the ADV.

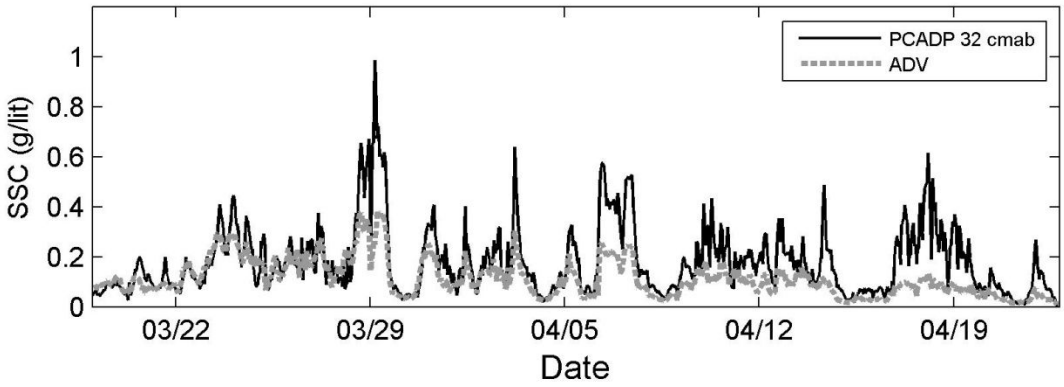

Figure 5.11: Suspended sediment concentration at TT2 during experiment B, estimation based on ADV and PCADP back scatter intensity at 32 cmab.

5.6 Conclusions of Chapter 5

The monitoring of meteorological, hydrodynamic and bottom boundary layer parameters during two weeks of measurement from Tiger Shoal, and a WAVCIS station south of Marsh Island (CSI03), during a low discharge period of Atchafalaya River (experiment A); and an extended survey (35 days) for the entire Tiger and Trinity Shoal complex yielded the following conclusions:

The rapid change in wind speed and direction during the passage of cold fronts resulted in abrupt change in waves, currents, water level and other hydrodynamic parameters as well as bottom boundary conditions. Strong and persistent current profiles were measured by PCADP and ADCP at all stations during cold fronts, from both experiments. Energetic high frequency waves (with frequency of approximately 0.3 Hz) from north became the dominant wave component during the frontal passage, while during pre- and post-frontal conditions, the southerly waves with lower frequency were dominant (0.13 Hz). The salinity at 1 m above the bottom from Tiger Shoal showed strong influence of the Atchafalaya River plume on the

hydrodynamics and mixing over the shoal, during cold front events monitored during experiment B. However, the salinity fluctuation was minimum at the Trinity Shoal deployment site.

Before experiment A, Tiger Shoal was covered by a "fluffy mud" layer, while sediment samples collected during the retrieval cruise revealed a substrate of shell and shell hash. The change in physical forcing also resulted in resuspension of bed sediments, as detected by the maximum reflectance level and the hydrodynamic bottom determined by PCADP. During experiment B, the Tiger site showed relatively stable bed which was in agreement with shell dominated sediment samples collected before and after deployment (more than 80% shell and shell hash). On the other hand, the PCADP at Trinity Shoal detected several stages of erosion and deposition phases. The passage of each cold front during experiment B resulted in few centimeter of net deposition at this site located on the northern flank of the shoal. The sediment samples were dominated by fine sand with slightly more fine sediments collected at the end of experiment B.

During both experiments, several time periods were identified in which energy of short period waves, in the frequency range of 0.25-0.4 Hz, were dissipated considerably over the shoals, while no significant change in the of dissipation was observed between sea and swell waves. The dissipation of southerly long period waves, in the frequency range of 0.1-0.2 Hz, could be explained by dissipation with bottom interaction. However, some other mechanism is needed for dissipation of high frequency waves, because these waves interact weakly with the bottom. High concentration of suspended sediment close to bottom and extension of sediment plume to the southern boundary of the shoal complex, as observed from MODIS true color satellite images, suggested that the mud-wave interaction could be responsible for the dissipation of high frequency waves. The Nonlinear triad wave-wave interaction may also enhance the dissipation of high frequency waves by transferring the energy to low frequency components which have more interaction with mud layer close to the bed. This assumption is evaluated in more details in Chapter 6.

Using two weeks of measurement in experiment A, the performance of a PCADP and an ADCP for measuring wave parameters from the Tiger Shoal complex, especially during cold front events, were compared. Results showed that strong non-uniform current profile and the velocity ambiguity were responsible for some data discrepancy observed from the two sensors. Based on the data from experiment B, the performance of an ADV and a PCADP were compared from Trinity Shoal. The results confirmed that the data mismatch from two instruments happened when suspicious jumps were recorded in burst samples, which were used to produce the wave spectrum; and therefore indicating the same conclusion about ambiguity velocity algorithm used in PCADP. In order to solve this problem, the resolution velocity should be calculated based on a closer cell to the sensor than 60 cm used in these deployments.

Estimation of suspended sediment concentration based on PCADP and OBS data were in good agreement in the first deployment, but significantly deviated in the second deployment,

especially after the peak in sediment load of Atchafalaya River discharge. Suspension of very fine particles which may be transported to the study area directly by the Atchafalaya River or resuspended at the north of the study area could be responsible for overestimation of OBS, while the PCADP cannot detect these fine grained particles. Because the ADV estimate of SSC was not better than the PCADP, those fine grain particles should be smaller than 5 μm. The simultaneous monitoring of particle size in the water column, along with wave and current measurements would help in the future to fully understand the bottom boundary layer dynamics and its implications on shoal sediment resuspension and distribution, especially during high energy events like cold fronts passing through the area.

CHAPTER 6: SIMULATION OF WAVE DAMPING DURING A COLD FRONT OVER THE MUDDY ATCHAFALAYA SHELF

6.1 Introduction

Third generation wave models calculate the evolution of wave spectra without any pre-assumed form for the sea or swell part of the spectrum. These phase averaged wave models are based on the wave action balance equation for wind waves with ambient currents (Whitham, 1965), and is given by:

$$\frac{DN}{Dt} = \frac{S_{tot}}{\sigma} \tag{6.1}$$

in which $N \equiv E/\sigma$ is wave action density, E is wave energy density, $\sigma = 2\pi f_r$ is the angular relative frequency, and S_{tot} denotes the total of source/sink terms. In deep water, the energy exchange between wind and waves, quadruplet wave-wave interaction and energy dissipation are the main components of S_{tot} (Komen et al., 1994). However, when waves propagate across intermediate and shallow waters, nearshore processes such as bed friction become important (Graber and Madsen, 1988). The rate of energy dissipation over non-cohesive bottom is roughly estimated as a few watts per square meter. This rate is approximately the same as the rate of wind energy transferred to waves during moderate wind speeds (Cavaleri et al., 2007).

The general formulation for bottom friction term in phase averaged wave models is as follows (Weber, 1991):

$$S_{fric} = -C\frac{k}{\sinh(2kh_w)}E \tag{6.2}$$

in which k is wave number and h_w is water depth. The friction coefficient C varies for different formulations that have been suggested. In the simplest form, it can be considered as the constant value of 0.038 m^2s^{-3} for swell waves (Hasselmann et al., 1973) and 0.067 for sea waves (Bouws and Komen, 1983). However, the friction coefficient is not constant in reality and depends on wave-induced bed velocity (Young and Gorman, 1995). In the eddy-viscosity model of Madsen et al. (Madsen et al., 1988), the friction coefficient is given as follows:

$$C = \frac{g}{\sqrt{2}} f_w U_{rms} \tag{6.3}$$

where U_{rms} is the root mean square bottom orbital velocity, and f_w is the friction factor which depends on the near-bottom excursion amplitude and the bed roughness height, K_N. The realistic value for K_N depends on ripple formation for sandy bottoms and varies between 0.02-

20 cm. The calibration process suggested $K_N = \mathrm{O}(1)$ cm to be used in wave models (Tolman, 1991).

In the case of a soft muddy bottom, waves are reported to be attenuated at a much faster rate than the rate predicted using equation (6.2) in the wave model (e.g. Gade (1958)). When shear stress (induced by waves and background current) exceed the critical value of the local bed, liquefaction of part of the seabed occurs. The flocculation and slow deposition of the cohesive suspended sediment form a fluid mud which dissipates the energy of internal wave at the interface of mud and water, predominantly by internal friction (Winterwerp et al., 2007). Gade (1958) simplified the problem by assuming a layer of non-viscous water over a viscous fluid mud layer. However, the hydrostatic assumption in both layers limits the application of his model to long waves in very shallow water.

Several extensions of the model suggested by Gade (1958) have been proposed to include non-hydrostatic effects as well as viscosity in the water layer (Dalrymple and Liu, 1978; De Wit, 1995; Ng, 2000). Note that the effect of water viscosity on the dissipation is typically negligible compared to energy damping within the lower layer (Dalrymple and Liu, 1978). In addition to the viscous Newtonian fluid models, several other theoretical descriptions of wave damping by fluid mud are also available in the literature based on different assumptions about mud rheology; such as visco-elastic (Macpherson, 1980), Bingham-plastic (Mei and Liu, 1987) or poro-elastic model (Yamamoto et al., 1978). However, Winterwerp et al. (2007) argued that these models are based on the mud effects which are small or in a short period of time compared to a typical storm period. Therefore, the damping of wave energy in the lower layer by viscous fluid mud is the main mechanism of wave attenuation in the presence of fluid mud.

In recent years, inclusion of a mud-induced dissipation term to wave models has been studied for both phase resolving and phase averaged models (Kaihatu et al., 2007; Kranenburg et al., 2011; Rogers and Holland, 2009; Sheremet et al., 2011; Winterwerp et al., 2007). The formulations of Gade (1958) and Ng (2000) are of special interest because their dispersion equations are explicit. The better performance of wave models with a mud-induced dissipation term was reported for the simulations of wave propagation over muddy coasts of Cassino Beach, Brazil (Cuchiara et al., 2009; Rogers and Holland, 2009) and Louisiana, USA (Kranenburg et al., 2011). In those studies, the SWAN model (Booij et al., 1999) was used in stationary mode. In some cases, modeling of the transformation of the swell-type waves from the offshore boundary was their main focus. However, the main objective of this study is to quantify the interaction of locally generated, high frequency waves (sea waves) and fluid mud along the west coast of Louisiana, during a typical cold front condition, using the SWAN model.

The field study is shown in Figure 6.1a which is close to the Atchafalaya-Vermilion Bay system, the largest estuary along the Louisiana coast, receiving between 15-30% of the total flow of Mississippi River and nearly 40-50% of its suspended sediment load through the lower Atchafalaya River and Wax Lake outlets (Allison et al., 2000; Mossa and Roberts, 1990). Based

on the river discharge data at Simmesport station, LA (160 km north of Marsh Island) archived over the 1952-1989 period, the average suspended sediment load of Atchafalaya River is 84 million tons per year, which includes 17% sand (Allison et al., 2000). Away from sand shoals (e.g. Tiger and Trinity Shoals shown in Figure 6.1a) and oyster reefs on the inner shelf adjacent to Marsh Island, the mean particle diameter of bottom sediments is 2-7 μm, which is the same as the size of suspended particles from the lower Atchafalaya River (Sheremet et al., 2005; Wells and Kemp, 1981).

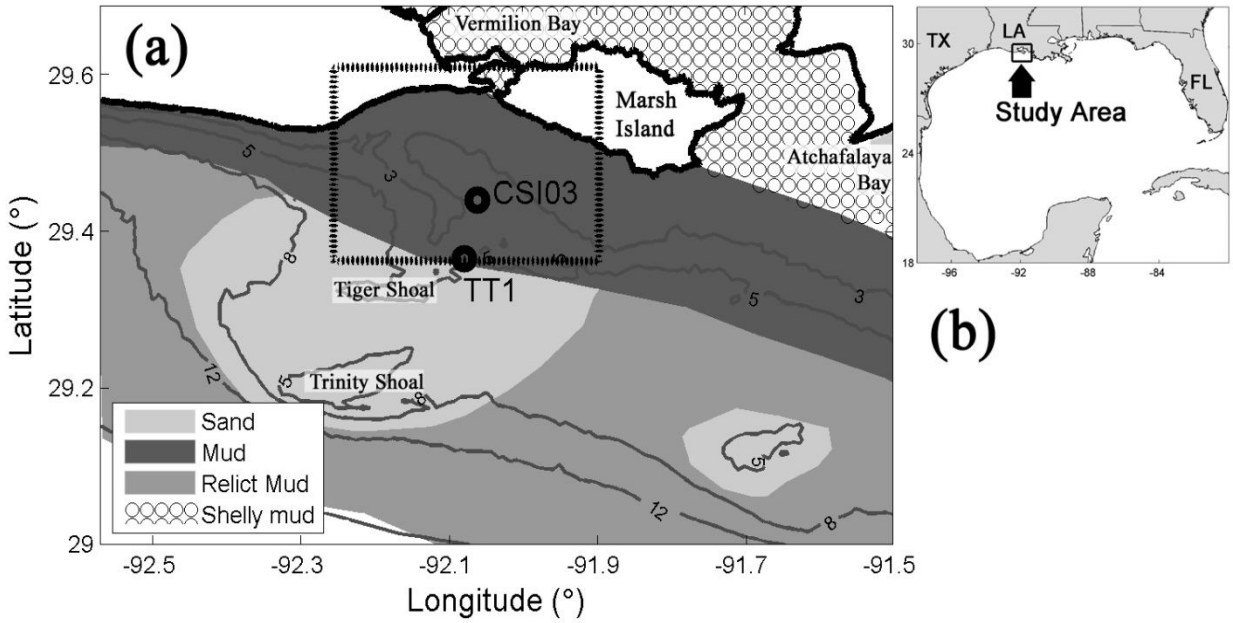

Figure 6.1. a) The study area, Atchafalaya Bay and the surrounding shelf. The location of deployment sites at the Tiger Shoal and CSI03 station are also shown. The shadings represent a qualitative extension of various sediment types in the Atchafalaya shelf, modified from Neill and Allison (2005). The dotted rectangle represents the approximate computational domain of SWAN; b) the location of the study area with respect to the Gulf of Mexico.

The turbid plume exiting the Atchafalaya bay system, which is advected to the west along the Louisiana coast, is referred to as "mud stream" (Wells and Kemp, 1981). The mud stream is confined to water depths of less than 10 m (Kineke et al., 2006), moving westward due to a sustained westerly low frequency circulation of Texas-Louisiana shelf during non-summer months (Cochrane and Kelly, 1986). During the passage of cold fronts over the Atchafalaya Shelf, which occur every 4-7 days in winter/spring seasons, the wind direction changes clock-wise from pre-frontal southeast direction to south, west, and eventually to north. Westerly winds disrupt the westward movement of the mud stream and Ekman transport contributes to extending

the sediment plume farther to the south. The prefrontal water level set-up along the Atchafalaya Bay would also be released once the front crossed the region (Feng and Li, 2010). Sustained northerly wind during the cold fronts facilitates the rapid seaward flushing of sediment-laden plumes from the Atchafalaya River and Wax Lake outlets (Walker and Hammack, 2000). Based on data from a transect south of Marsh Island, Allison et al. (2000) showed that during early stages of a frontal passage, the suspended sediment concentration (SSC) in the entire water column can exceed 1 g/l in water depth shallower than 5 m. After a few hours of wind speed weakening, accumulation of sediments close to bed can form a fluid mud with concentrations of more than 25 g/l.

The presence of the mud stream significantly influences the wave characteristics of the western Louisiana coast. By deploying an array of wave sensors approximately 70 km west of Marsh Island, Elgar and Raubenheimer (2008) demonstrated the rapid dissipation of wave energy when it propagates across the Atchafalaya mud stream. Simultaneous measurement of waves and SSC from an offshore station on Atchafalaya shelf (CSI 03 in Figure 6.1a) showed that SSC could reach 0.5 g/l, throughout the water column, during the passage of Hurricane Claudette. During the waning phase of the storm, sediments accumulated at bottom layers of the water column and a persistent high SSC remained at 1 m above the bottom (mab) (Sheremet et al., 2005). Sheremet and Stone (2003) compared the time series of wave height and period measured at CSI03 with another station located 150 km southeast of the Atchafalaya-Vermillion Bay system in a sandy environment, having the same depth. They found that mud-induced dissipation affects not only the long waves but also the high frequency waves, which in turn interact scantly with the sea bottom.

If fluid mud is formed close to coast during the passage of a cold front, and mud-induced dissipation is able to effectively dissipate high frequency waves, then the wave growth rate simulated by a wave model during the northerly winds of a cold front event should be overestimated. Evaluating this hypothesis is the first objective of this study. Moreover, it is relevant to see whether the inclusion of mud-induced energy dissipation term to the model would improve the simulated wave spectrum, compared to observed data, and how this improvement is different from manipulating the non-cohesive bed friction term available in the model. Estimation of rheology and mud distribution required to reproduce the *in situ* observation during a cold front passage is the final objective of this study.

To achieve these goals, the wave information at CSI03 is used because this station has enough fetch against northerly wind for wave growth, and it is also located in the muddy environment. In order to include the effects of southerly swell in the wave modeling, a tripod is deployed further offshore in a non-cohesive environment (approximately 8 km south of CSI03). A brief explanation of instrumentation used in this study is presented in section 6.2. The methodology of this study and the model used here are described in section 6.3. The results of simulations are presented in section 6.4. Several discussions on the results and methodology are given in section 6.5, and conclusions in section 6.6.

6.2 Experimental Setting

The upper water column at the TT1 station shown in Figure 6.1a was monitored using an upward looking 1200 kHz RDI workhorse ADCP. A downward looking SonTek 1.5 MHz PCADP was also deployed to record high resolution velocity profiles close to the bottom. Both instruments had inbuilt pressure sensors which provided the water depth variation.

Inshore the TT1 station, a permanent observation station noted as CSI03 in Figure 6.1a, provided the meteorological as well as hydrodynamic conditions close to the shore. This station is part of the Wave, Current and Surge Information System (WAVCIS), designed to provide continuous observation of met-ocean conditions from the northern Gulf of Mexico (Stone et al., 2001). Note that wind speed and direction were measured approximately 24 m above the water surface; and were converted to the equivalent neutral wind, following the method of Liu and Tang (1996). The instrumentation at CSI03 and TT1 used in this study is summarized in Table 6.1. Although wave measurements were available for more than 1 month, the failure of the wind sensor on April 1 2009 limits this modeling study to the first 13 days of deployment.

Table 6.1, Different instruments used at CSI03 and TT1 tripod

Location	Instrument	Purpose	Considerations
CSI03	ADCP	Hourly wave and current data	2048 samples at2 Hz frequency, bin size was 0.5 m and the sensor head was located 0.5 mab
	Pressure sensor	Hourly wave data	2048 samples at2 Hz frequency, located 2 mab; failed on March 24 2009
	Meteorological sensors	Hourly wind vectors, air and water temperature, humidity and barometric pressure	Sampled at 1 Hz for a 10 min period and the average values were recorded; failed on April 1 2009
TT1	ADCP	10 minute-averaged current every 20 minutes	Sensor head at 0.75 mab, bin size was 0.25 m; failed on March 25 2009
	PC-ADP	Hourly wave, and bottom boundary layer data	2048 samples at 2 Hz frequency, The Transducer head was approximately 1.1 mab, with 37 bins of 3.3 cm wide starting from 15 cm below the sensor.

6.3 Method

6.3.1 Implementation of Mud-induced Wave Damping in SWAN

Kranenburg et al. (2011) assumed a viscous two-layer model in which a non-viscous non-hydrostatic fluid moves over a viscous hydrostatic lower layer. The mud-induced dissipation

term, S_{mud}, was derived as a function of the real part of the pressure variation on the interface, $\hat{\rho}_{1,z=h_m}$, the amplitudes of surface, a, the interface displacements, b, and their phase difference, φ, as given by the following equation:

$$S_{mud} = -\sigma \frac{\mathrm{Re}\{\hat{\rho}_{1,z=h_m}\}}{\rho_w g a} \frac{b}{a} \sin\varphi \; E \tag{6.4}$$

Their model assumed that the viscous dissipation is the main mechanism of energy damping in the mud layer and the effects of elasticity and plasticity are negligible. Kranenburg et al. (2011) also showed that their model can reproduce the results of the models suggested by Gade (1958) for shallow water depth, by Ng (2000) for small relative mud thickness, and by Dalrymple and Liu (1978) for large relative mud thickness in deep water.

In order to solve the implicit dispersion relation for a complex wave number, Kranenburg et al. (2011) used an algorithm based on Argand diagrams in which viscosity was assumed to be equal to zero at the starting point, and increased by a small value at each step until it reached its proper value. The solution of the previous step was used as a starting point for solving the dispersion equation using the DZANLY routine of IMSL commercial package (Kranenburg, 2008). This method is accurate but time-consuming and cannot be used for performing an efficient non-stationary simulation in which the solution of dispersion relation is required for each time step. In this study, the dispersion equation of Kranenburg et al. (2011) is modified as follows:

$$\begin{aligned}
&\sigma^4\left(\frac{1}{k_c} - \frac{\rho_w}{\rho_m}\frac{\tanh k_c h_w \tanh m h_m}{m} + h_m \frac{\rho_w}{\rho_m}\tanh k_c h_w\right) + \sigma^3 2ik_c\nu_m\left(1 - \frac{1}{\cosh m h_m}\right) \\
&+ \sigma^2 g\left(\frac{k_c}{m}\tanh m h_m - k_c h_m - \tanh k_c h_w\right) + \sigma 2igk_c^2\nu_m \tanh k_c h_w\left(\frac{1}{\cosh m h_m} - 1\right) \\
&+ g^2 k_c^2 \tanh k_c h_w\left(1 - \frac{\rho_w}{\rho_m}\right)\left(h_m - \frac{\tanh m h_m}{m}\right) = 0
\end{aligned} \tag{6.5}$$

in which k_c is complex wave number, ν_m is the viscosity of mud layer, h_m and h_w are the thicknesses of mud layer and water layer respectively, ρ_m and ρ_w are the densities of mud layer and water layer respectively, and $m = (1-i)\sqrt{\sigma/2\nu_m}$ where $i = \sqrt{-1}$. Although this equation is mathematically equivalent to equation (25) of Kranenburg et al. (2011), it has the advantage that the iterative method of Müller (e.g. Press et al. (1992)) can solve it with only few iterations. The Müller's method requires three initial values for starting the iterations. The first starting value is created from explicit solution of the dispersion equations of Gade (1958) and Guo (2002) using the equation suggested by Kranenburg et al. (2011). The next two starting values are obtained by solving equation (6.5) using Newton's method with only two iterations. Moreover, in case of a very thin layer of mud, the explicit formulation of Ng (2000) is a better starting value for the

iterations than any of the values predicted by Gade (1958) or Guo (2002). Therefore in the proposed algorithm, whenever h_m / h_w exceeds 0.05, the formulation of Ng (2000) is used for iterations.

Using this algorithm, the computational effort required to solve the dispersion equation (6.5) is reduced by two orders of magnitude. Since the calculation required for the mud-induced dissipation term with previous algorithm is the most time-consuming part of the code, the new algorithm significantly improves the efficiency of the model.

The SWAN version 40.51 was used originally to test the implementation of mud-dissipation in stationary mode (Kranenburg, 2008). In order to benefit from new bug fixes and modifications in the newer versions of SWAN, the code version 40.85 was employed in this study. The new code was tested against the propagation test cases shown in Kranenburg et al. (2011).

The code was further modified to solve the two-layer dispersion equation at each time step in the non-stationary mode. The implementation was verified by reproducing the same results for asymptotic non-stationary simulations and corresponding stationary simulations for different configuration of wind and boundary waves for the same computational domain.

6.3.2 Wind Sea and Swell Separation

It is worthwhile to distinguish between the components of waves which are locally driven by wind (wind sea) and the components which have been generated far offshore (swells). In order to separate different wave components, the wave partitioning procedure of Hanson et al. (2009) was employed. As a first step, the spectrum was partitioned to isolate the spectral peaks and then, following Hanson and Phillips (2001), the next wave age criteria was used to distinguish between wind sea and swell waves:

$$c_p \le (1.5) U_{10} \cos\delta, \qquad 0 \le \delta \le \frac{\pi}{2} \tag{6.6}$$

in which c_p denotes wave phase speed, U_{10} is wind speed at 10 m above mean sea level, and δ is the angle between wind and wave components.

During the passage of cold fronts, the wind veers rapidly and another criterion is needed to distinguish between wind seas and young swells, which are recently released from the influence of wind forcing. Following Hanson and Phillips (1999), the wind sea component should maintain energy above a threshold level estimated by the equilibrium range theory of Phillips (1985). Finally, all wind sea peaks and swell peaks are combined to have one wind sea zone and one swell zone. An example of this algorithm is shown in Figure 6.2, which shows that wind from northwest generates the wind sea while the southerly low frequency swell waves are still present. After extracting the sea and swell zones in spectral domain, the same zones were used to calculate simulated sea and swell wave height from the modeling results.

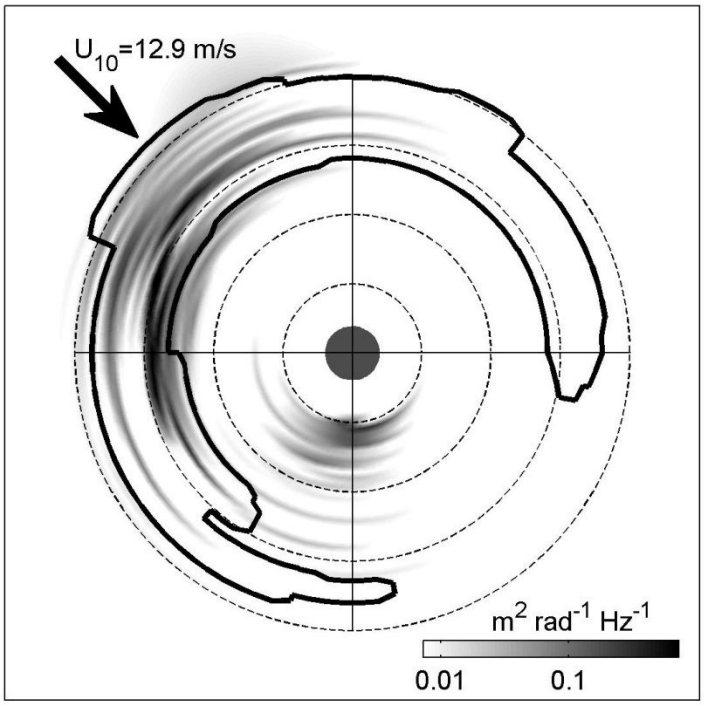

Figure 6.2. Wind sea and swell partitions of the wave spectrum measured by ADCP at CSI03 at 08:00 GMT, March 28 2009 are separated by solid curve. The arrow shows the dominant wind direction, and the dash lines correspond to frequencies of 0.1, 0.2, 0.3 and 0.4 Hz.

6.3.3 Modeling Setup

The computational domain of the wave model is shown in Figure 6.3 with dash lines. The hourly measured wave spectra at TT1 were used as a uniform boundary condition at the southern boundary of the domain. The hourly wind speed and direction at CSI03 was also assumed to be uniform for the entire domain. The grid sizes in the north-south direction and the west-east direction were 300 and 450 m respectively. A grid sensitivity test showed that chosen spatial resolution had no effect on the model results. Similar analysis showed that a time step as small as 60 second was required during wind turning.

The WAM cycle 4 package of SWAN was employed for energy input from wind and energy dissipation by the whitecapping. The nonlinear quadruplet wave-wave interaction was estimated by the Discrete Interaction Approximation formulation (DIA) (Hasselmann et al., 1985). The linear wave growth term of Cavaleri and Rizzoli (1981) was also activated to provide more realistic results in early stages of wave development. Moreover, the nonlinear triad interaction and the depth-induced wave breaking were considered according to Eldeberky (1996) and Battjes and Janssen (1978) respectively (see section 6.5.3). As explained in section 6.1, the bed friction formulation of Madsen et al. (1988) required the estimation of bottom roughness length scale, and the value of $K_N = 0.01$ m was selected based on calibration.

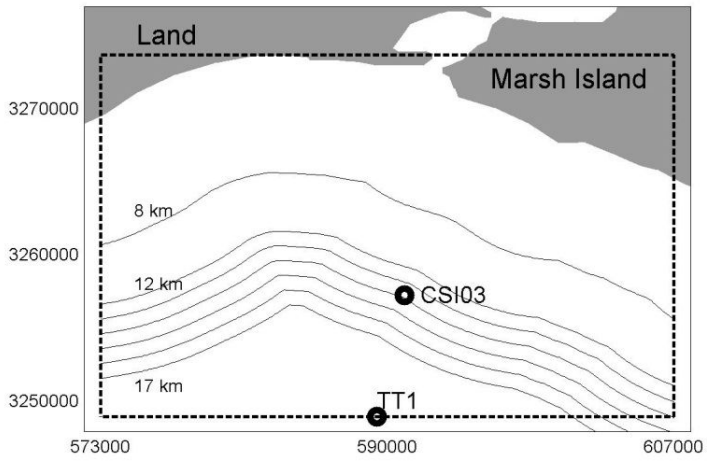

Figure 6.3. Computational domain used for wave modeling. Different assumed seaward extensions for mud layer are shown with black lines. The coordinate system is UTM 15.

The mud-induced dissipation term also requires density, kinematic viscosity, and thickness of mud layer as well as its spatial extent. According to Wells (Wells, 1983), the fluid mud zone extends to 5-8 km offshore in the west of the study area. Since cold fronts push the sediment from Atchafalaya River southward (Walker and Hammack, 2000), it is expected that the fluid mud would be found further offshore. As shown in Figure 6.3, seaward of the zone of fluid mud was assumed to have the same distance (X_m) from the coastline in the study area, but several values were assumed for X_m. Based on similar studies on wave-dissipation by fluid mud (Elgar and Raubenheimer, 2008; Kranenburg et al., 2011; Rogers and Holland, 2009; Sheremet et al., 2011; Winterwerp et al., 2007), different values for each of the aforementioned mud parameters were assumed as summarized in Table 6.2. Note that for simulations which include wave damping term, the non-cohesive bed friction term was activated outside of the zone of fluid mud.

Table 6.2. Different values used for parameters needed for inclusion of mud-induced dissipation term in SWAN

ν_m (m^2/s)	X_m (km from coastline)	h_m (m)	ρ_m (kg/m^3)
0.0001, 0.001, 0.003, 0.01, 0.1, 0.3	12, 13, 14, 15, 16, 17	0.05, 0.2, 0.3	1080, 1300

Current speed and water level in the domain varied during the cold front. The mean current speed exceeded 0.5 m/s during the cold front passage of March 2009. It was important to

include wave-current interaction in the wave model to include the Doppler shifting effect of current on high frequency sea waves in the wave model. The simulation result of MIKE21 was used to provide these data for SWAN. Details of the hydrodynamic model and its calibration were discussed in Stone et al. (2012).

6.4 Results

The wind vectors measured at CSI03 during the deployment are presented in Figure 6.4a. Note that this time period consisted of an extensive southerly wind system beginning March 22. It was interrupted with brief northerly wind fronts March 26 and 27 for a few hours. The cold front crossed the coast on March 28 and continued for two days until the southerly wind again prevailed over the study area.

The measured wave height at CSI03 and the corresponding simulated results from SWAN using a non-cohesive bed friction formulation are shown in Figure 6.4b. Although the model is in fairly good agreement with the field dataset in general, there are several time periods in which the model could not reproduce the measured wave height. The periods of discrepancy in wave heights labeled as (II) and (III) were few hours in which northerly wind intruded and the assumption that the measured wind at CSI03 was a good representative of the entire domain was most likely not valid. The wind during the time period labeled as (I) was weak, and a non-uniform spatial structure of wind as well as a low signal-to-noise ratio for buoy data could explain the overestimation of the model. However this could not explain the overestimation of simulated wave height for the periods labeled as (IV) and (V), because the strong northerly wind persisted during March 28-29, and the wave height was relatively large.

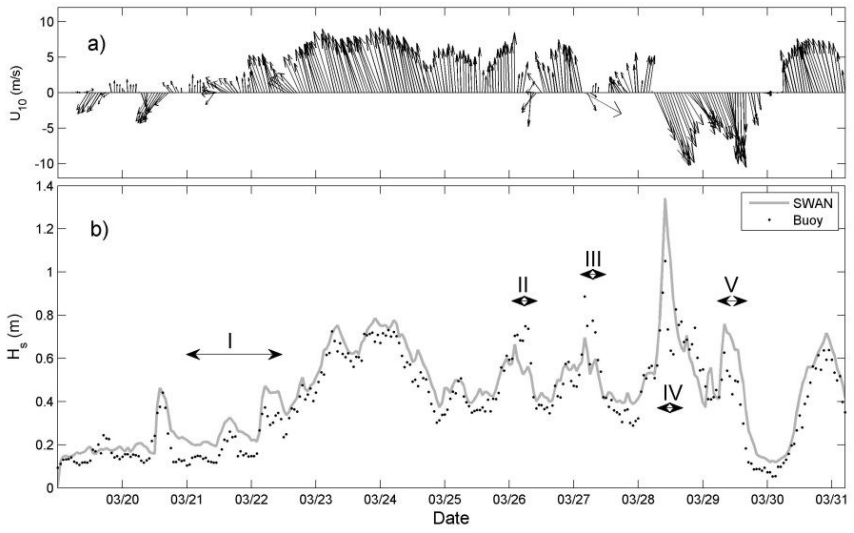

Figure 6.4. a) The hourly wind vectors measured at CSI03; b) the measured and simulated wave height at CSI03. The incidents of discrepancy between model with non-cohesive friction term and *in situ* measurements are identified and labeled in panel (b).

The result of SWAN with the mud-induced dissipation term showed that $X_m = 14$ km resulted in the best performance of model, and viscosity is the main controlling parameter for the wave height measured at CSI03. Sensitivity of the model to mud layer thickness, density, and width of mud layer from the coastline are discussed in section 6.5.1. In Figure 6.5, the swell and sea wave heights from buoy are compared with results of SWAN using the non-cohesive dissipation term as well as the mud-induced damping term with different values for ν_m. As shown in Figures 6.5a and 6.5c, the swell waves at CSI03 are underestimated but weakly affected by viscosity of the mud layer.

Figure 6.5b and 6.5d depict the overestimation of sea waves by using the non-cohesive formulation of SWAN. Moreover, the sea wave height strongly depends on ν_m, and high values of viscosity are more appropriate at the early phase of each event. A high value of viscosity ($\nu_m = 0.8$ m^2/s) was also reported by Kranenburg et al. (2011), when they simulate waves approaching Big Constance Lake, about 50 km west of the present study area. Moreover, compared to the dissipation term for a non-cohesive environment, the mud-induced dissipation term resulted in faster attenuation of sea waves. Field evidence of the higher dissipation rate of short waves in the waning phase of a storm over a muddy bottom as compared to a sandy environment was also reported by Sheremet and Stone (2003).

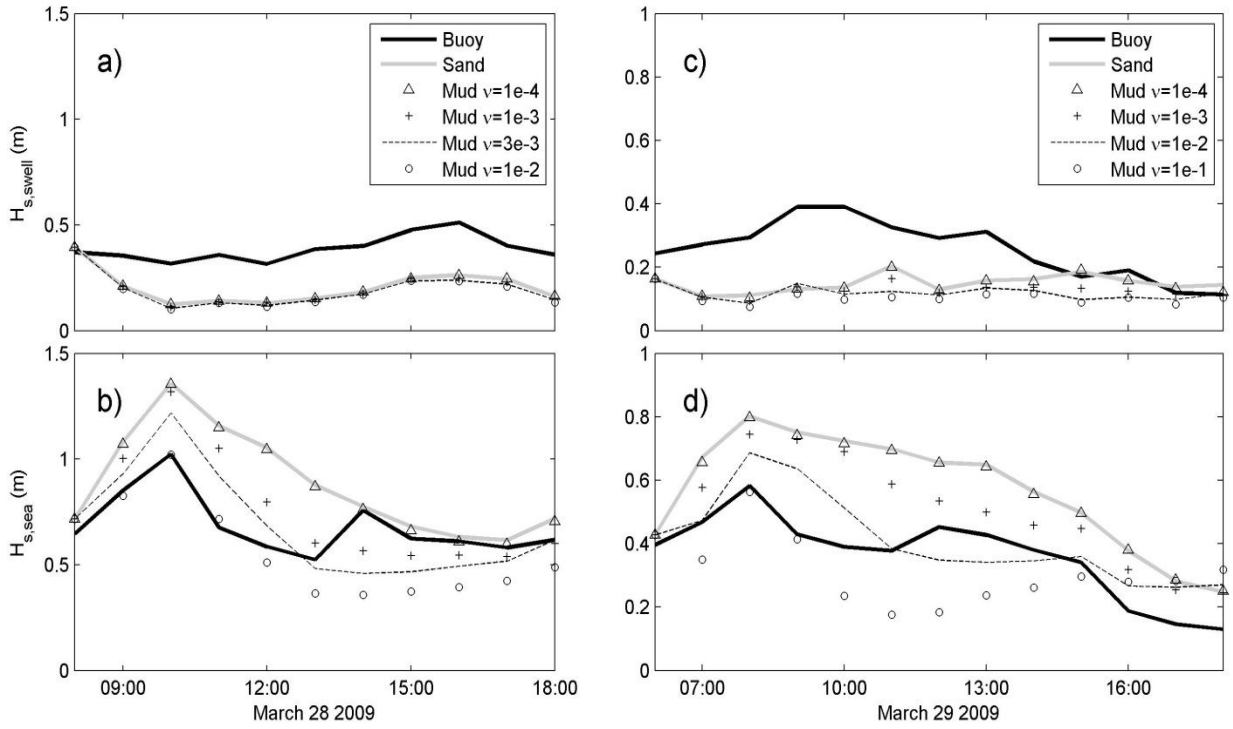

Figure 6.5. a,b) The measured and simulated swell and sea component of wave spectrum on March 28 ; c,d) The same as a,b but for March 29.

Note that increasing either the mud viscosity in the mud-induced wave damping term or roughness height in the non-cohesive bed friction term decreases the wave height. In addition, the mud-induced dissipation term is much more computationally intense than the non-cohesive dissipation term. Therefore, the question might be asked "Could the non-cohesive dissipation term result in the same wave spectra by adjusting the roughness height without using the mud-induced dissipation term?" In order to see whether inclusion of the mud-induced dissipation in SWAN is the same as increasing the roughness length in the formulation by Madsen et al. (1988), SWAN was also run with $K_N = 0.05$ m and $K_N = 0.1$ m.

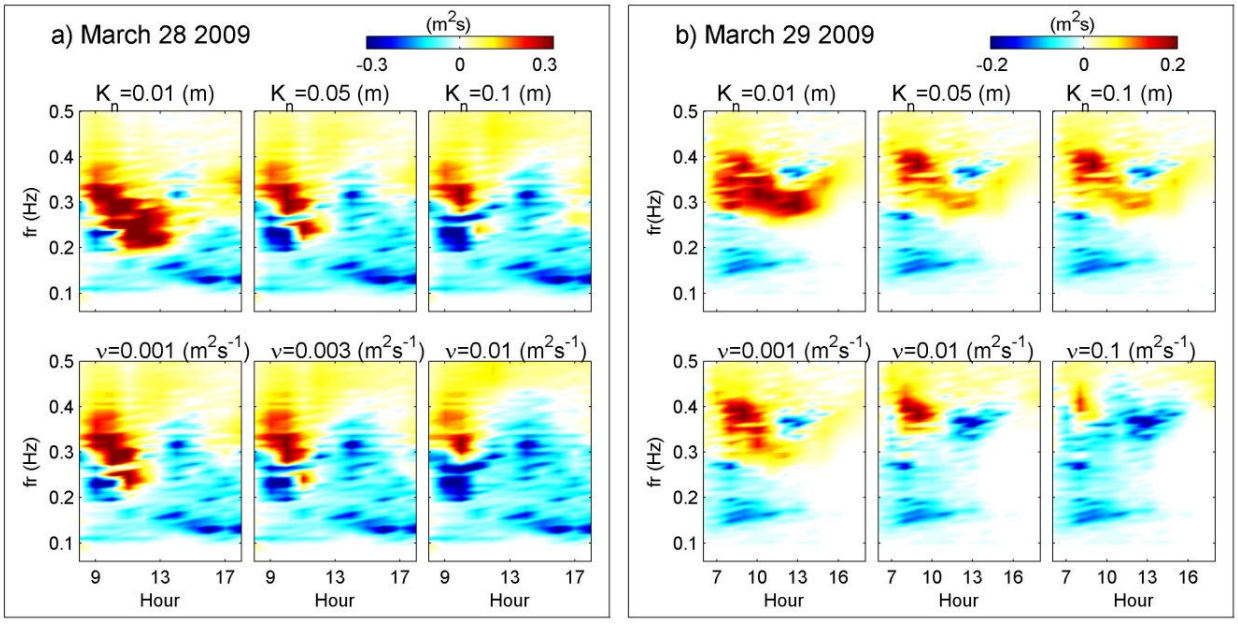

Figure 6.6. a) The bias for spectral evolution at CSI03 station, for SWAN using non-cohesive formulation of bed friction with three values of K_n, when compared against SWAN with mud-dissipation term and having three values for ν_m, on March 28 2009; b) the same as (a) but for March 29 2009.

The biases of spectrum evolution for these simulations are compared in Figure 6.6a for March 28. The effect of increasing K_N from 0.01 to 0.1 m on the bias of spectrum evolution is quite similar to increasing ν_m from 0.001 to 0.01 m^2/s. However, $K_N = 0.1$ m slightly worsen the underestimation of frequency band of 0.1-0.2 Hz after hour 13:00, while its effect on the high frequency band of 0.3-0.4 Hz before hour 13:00 is less than $\nu_m = 0.01$ m^2/s. As shown in Figure 6.6b, the effect of increasing K_N on the bias of spectrum evolution is not the same as increasing ν_m for March 29. Although the increase of K_N from 0.01 m to 0.05 m partially ameliorated the overestimation of energy in the high frequency band of the spectrum, further increase of K_N

from 0.05 m to 0.1 m did not help at all. During this time period, increasing ν_m in the mud-induced dissipation term consistently increases the dissipation in the high frequency end of spectrum with minor changes in low frequency components. Note that the bias of spectrum evolution is close to zero for SWAN with the mud-induced dissipation term using $\nu_m = 0.1$ and 0.001 m^2/s before and after hour 11:00 respectively. Therefore, the result of the wave model with a mud-induced dissipation term is quite different from the model with only a non-cohesive bed friction term.

6.5 Discussions

6.5.1 Sensitivity to the Parameters of Mud Layer

The sea and swell wave heights measured at CSI03 were compared with the simulation result of SWAN with the mud-induced dissipation term using different mud width from coastline in Figure 6.7a,b. For this set of simulations, $\nu_m = 0.001$ m^2/s, $\rho_m = 1300$ kg/m^3 and $h_m = 0.2$ m were assumed. The overestimation of sea waves became worse if $X_m < 14$ km was used while using $X_m > 14$ km did not further ameliorate the overestimation of sea waves. On the other hand, using values of $X_m > 14$ km, there was more dissipation on swell waves, which was not favorable. This process was repeated with different values for viscosity of mud, and the pattern was quite similar. The selection of $X_m = 14$ km was also in agreement with the observation of high concentration of sediment at CSI03 during the passage of a storm reported by Sheremet et al. (2005), and cohesive sediment observed at this station before and after deployments in this study. Note that sediment samples taken from Tiger Shoal were composed of high fraction of shell and shell hash up to 3 km north of TT1 (Stone G.W. et al., 2012). The PC-ADP backscatter intensity at TT1 (not shown here) also suggested a stable bottom during the study period. Therefore, TT1 should be outside of the fluid mud zone, and CSI03 should be inside the fluid mud zone as it is using $X_m = 14$ km.

The sensitivity of sea and swell at CSI03 to the thickness of mud layer assumed in the model is presented in Figure 6.7c,d for $\nu_m = 0.1$ and $\nu_m = 0.001$ m^2/s. It is clear that the difference between model results for three values of $h_m = 0.05$, $h_m = 0.2$ and $h_m = 0.3$ are negligible, and mud thickness is not the primary controlling factor of waves at CSI03. Similarly, Figure 6.7e,f shows that the effect of changing density from 1300 kg/m^3 to 1080 kg/m^3 is negligible for $\nu_m = 0.1$ and $\nu_m = 0.001$ m^2/s. Note that CSI03 is on the southern boundary of the mud layer and its weak sensitivity to the thickness of fluid mud and its density does not imply that these parameters are of secondary importance in the mud-induced dissipation term. In fact, wave height contours of the simulation results (not shown here) suggest that changing the fluid mud characteristics such as its thickness has a profound effect on wave parameters closer to the coast. However, since there was no *in situ* measurement available in the shallower water, it was not possible to evaluate the model outputs north of CSI03.

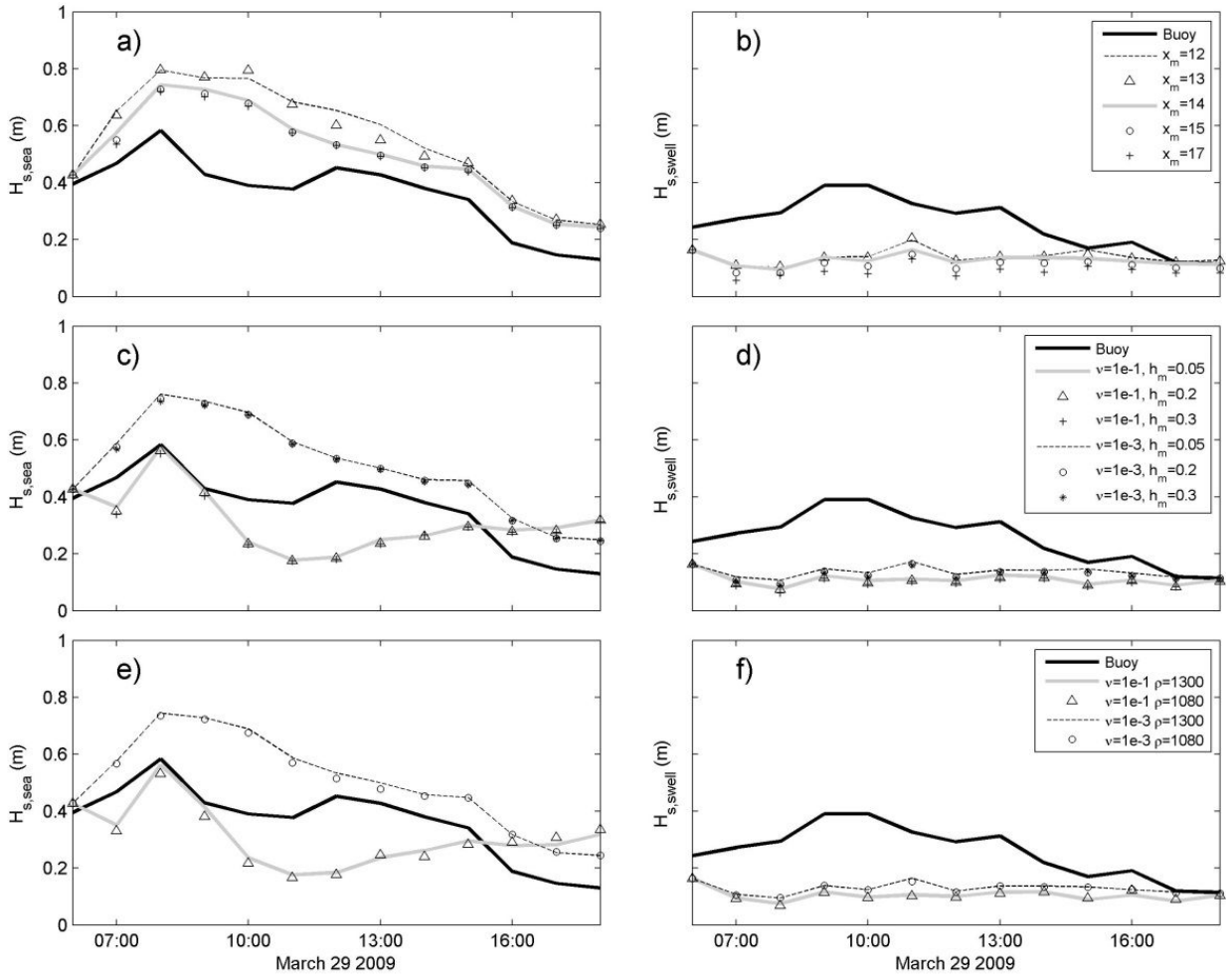

Figure 6.7. Sensitivity of simulated sea and swell waves at CSI03 station to: a,b) X_m (offshore extent of fluid mud). Note that ν_m=0.001 m^2/s and h_m=0.2 m are used for all simulation; c,d) h_m (thickness of fluid mud); e,f) ρ_m (density of fluid mud).

6.5.2 Dissipation of Swell Waves

Figure 6.5a,c shows that the simulated swell waves are overly dissipated in both time periods. The underestimation of swell waves in the presence of sea waves is one of the known problems of the WAM type formulation (van der Westhuysen et al., 2007). The dependence of the whitecapping term of WAM cycle4 formulation on the average wave steepness and wave number results in a decrease in the dissipation of sea waves and an increase in the dissipation of swell waves (Ardhuin et al., 2010). The whitecapping formulation developed by van der Westhuysen et al (2007) could potentially fix this problem. However, employing this formulation accompanied by the wind input formulation of Yan (1987) resulted in local high energy spots in some grid points of the computational domain. During the rapid change of wind direction and speed, a part of the wave energy in the high frequency end of the spectrum in the

earlier wind direction was not being dissipated enough at those grid points. Therefore, those nodes lose their energy too slowly. Decreasing the time step or increasing the spatial resolution, or even replacing the bathymetry with the ideal case having shore parallel contours did not solve this problem. Most likely, the erroneously wide distribution of DIA was fixed by the directionally narrow distribution of the wind energy term of the WAM cycle 4 formulation. Therefore, there was no such problem when the WAM cycle 4 package of SWAN was employed. Due to the high computational cost of the exact formulation of nonlinear wave-wave interaction, it was not possible to test this hypothesis here, and WAM cycle 4 was used for all simulations presented in this study.

6.5.3 Effects of Other Shallow Water Processes

Nonlinear triad wave interaction and wave breaking are two important nearshore processes. The lumped triad approximation method proposed by Eldeberky (1996) to estimate the nonlinear triad interaction is criticized for overestimating the transfer of energy from peak frequency to the second harmonic. It does not consider higher harmonics or the transfer of energy to low frequency harmonics (Booij et al., 2009). The depth-induced breaking formulation of Battjes and Janssen (1978) is also a function of γ, the ratio of wave height to depth; and there is not an agreement on the value of γ in the literature (e.g. see section 5.2 of Svendsen (2006)). Moreover, Winterwerp et al. (2007) showed an aerial photograph in which waves are damped in the presence of fluid mud, and there is no foam or any other visible sign of wave breaking. Therefore the simultaneous use of a depth-induced wave breaking term and a mud-induced wave attenuation term may be questionable. Therefore, the importance of these processes during the study period is evaluated to ensure their minor effects on the conclusions of research presented in this paper.

As shown in Figure 6.8a, the effect of the inclusion of depth-induced wave breaking and the nonlinear triad wave interaction formulation on simulated wave height is insignificant. Moreover, simultaneous inclusion of the triad wave interaction and the mud-induced wave damping term was reported to produce unrealistic results in some wave simulations (Kranenburg et al., 2011). Therefore, all mud simulations in this study were performed without the inclusion of the approximate term for nonlinear triad interactions. Figure 6.8b presents the time series of γ during the study period, which is well below the reported field values such as 0.6 by Thornton and Guza (Thornton and Guza, 1983). The steepness of waves shown in Figure 6.8c is below Miche (1944) which is another criterion for wave breaking. Therefore, Figure 6.8 implies that the uncertainties in the formulations of these shallow water processes do not have any significant impact on the simulation results of this study.

6.5.4 Boundary Conditions

The use of wave spectra from TT1 as a uniform offshore boundary condition at the southern part of the domain introduces an error that could affect the conclusions of this study.

To estimate this error, waves in the Gulf of Mexico were simulated for the time period of this study using the wind data from the North American Regional Re-analyzed database of National Center for Environmental Prediction NCEP/NOAA) server. The wave spectra resulted from the modeling were used to perform two wave simulations with the same setup of SWAN as explained in section 6.3.3. In the first simulation, the non-uniform offshore boundary condition was implemented and in the second one, the wave spectrum at the middle point of the southern boundary was uniformly applied. Results show the wave height variation in the offshore boundary condition (southern boundary shown in Figure 6.2) led to maximum change of less than 7 cm at CSI03 during a weak wind event. Particularly, during March 23-29, the wave height at CSI03 did not vary more than 2 cm (5 % relative change) between these two simulations, suggesting that the boundary effect was not a major source of error.

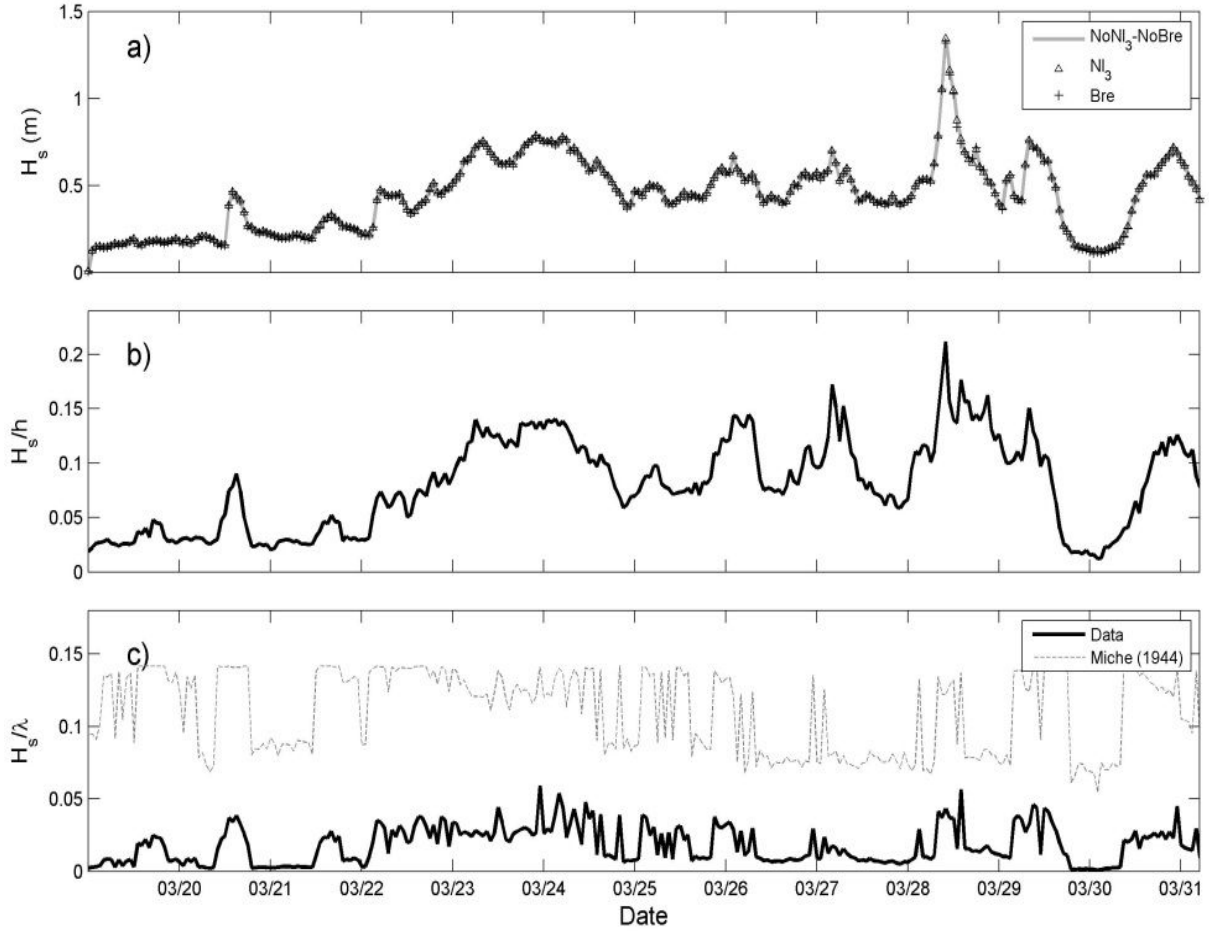

Figure 6.8. Time series of a) wave height resulted from SWAN without triad interaction and depth-induced breaking term (solid line), with triad interaction term (Δ), and with depth induced breaking term (+); b) breaker parameter ϒ; c) wave steepness and its limit from formulation of Miche (1944). All values are measured/calculated for CSI03.

6.5.5 Stationary and Non-Stationary

The time series of simulated wave heights using stationary and non-stationary discretization of equation (6.1) are shown in Figure 6.9. The mud-induced dissipation term was inactive in both of these simulations. Moreover, the curvature-based stopping criterion was used for the stationary simulation, which was more accurate than the default criterion of SWAN (Zijlema and van der Westhuysen, 2005). Following Rogers et al. (2007), each stationary simulation was initialized with a low energy condition to avoid the potential of positive bias. Note that the difference between the two methods increased during northerly wind (see Figure 6.3a), especially on March 29. Considering the overestimation of SWAN with the non-cohesive formulation in the time period labeled as V in Figure 6.3b, it is clear that the stationary assumption potentially worsens the performance of the wave model under a rapidly varying wind field.

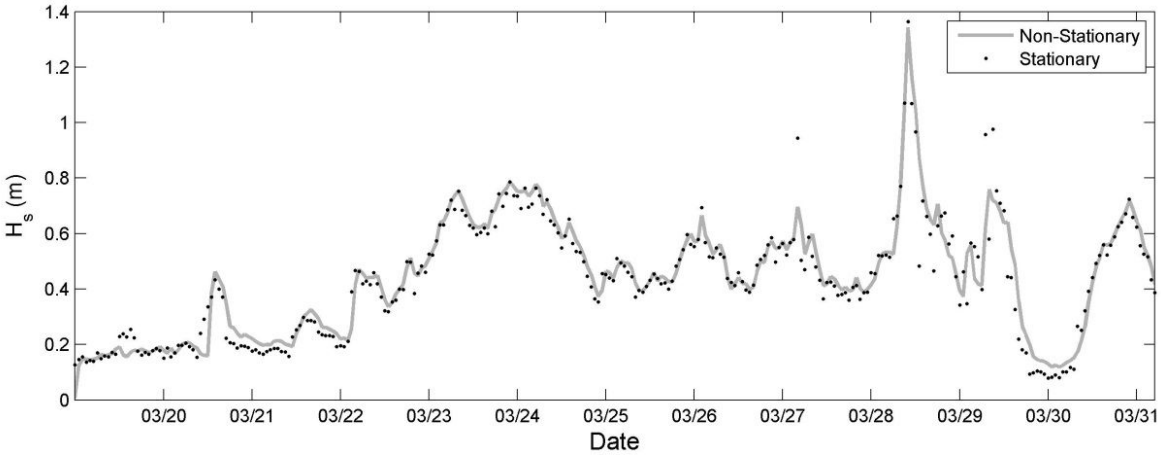

Figure 6.9. Time series of wave height at CSI03 resulted from stationary and non-stationary simulations of waves during the time period of measured data in March 2009.

6.5.6 Wave Height Close to the Coastline

As shown in section 6.5.1, the change in the viscosity of fluid mud within the assumed values of Table 2 significantly affected the wave height at CSI03. In Figure 6.10, the distribution of wave heights at the peak of storm on March 29 2009 is shown for SWAN using the mud-induced dissipation term with $\nu_m = 0.1$ and $\nu_m = 0.001$ m^2/s. Note that wind was from north-west for a couple of hours before this snapshot and the dominant wave direction was from the same direction. The wave growth in shallow water was hindered more when $\nu_m = 0.1$ m^2/s was used for the fluid mud. Therefore, the 0.3 m contour of wave height is closer to the coast when $\nu_m = 0.001$ m^2/s was used. However, as waves propagate offshore, water depth increases and the importance of the fluid mud term decreases. The similarity of the wave height contours

of 0.7 and 1m between two cases confirms that mud-induced dissipation is of secondary importance in a water depth close to 4 m.

The complex dependence of normalized mud-induced energy dissipation of waves, S_{mud} / E, on fluid mud viscosity and wave frequency are demonstrated in Figure 6.11a,b for two water depths. In general, S_{mud} / E increases as viscosity increases for both $h_w = 0.5m$ and $h_w = 4m$. However, for $h_w = 0.5m$, the normalized dissipation is a weak function of wave frequency in the range of 0.03-0.5 Hz when viscosity of fluid mud is less than 0.1 m^2/s. The maximum relative dissipation also occurs close to 0.36 Hz for low viscosity values of fluid mud. However, the frequency of maximum normalized dissipation decreases to approximately 0.12 Hz when ν_m is about 0.2 m^2/s, and again increases for higher viscosity values. In the case of very shallow water with a fluid mud viscosity of $\nu_m = O(1)\ m^2/s$, the mud-induced dissipation term changes sharply over a narrow band of frequencies. In such a situation, this term effectively attenuates the energy transferred from wind to the high frequency band of the spectrum, and delays the process of wave growth.

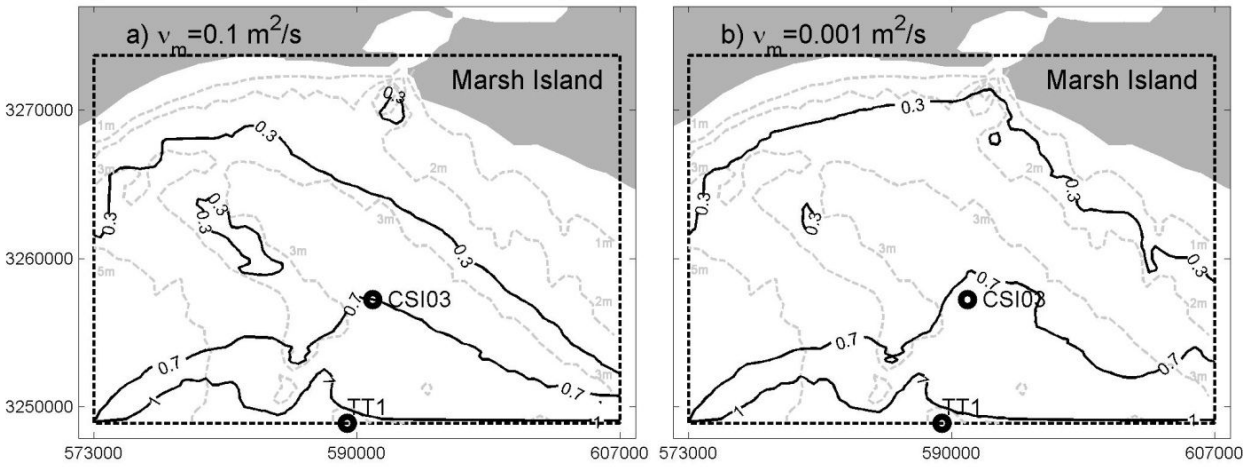

Figure 6.10. The wave height contours of 0.3, 0.7 and 1 m on March 29 2009, at 8:00 GMT are shown in solid black lines for a) ν_m=0.1 m^2/s; b) ν_m=0.001 m^2/s. The gray dash contours are isobaths.

As expected, the importance of mud-induced dissipation decreases as water depth increases. Therefore, the values of S_{mud} / E are much smaller in Figure 6.11b than Figure 6.11a. Note that dissipation is not a weak function of wave frequency. Moreover, the maximum of relative dissipation is in the low frequency end of the spectrum, close to 0.13 Hz, exposing relatively weak dissipation on short waves. Note that nonlinear triad interactions, however, can transfer high frequency energy to the low frequency band that is efficiently dissipated by the

fluid mud, as demonstrated by Elgar and Raubenheimer (2008), which is not accounted for by SWAN.

6.5.7 Comparison with Ng Implementation

As mentioned in section 6.3.1, Ng (2000) proposed explicit formulations for the imaginary part of the wave number, and the wave attenuation rate in the case of a thin layer of mud. Avoiding the complex iteration schemes needed to find the roots of the dispersion equation, and the numerical errors involved therein may attract the use of the Ng (2000) approximation in wave simulations. However, this formulation is only valid when the mud layer is thin. Increasing the viscosity increases the Stokes boundary layer thickness, $\delta = \sqrt{2\nu_m/\sigma}$, and may violate the assumption of $k\delta << 1$ needed in the derivation of the explicit formulae. In this section, the wave dissipation of Ng (2000) is compared to the more advanced formulation of Kranenburg et al. (2011).

Figure 6.11c,d shows the approximation of S_{mud} / E predicted by the Ng (2000) formulation for similar conditions as Figure 6.11a,b. For $h_m = 0.2m$ assumed in these calculations, the approximation of Ng (2000) is not valid for $\nu_m > 0.001$ m^2/s and underestimates the mud-induced energy dissipation by several orders of magnitude. Therefore, the Ng (2000) formulation cannot be used for simulation of wave damping close to the coast near the Atchafalaya Bay. Although not shown here, decreasing the h_m to 0.05 in Figure 6.11, increases the importance of normalized mud-induced dissipation and consequently, the discrepancies between formulations of Ng (2000) and Kranenburg et al. (2011).

6.6 Conclusions of Chapter 6

The algorithm presented by Kranenburg et al. (2011) to incorporate the mud-induced dissipation of wave energy was optimized by reformatting the dispersion equation and changing the initial value used for iterations. These modifications reduced the computational efforts needed for each time step considerably, and made it possible to use SWAN for simulation of wave growth over the inner shelf opposite Atchafalaya Bay using a non-stationary formulation of wave action balance. During northerly wind of a cold front recorded in the deployment period, the interaction of high frequency wind seas and fluid mud resulted in lower wave heights than simulated by SWAN without the mud-induced energy dissipation term.

The directional separation of wave height into sea and swell was performed to account for underestimation of the swell waves due to whitecapping term. This method is also not sensitive to the inaccuracies in reproducing spectral shape by the wave model resulted from other sink and source terms. Mud coverage, kinematic viscosity, thickness, and density were determined by sensitivity analysis on sea and swell wave height from one station in the southern boundary of fluid mud zone. Within the range of parameters reported in the literature, viscosity was found to be important. The best performance of the model during the peak of the storm

happened when high values of viscosity (0.1-1 m^2/s) were used. However, lower values (0.01-0.001 m^2/s) were better for few hours after the peak of wave height.

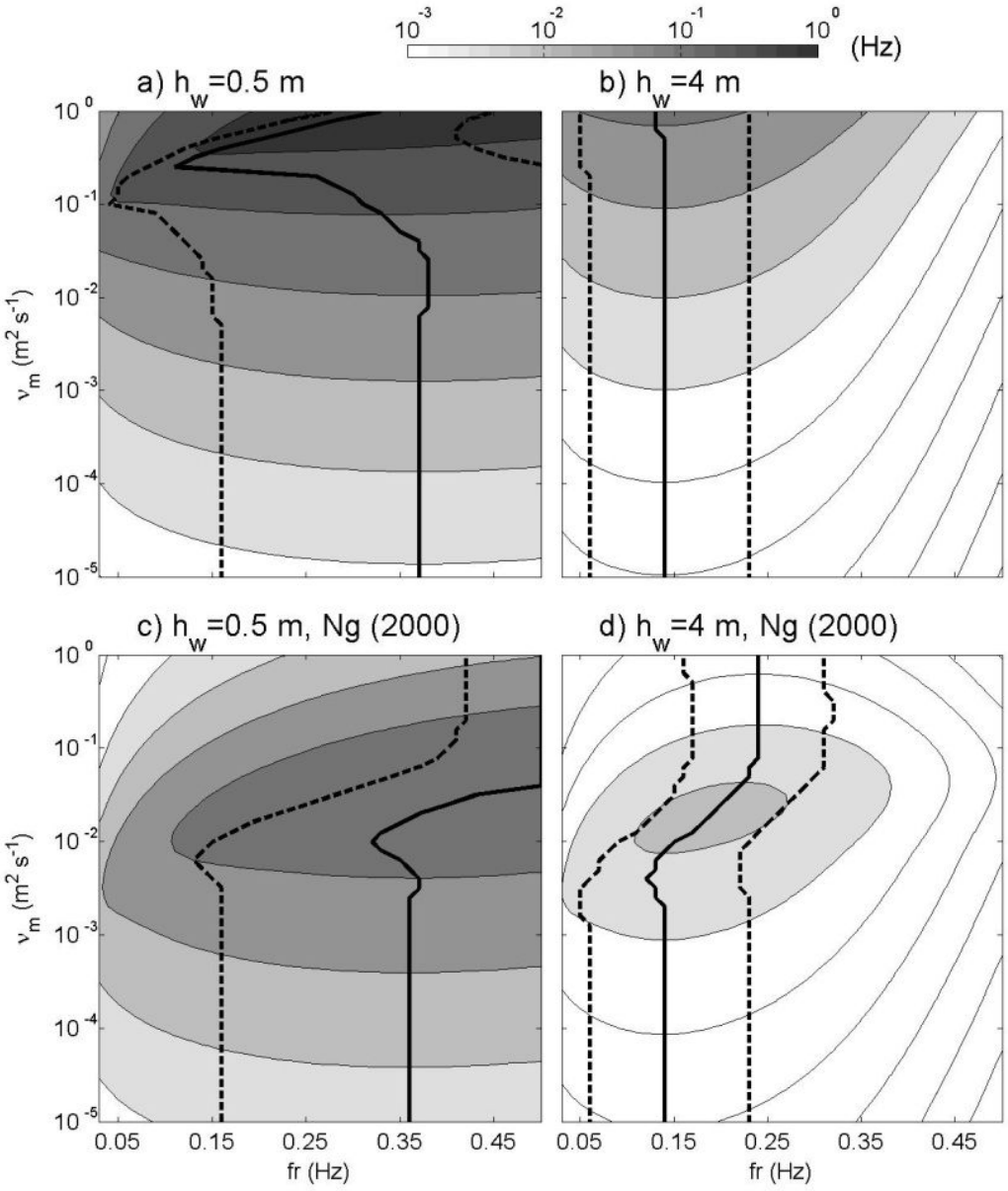

Figure 11. Variation of the normalized mud-induced dissipation term, S_{mud}/E versus wave frequency (fr) and kinematic viscosity (ν_m) according to a) Kranenburg et al. (2011) and h_w=0.5 m; b) Kranenburg et al. (2011) and h_w=4 m; c) NG (2000) and h_w=0.5 m, d) NG (2000) and h_w=4 m. The values of h_m=0.2 m, ρ_m=1300 kg/m^3 and ρ_m=1025 kg/m^3 are used for all panels. The solid black line represents the frequency of maximum S_{mud}/E as a function of ν_m. For specific value of ν_m, dashed lines mark the frequencies that S_{mud}/E decreases to 80% of the peak.

In very shallow water close to the shoreline such as h_w=0.5 m, the mud-induced dissipation term strongly dissipated the energy in the high frequency end of spectrum when kinematic viscosity was of the order of 1 m^2/s. However the dissipation broadened in the frequency domain as the viscosity decreased to 0.1 and the peak of dissipation shifted to the low frequency range of the spectrum. The frequency of maximum relative dissipation returned to the high frequency end of the spectrum for $\nu_m < 0.01$ m^2/s and the dissipation term became a weak function of frequency. In deeper water, such as h_w=4 m, the mud-induced dissipation term was a strong function of frequency and attenuated the energy mainly from a narrow band at low frequency end of the spectrum regardless of fluid mud viscosity (in the range of 10^{-5}-1 m^2/s).

It was also shown that the explicit formulation of Ng (2000) could not reproduce above-mentioned behavior of the energy dissipation when the kinematic viscosity exceeded 0.001 m^2/s. Effort was also made to reproduce the same simulation results with the non-cohesive bed friction formulation of SWAN. However, the use of the energy dissipation formulation of Madsen et al. (1988), even with artificially high values of roughness height, could not provide enough dissipation on high frequency waves.

CHAPTER 7: SYNTHESIS AND CONCLUSIONS

As described in previous chapters, the phase averaged wave models were employed to simulate the waves in the Gulf of Mexico and along the Louisiana coast. Two wave models, WAVEWATCH-III and SWAN, were skill assessed in idealized cases, and also during the passages of several cold fronts and hurricanes. Research results allowed for the following conclusions:

7.1 Calibration of Whitecapping Term

The whitecapping term of the WAM-3 formulation was originally calibrated so that it can reproduce the parametric wave spectra such as the spectrum of Pierson and Moskowitz (1964), proposed for fully developed conditions. Several alternatives of two widely used formulations of white capping, WAM-3 and WAM-4 were calibrated using *in situ* measurements from NDBC buoys and WAVCIS stations from the Gulf of Mexico. This calibration process resulted in significant improvement in the performance of the model in the Gulf of Mexico.

The alternative formulations of WAM-3 and WAM-4 were considered by assuming higher dependence of wave dissipation on the wave number and the wave steepness relative to the original formulations. Although all configurations resulted in a similar level of accuracy for wave height, the performance of SWAN with each configuration was different in simulating wave period and idealized wave growth.

Increasing the power of the steepness term in the WAM-3 formulation from 2 to 3 slightly decreased the Scatter Index of wave height and also improved the resulting bias for small H_s and short T_p. It also outperformed the original WAM-3 formulation in reproducing fetch-limited growth curves as well as the saturation level for the wave spectrum.

Increasing the power of wave number component in the whitecapping formulation of the WAM-3 partially ameliorated the underestimation of average wave period. The direct dissipation of energy in the high frequency end of the wave spectrum, and indirect effects of changing the mean wave number contributed to this improvement. However, during strong and steady wind, the spurious energy transfer to the low frequency portion of the wave spectrum could result in a bimodal wave spectrum. Incorporation of a higher order wave number term in WAM-4 also resulted in the model being prone to developing a bimodal energy spectrum.

A similar level of accuracy for wave height was achieved by using WAM-4 alternatives. However, the average wave period was predicted better by the WAM-4 alternatives than original WAM-3 and its alternatives.

7.2 Slope of High Frequency Tail and Cut-off Frequency

As explained in Chapter 3, the high cut-off frequency in the model determines the maximum modal frequency for which model numerically solves the wave balance equation. Because the model requires the energy content at frequencies larger than maximum model

frequency, a power law with the slope of n is assumed beyond the high cut-off frequency for wave spectrum.

The WAM-3 formulation was very sensitive to the assumed high cut-off frequency and assumed power law for the diagnostic frequency tail. Although SWAN assumes n=4 when the WAM-3 formulation was used, the use of n=5 was shown to be more successful for reproducing the bulk wave parameters in oceanic scales, especially during low energy events. Moreover, use of the WAM-3 formulation transferred too much energy beyond the equilibrium range of the spectrum. Therefore, use of cut-off frequency close to 0.5 Hz was suggested rather than the default value of 1 Hz. The repetition of the same simulations using WAVEWATCH-III confirmed that the numerical scheme was not responsible for high energy content at frequency band of 0.5-1 Hz.

The higher dissipation imposed on the high frequency end of the spectrum when the WAM-4 or Westhuysen formulations were employed led to low energy content in the high frequency end of the spectrum. Therefore, these formulations were not sensitive to the exponent used for the tail form or the assumed cut-off frequency. This feature can be used to decrease the time needed to perform a simulation by choosing the cutoff frequency close to 0.5 Hz instead of 1 Hz.

7.3 Use of Sediment Characteristics in Bed Friction Term

Chapter 4 was concerned with comparing two bed friction formulations: a simple formulation of JONSWAP, and the eddy-viscosity model presented by Madsen et al. (1988). Inclusion of the latter one increased the total computational time by approximately 4%, and required roughness height of the bed. The limited comparisons of the model results with *in situ* observations suggested a better performance of the formulation of Madsen et al. (1988) when roughness height was estimated based on the grain size of seabed sediments. Therefore, this formulation was used in later chapters to include the bottom friction effects in the model.

During severe storms and hurricanes, such as Hurricane Dennis 2005, the difference between JONSWAP and Madsen et al. (1988) formulations could exceed 1.5 m or 40% of local wave height. During the passage of Hurricane Dennis, the spatial extension of the difference between two formulations could exceed beyond the 30 m isobath. However, during fair-weather and storm conditions, the difference between using these two formulations became largely confined to landward of the 15m isobath.

7.4 Inclusion of Mud-induced Attenuation of Wave Energy

The algorithm presented by Kranenburg et al. (2011) to solve the complex dispersion equation was modified to reduce the computational efforts required to find the complex wave numbers. The SWAN with and without mud-induced damping term was used to simulate the wave growth over the inner shelf opposite Atchafalaya Bay. Compared to *in situ* observations, high frequency wind seas were significantly overestimated by SWAN without mud-induced

energy dissipation term. Increasing the roughness height in the non-cohesive bed friction term resulted in too much dissipation in low frequency waves and only slightly decreased of overestimation in short waves. Therefore, another mechanism was required to damp the high frequency waves over the Atchafalaya shelf during northerly wind.

Using the directional partitioning of sea and swell waves, the underestimation of swell waves were separated from overestimation of wind seas. The mud layer density, thickness, density and its spatial extent were determined by sensitivity analysis on sea and swell waves. The model results indicated the high value of fluid mud viscosity (0.1-1 m^2/s) during the peak of the storm. However, a few hours after the passage of the peak waves, the lower value of mud viscosity (0.01-0.001 m^2/s) resulted in better agreement with observations.

In a water depth of 0.5 m, the normalized mud-induced damping term strongly dissipated the energy on high frequency end of spectrum when kinematic viscosity was of the order of 1 m^2/s. However, the dissipation was not a narrow function of frequency for mud viscosity smaller than 0.1. Due to dissipation of high frequency waves in shallow water close to the coastline, the mud-induced damping decreased the effective fetch of the wind, and hindered the wave growth. Note that increasing the water depth decreased the importance of the mud-induced damping term. In deeper water such as h_w=4 m, the mud dissipation term was a strong function of frequency, and mainly attenuated a narrow band of low frequencies close to 0.13 Hz regardless of fluid mud viscosity (in the range of 10^{-5}-1 m^2/s).

7.5 Directions for Future Research

In Chapter 2, it was shown that the use of a wind input formulation from the WAM-4 package in SWAN in conjunction with WAM-3 white capping term was the most successful combination in hindcasting the peak period in the Gulf of Mexico. This combination also outperforms all WAM-3 alternatives in the estimation of average wave period. The use of the WAM-3 formulation of SWAN with the highly dynamic wind condition presented in Chapter 6 was not successful and resulted in numerical instabilities. Indications are evident that the wind input formulation also plays an important role in the performance of wave models, and part of their below par performance can be resolved by modifying the wind input term instead of the white capping term. The WAM-4 wind input formulation is 10 times more computationally expensive than WAM-3 wind input formulation and results in approximately a 30% extension in total computational time. However, it enhances the overall performance of the model. The in-depth analysis of the available wind input term and evaluating their alternatives is worthy of notice for future research.

As shown in Chapter 3, the use of WAVEWATCH-III with the wind input and white capping dissipation terms proposed by Tolman and Chalikov, (1996) resulted in considerable overestimation of energy dissipation for the Gulf of Mexico. Therefore, a new calibration process is needed to remedy the underestimation of wave energy in low frequency end of the spectrum simulated by this package.

Comparing the WAVEWATCH-III performance using the WAM-3 formulation and a dynamic high cut-off frequency with a static cut-off frequency showed that the dynamic cut-off frequency resulted in better hindcast results with less computational cost. Therefore, in order to efficiently use SWAN at oceanic scales, the implementation of a dynamic cut-off frequency in the source code is required.

As explained in Chapter 6, the numerical algorithm to solve the complex dispersion equation in the presence of a mud layer was improved in this study. However, the mud-induced wave attenuation term is still one of the most time consuming parts of the source code. The available explicit formulations for the imaginary part of the complex wavenumber have been proposed for special cases, and cannot be used in a general shallow water wave model. Proposing an explicit approximation formulation for the roots of the dispersion equation presented in Chapter 6 and optimizing the model calculations are the potential future research areas to improve the model performance. Moreover, the performance of the model was evaluated only close to the offshore boundary of the mud zone. Using a series of pressure sensors inside the mud zone can provide further details about the dynamical interaction of fluid mud and waves, and the performance of the formulations used in this study.

Nonlinear quadratic and triad wave interactions are also among the source and sink terms which need to be optimized for the Gulf of Mexico. The approximate method used for nonlinear quadratic wave interaction has been shown to be responsible for several problems in the third generation wave models. The implementation of other approximate methods such as the reduced integration approach (Lin and Perrie, 1999) or the multiple representative quadruplets (Hashimoto and Kawaguchi, 2001; Resio and Perrie, 2008; van Vledder GP., 2001) can potentially improve the performance of the wave model. Triad wave-wave interaction is also an important process in shallow water which transfers energy to higher and lower frequencies. The method implemented in the official release of SWAN is based on a relatively old Boussinesq equation, and sacrifices the accuracy for efficiency by ignoring higher order terms. The use of a more recent Boussinesq equation for deriving the nonlinear term, or the more accurate formulations such as the one presented recently by Booij et al. (2009) may improve the model performance and needs to be validated.

REFERENCES

Allison, M.A., Kineke, G.C., Gordon, E.S. and Goni, M.A., 2000. Development and Reworking of a Seasonal Flood Deposit on the Inner Continental Shelf off the Atchafalaya River. Cont Shelf Res, 20(16): 2267-2294.

Alves, J.H.G.M., Greensladeb, D.J.M. and Banner, M.L., 2002. Impact of a Saturation-Dependent Dissipation Source Function on Operational Hindcasts of Wind-Waves in the Australian Region Journal of Atmospheric & Ocean Science, 8(4): 239-267.

Anctil, F., Donelan, M.A., Forristall, G.Z., Steele, K.E. and Ouellet, Y., 1993. Deep-Water Field-Evaluation of the Ndbc-Swade 3-M Discus Directional Buoy. J Atmos Ocean Tech, 10(1): 97-112.

Ardhuin, F. et al., 2007. Swell and Slanting-Fetch Effects on Wind Wave Growth. J Phys Oceanogr, 37(4): 908-931.

Ardhuin, F. et al., 2010. Semiempirical Dissipation Source Functions for Ocean Waves. Part I: Definition, Calibration, and Validation. J Phys Oceanogr, 40(9): 1917-1941.

Babanin, A.V., Tsagareli, K.N., Young, I.R. and Walker, D.J., 2010. Numerical Investigation of Spectral Evolution of Wind Waves. Part II: Dissipation Term and Evolution Tests. J Phys Oceanogr, 40(4): 667-683.

Baker, E.T. and Lavelle, J.W., 1984. The Effect of Particle-Size on the Light Attenuation Coefficient of Natural Suspensions. J Geophys Res-Oceans, 89(Nc5): 8197-8203.

Banner, M.L., 1990. Equilibrium Spectra of Wind-Waves. J Phys Oceanogr, 20(7): 966-984.

Banner, M.L., 1991. On the Directional Behavior of the Equilibrium Wave Number Spectrum: Implications for the Equilibrium Frequency Spectrum. In: R.C. Beal (Editor), Directional Ocean Wave Spectra. Johns Hopkins University Press, Baltimore, pp. 39-45.

Banner, M.L., Jones, I.S.F. and Trinder, J.C., 1989. Wavenumber Spectra of Short Gravity-Waves. J Fluid Mech, 198: 321-344.

Banner, M.L. and Young, I.R., 1994. Modeling Spectral Dissipation in the Evolution of Wind-Waves .1. Assessment of Existing Model Performance. J Phys Oceanogr, 24(7): 1550-1571.

Battjes, J.A. and Janssen, J.P.F.M., 1978. Energy Loss and Set-up Due to Breaking of Random Waves. 16th International Conference on Coastal Engineering, ASCE, pp. 569-587.

Berg, R., 2008. Tropical Cyclone Report Hurricane Ike, National Hurricane Centre, National Oceanographic and Atmospheric Administration, Miami, Florida.

Beven, J.L., 2006. Tropical Cyclone Report on Hurricane Dennis National Hurricane Center.

Beven, J.L. and Kimberlain, T.B., 2008. Tropical Cyclone Report Hurricane Gustav, National Hurricane Centre, National Oceanographic and Atmospheric Administration, Miami, Florida.

Bilgili, A., Smith, K.W. and Lynch, D.R., 2006. BatTri: A Two-Dimensional Bathymetry-Based Unstructured Triangular Grid Generator for Finite Element Circulation Modeling. Comput Geosci-Uk, 32(5): 632-642.

Booij, N., Holthuijsen, L.H. and Benit, M., 2009. A Distributed Collinear Triad Approximation in SWAN, Coastal Dynamics, Tokyo, Japan, pp. 10.

Booij, N., Ris, R.C. and Holthuijsen, L.H., 1999. A Third-Generation Wave Model for Coastal Regions - 1. Model Description and Validation. J Geophys Res-Oceans, 104(C4): 7649-7666.

Bouws, E. and Komen, G.J., 1983. On the Balance between Growth and Dissipation in an Extreme Depth-Limited Wind-Sea in the Southern North-Sea. J Phys Oceanogr, 13(9): 1653-1658.

Breugem, W.A. and Holthuijsen, L.H., 2007. Generalized Shallow Water Wave Growth from Lake George. J Waterw Port C-Asce, 133(3): 173-182.

Buczkowski, B.J. et al., 2006. usSEABED: Gulf of Mexico and Caribbean (Puerto Rico and U.S. Virgin Islands) Offshore Surficial Sediment Data Release: U.S. Geological Survey Data Series 146, version 1.0.

Burden R.L and Faires, J.D., 2001. Numerical Analysis. Brooks Cole, Pacific Grove, CA., 864 pp.

Cavaleri, L. et al., 2007. Wave Modelling - The State of the Art. Prog Oceanogr, 75(4): 603-674.

Cavaleri, L. and Rizzoli, P.M., 1981. Wind Wave Prediction in Shallow-Water - Theory and Applications. J Geophys Res-Oc Atm, 86(Nc11): 961-973.

Chalikov, D., 1995. The Parameterization of the Wave Boundary-Layer. J Phys Oceanogr, 25(6): 1333-1349.

Chalikov, D.V. and Belevich, M.Y., 1993. One-Dimensional Theory of the Wave Boundary-Layer. Bound-Lay Meteorol, 63(1-2): 65-96.

Cochrane, J.D. and Kelly, F.J., 1986. Low-Frequency Circulation on the Texas-Louisiana Continental-Shelf. J Geophys Res-Oceans, 91(C9): 645-659.

Cuchiara, D.C., Fernandes, E.H., Strauch, J.C., Winterwerp, J.C. and Calliari, L.J., 2009. Determination of the Wave Climate for the Southern Brazilian Shelf. Cont Shelf Res, 29(3): 545-555.

Dalrymple, R. and Liu, P.L., 1978. Waves over Soft Mud Beds: A Two-Layer Fluid Mud Model. J Phys Oceanogr, 8: 1121-1131.

De Wit, P.J., 1995. Liquefaction of Cohesive Sediments Caused by Waves, Delft University of Technology, Delft 194 pp.

Defendi, V., Kovacevic, V., Arena, F. and Zaggia, L., 2010. Estimating Sediment Transport from Acoustic Measurements in the Venice Lagoon Inlets. Cont Shelf Res, 30(8): 883-893.

Deines, K.L., 1999. Backscatter Estimation Using Broadband Acoustic Doppler Current Profilers. IEEE Sixth Working Conference on Current Measurement, pp. 249 - 253.

Donelan, M.A., Hamilton, J. and Hui, W.H., 1985. Directional Spectra of Wind-Generated Waves. Philos T Roy Soc A, 315(1534): 509-562.

Downing, A., Thorne, P.D. and Vincent, C.E., 1995. Backscattering from a Suspension in the near-Field of a Piston Transducer. J Acoust Soc Am, 97(3): 1614-1620.

Downing, J., 2006. Twenty-Five Years with OBS Sensors: The Good, the Bad, and the Ugly. Cont Shelf Res, 26(17-18): 2299-2318.

Downing, J.P. and Beach, R.A., 1989. Laboratory Apparatus for Calibrating Optical Suspended-Solids Sensors. Mar Geol, 86(2-3): 243-249.

Eldeberky, Y., 1996. Nonlinear Transformations of Wave Spectra in the Nearshore Zone, elft University of Technology, The Netherlands, 203 pp.

Elgar, S. and Raubenheimer, B., 2008. Wave Dissipation by Muddy Seafloors. Geophys Res Lett, 35(7).

Ewans, K.C. and Kibblewhite, A.C., 1990. An Examination of Fetch-Limited Wave Growth Off the West-Coast of New-Zealand by a Comparison with the JONSWAP Results. J Phys Oceanogr, 20(9): 1278-1296.

Feng, Z.X. and Li, C.Y., 2010. Cold-Front-Induced Flushing of the Louisiana Bays. J Marine Syst, 82(4): 252-264.

Forristall, G.Z., 1981. Measurements of a Saturated Range in Ocean Wave Spectra. J Geophys Res-Oc Atm, 86(Nc9): 8075-8084.

Francois, R.E. and Garrison, G.R., 1982. Sound-Absorption Based on Ocean Measurements .2. Boric-Acid Contribution and Equation for Total Absorption. J Acoust Soc Am, 72(6): 1879-1890.

Fugate, D.C. and Friedrichs, C.T., 2002. Determining Concentration and Fall Velocity of Estuarine Particle Populations Using ADV, OBS and LISST. Cont Shelf Res, 22(11-13): 1867-1886.

Gade, H.G., 1958. Effects of a Nonrigid, Impermeable Bottom on Plane Surface Waves in Shallow Water. J Mar Res, 16(2): 61-82.

Gartner, J.W., 2004. Estimating Suspended Solids Concentrations from Backscatter Intensity Measured by Acoustic Doppler Current Profiler in San Francisco Bay, California. Mar Geol, 211(3-4): 169-187.

Georgiou, I.Y. and Schindler, J.K., 2009. Wave Forecasting and Longshore Sediment Transport Gradients Along a Transgressive Barrier Island: Chandeleur Islands, Louisiana. Geo-Mar Lett, 29(6): 467-476.

Graber, H.C. and Madsen, O.S., 1988. A Finite-Depth Wind-Wave Model .1. Model Description. J Phys Oceanogr, 18(11): 1465-1483.

Grenci, L.M. and Nese, J.M., 2006. A World of Weather: Fundamental of Meteorology. Kendall/Hunt Publishing Company.

Guo, J.K., 2002. Simple and Explicit Solution of Wave Dispersion Equation. Coast Eng, 45(2): 71-74.

Ha, H.K., Hsu, W.Y., Maa, J.P.Y., Shao, Y.Y. and Holland, C.W., 2009. Using ADV Backscatter Strength for Measuring Suspended Cohesive Sediment Concentration. Cont Shelf Res, 29(10): 1310-1316.

Ha, H.K., Maa, J.P.Y., Park, K. and Kim, Y.H., 2011. Estimation of High-Resolution Sediment Concentration Profiles in Bottom Boundary Layer Using Pulse-Coherent Acoustic Doppler Current Profilers. Mar Geol, 279(1-4): 199-209.

Hageman, L.A. and Young, D.M., 2004. Applied Iterative Methods. Dover Publications.

Hagen, S.C., Horstman, O. and Bennett, R.J., 2002. An Unstructured Mesh Generation Algorithm for Shallow Water Modeling. Int J Comput Fluid D, 16(2): 83-91.

Hansen, C., Katsaros, K.B., Kitaigorodskii, S.A. and Larsen, S.E., 1990. The Dissipation Range of Wind-Wave Spectra Observed on a Lake. J Phys Oceanogr, 20(9): 1264-1277.

Hanson, J.L. and Phillips, O.M., 1999. Wind Sea Growth and Dissipation in the Open Ocean. J Phys Oceanogr, 29(8): 1633-1648.

Hanson, J.L. and Phillips, O.M., 2001. Automated Analysis of Ocean Surface Directional Wave Spectra. J Atmos Ocean Tech, 18(2): 277-293.

Hanson, J.L., Tracy, B.A., Tolman, H.L. and Scott, R.D., 2009. Pacific Hindcast Performance of Three Numerical Wave Models. J Atmos Ocean Tech, 26(8): 1614-1633.

Hashimoto, N., 1997. Analysis of the Directional Wave Spectrum from Field Data. In: P.L.-F. Liu (Editor), Advances in coastal and ocean engineering. World Scientific, Singapore, pp. 103–143.

Hashimoto, N. and Kawaguchi, K., 2001. Extension and Modification of Discrete Interaction Approximation (DIA) for Computing Nonlinear Energy Transfer of Gravity Wave Spectrum. In: Ocean Wave Measurement and Analysis. Ocean Wave Measurement and Analysis, San Francisco, pp. 530-539.

Hasselmann, K., 1963. On the Non-Linear Energy Transfer in a Gravity-Wave Spectrum .3. Evaluation of the Energy Flux and Swell-Sea Interaction for a Neumann Spectrum. J Fluid Mech, 15(3): 385-398.

Hasselmann, K., 1974. On the Spectral Dissipation of Ocean Waves Due to Whitecapping. Bound-Lay Meteorol, 6(1-2): 107-127.

Hasselmann, K., 1988. The Wam Model - a 3rd Generation Ocean Wave Prediction Model. J Phys Oceanogr, 18(12): 1775-1810.

Hasselmann, K. et al., 1973. Measurements of Wind-Wave Growth and Swell Decay During the Joint North Sea Wave Project (JONSWAP), Deutsche Hydrogr. Z. A8, No 12.

Hasselmann, S. and Hasselmann, K., 1985. Computations and Parameterizations of the Nonlinear Energy-Transfer in a Gravity-Wave Spectrum .1. A New Method for Efficient Computations of the Exact Nonlinear Transfer Integral. J Phys Oceanogr, 15(11): 1369-1377.

Hasselmann, S., Hasselmann, K., Allender, J.H. and Barnett, T.P., 1985. Computations and Parameterizations of the Nonlinear Energy-Transfer in a Gravity-Wave Spectrum .2. Parameterizations of the Nonlinear Energy-Transfer for Application in Wave Models. J Phys Oceanogr, 15(11): 1378-1391.

Hoitink, A.J.F. and Hoekstra, P., 2005. Observations of Suspended Sediment from ADCP and OBS Measurements in a Mud-Dominated Environment. Coast Eng, 52(2): 103-118.

Hsu, S.A., 1988. Coastal Meteorology. Academic Press, San Diego, 260 pp.

Hwang, P.A., Atakturk, S., Sletten, M.A. and Trizna, D.B., 1996. A Study of the Wavenumber Spectra of Short Water Waves in the Ocean. J Phys Oceanogr, 26(7): 1266-1285.

Janssen, P.A.E.M., 1989. Wave-Induced Stress and the Drag of Air-Flow over Sea Waves. J Phys Oceanogr, 19(6): 745-754.

Janssen, P.A.E.M., 1991. Quasi-Linear Theory of Wind-Wave Generation Applied to Wave Forecasting. J Phys Oceanogr, 21(11): 1631-1642.

Janssen, P.A.E.M., 2004. The Interaction of Ocean Waves and Wind. Cambridge University Press, 300 pp.

Janssen, P.A.E.M., 2008. Progress in Ocean Wave Forecasting. J Comput Phys, 227(7): 3572-3594.

Janssen, P.A.E.M., 1994. Simple Tests. In: G.J. Komen et al. (Editors), Dynamics and Modelling of Ocean Waves. Cambridge University Press, pp. 556.

Jaramillo, S., Sheremet, A., Allison, M.A., Reed, A.H. and Holland, K.T., 2009. Wave-Mud Interactions Over the Muddy Atchafalaya Subaqueous Clinoform, Louisiana, United States: Wave-Supported Sediment Transport. J Geophys Res-Oceans, 114.

Johnson, D., 2008. DIrectional WAve SPectra Toolbox, Version 1.3.1, MetOcean Solutions Ltd

Jonsson, I.G., 1967. Wave Boundary Layers and Friction Factors. Tenth Conference on Coastal Engineering, Tokyo, Japan, pp. 127-148.

Jonsson, I.G., 1980. New Approach to Oscillatory Rough Turbulent Boundary-Layers. Ocean Eng, 7(1): 109-152.

Jonsson, I.G. and Carlsen, N.A., 1976. Experimental and Theoretical Investigations in an Oscillatory Turbulent Boundary Layer. J Hydraul Res, 14: 46-60.

Kagan, B.A., Alvarez, O. and Gorchakov, E.V., 2008. Weak Dependence of the SWAN Wave Model on Hydrodynamic Properties of Sea Bottom. Izv Atmos Ocean Phy+, 44(6): 781-786.

Kahma, K.K., 1981. A Study of the Growth of the Wave Spectrum with Fetch. J Phys Oceanogr, 11(11): 1503-1515.

Kahma, K.K. and Calkoen, C.J., 1992. Reconciling Discrepancies in the Observed Growth of Wind-Generated Waves. J Phys Oceanogr, 22(12): 1389-1405.

Kaihatu, J.M., Sheremet, A. and Holland, K.T., 2007. A Model for the Propagation of Nonlinear Surface Waves Over Viscous Muds. Coast Eng, 54(10): 752-764.

Kamphuis, J.W., 2000. Introduction to Coastal Engineering and Management. Advanced Series on Ocean Engineering., 472 pp.

Kineke, G.C., Higgins, E.E., Hart, K. and Velasco, D., 2006. Fine-Sediment Transport Associated with Cold-Front Passages on the Shallow Shelf, Gulf of Mexico. Cont Shelf Res, 26(17-18): 2073-2091.

Kineke, G.C. and Sternberg, R.W., 1992. Measurements of High-Concentration Suspended Sediments Using the Optical Backscatterance Sensor. Mar Geol, 108(3-4): 253-258.

Kitaigordskii, S.A., Krasitskii, V.P. and Zaslavskii, M.M., 1975. Phillips Theory of Equilibrium Range in Spectra of Wind-Generated Gravity-Waves. J Phys Oceanogr, 5(3): 410-420.

Kitaigorodskii, S.A., 1983. On the Theory of the Equilibrium Range in the Spectrum of Wind-Generated Gravity-Waves. J Phys Oceanogr, 13(5): 816-827.

Komen, G.J. et al., 1994. Dynamics and Modelling of Ocean Waves. Cambridge University Press, Cambridge, 532 pp.

Komen, G.J., Hasselmann, S. and Hasselmann, K., 1984. On the Existence of a Fully-Developed Wind-Sea Spectrum. J Phys Oceanogr, 14(8): 1271-1285.

Kraan, C., Oost, W.A. and Janssen, P.A.E.M., 1996. Wave Energy Dissipation by Whitecaps. J Atmos Ocean Tech, 13(1): 262-267.

Kranenburg, W.M., 2008. Modelling Wave Damping by Fluid Mud: Derivation of a Dispersion Equation and an Energy DissipationTerm and Implementation into SWAN, Delft University of technology.

Kranenburg, W.M., Winterwerp, J.C., de Boer, G.J., Cornelisse, J.M. and Zijlema, M., 2011. SWAN-Mud: Engineering Model for Mud-Induced Wave Damping. J Hydraul Eng-Asce, 137(9): 959-975.

Lacy, J.R. and Sherwood, C.R., 2004. Accuracy of a Pulse-Coherent Acoustic Doppler Profiler in a Wave-Dominated Flow. J Atmos Ocean Tech, 21(9): 1448-1461.

Lafon, C., Piazzola, J., Forget, P., Le Calve, O. and Despiau, S., 2004. Analysis of the Variations of the Whitecap Fraction as Measured in a Coastal Zone. Bound-Lay Meteorol, 111(2): 339-360.

Leykin, I.A. and Rozenberg, A.D., 1984. Sea-Tower Measurements of Wind-Wave Spectra in the Caspian Sea. J Phys Oceanogr, 14(1): 168-176.

Li, C.W. and Mao, M., 1992. Spectral Modeling of Typhoon-Generated Waves in Shallow Waters. J Hydraul Res, 30(5): 611-622.

Li, C.Y., Roberts, H., Stone, G.W., Weeks, E. and Luo, Y.X., 2011. Wind Surge and Saltwater Intrusion in Atchafalaya Bay during Onshore Winds Prior to Cold Front Passage. Hydrobiologia, 658(1): 27-39.

Lin, R.Q. and Perrie, W., 1999. Wave-Wave Interactions in Finite Depth Water. J Geophys Res-Oceans, 104(C5): 11193-11213.

Liu, P.C., 1989. On the Slope of the Equilibrium Range in the Frequency-Spectrum of Wind-Waves. J Geophys Res-Oceans, 94(C4): 5017-5023.

Liu, W.T. and Tang, W., 1996. Equivalent Neutral Wind, California Instintude of Technology, Pasadena, Ca.

Luo, W. and Monbaliu, J., 1994. Effects of the Bottom Friction Formulation on the Energy-Balance for Gravity-Waves in Shallow-Water. J Geophys Res-Oceans, 99(C9): 18501-18511.

Lynch, J.F., Irish, J.D., Sherwood, C.R. and Agrawal, Y.C., 1994. Determining Suspended Sediment Particle-Size Information from Acoustical and Optical Backscatter Measurements. Cont Shelf Res, 14(10-11): 1139-1165.

Macpherson, H., 1980. The Attenuation of Water-Waves over a Non-Rigid Bed. J Fluid Mech, 97(Apr): 721-742.

Madsen, O.S., Poon, Y.-K. and Graber, H.C., 1988. Spectral Wave Attenuation by Bottom Friction: Theory. The 21st International Conference on Coastal Engineering, ASCE, pp. 492-504.

Martini, M. et al., 2005. Hydratools, a MATLAB® Based Data Processing Package for Sontek Hydra Data. Proceedings of the IEEE/OES Eighth Working Conference on Current Measurement Technology, pp. 147 - 151.

Massel, S.R., 1996. Ocean Surface Waves; their Physics and Prediction. World Scientific, New Jersey, 491 pp.

Massel, S.R., 2007. Ocean Waves Breaking and Marine Aerosol Fluxes. Atmospheric and Oceanographic Sciences Library. Springer, New York, 328 pp.

Mei, C.C. and Liu, K.F., 1987. A Bingham-Plastic Model for a Muddy Seabed under Long Waves. J Geophys Res-Oceans, 92(C13): 14581-14594.

Miche, R., 1944. Mouvements Ondulatoires des Ders En Profundeur Constante on Decroisante. Annales des Ponts et Chaussees: 25–78, 131–164, 270–292, 369–406.

Mitsuyasu, H., 1977. Measurement of High-Frequency Spectrum of Ocean Surface-Waves. J Phys Oceanogr, 7(6): 882-891.

Mitsuyasu, H. et al., 1980. Observation of the Power Spectrum of Ocean Waves Using a Cloverleaf Buoy. J Phys Oceanogr, 10(2): 286-296.

Moeini, M.H. and Etemad-Shahidi, A., 2007. Application of Two Numerical Models for Wave Hindcasting in Lake Erie. Applied Ocean Research, 29: 137-145.

Morey, S.L., Baig, S., Bourassa, M.A., Dukhovskoy, D.S. and O'Brien, J.J., 2006. Remote Forcing Contribution to Storm-Induced Sea Level Rise during Hurricane Dennis. Geophys Res Lett, 33(19): 5 pp.

Moskowitz, L., 1964. Estimates of Power Spectrums for Fully Developed Seas for Wind Speeds of 20 to 40 Knots. J Geophys Res, 69(24): 5161-5179.

Mossa, J. and Roberts, H.H., 1990. Synergism of Riverine and Winter Storm-Related Sediment Transport Processes in Louisiana's Coastal Wetlands. Gulf Coast Association of Geological Societies Transactions, 40: 635-642.

Neill, C.F. and Allison, M.A., 2005. Subaqueous Deltaic Formation on the Atchafalaya Shelf, Louisiana. Mar Geol, 214(4): 411-430.

Ng, C.O., 2000. Water Waves over a Muddy Bed: A Two-Layer Stokes' Boundary Layer Model. Coast Eng, 40(3): 221-242.

Nielsen, P., 1992. Coastal Bottom Boundary Layer and Sediment Transport. Advanced Series on Ocean Engineering, 4. World Scientific Publishing Co., River Edge, N.J., 324 pp.

Palmsten, M.L., 2001. Application of SWAN Wave Model to a High-Energy Continental Shelf, University of South Florida.

Pawka, S.S., 1983. Island Shadows in Wave Directional Spectra. J Geophys Res-Oc Atm, 88(Nc4): 2579-2591.

Peixoto, J.P. and Oort, A.H., 1992. Physics of Climate. Amer Inst of Physics, New York, NY.

Pepper, D.A. and Stone, G.W., 2004. Hydrodynamic and Sedimentary Responses to Two Contrasting Winter Storms on the Inner Shelf of the Northern Gulf of Mexico. Mar Geol, 210(1-4): 43-62.

Phillips, O.M., 1958. The Equilibrium Range in the Spectrum of Wind-Generated Waves. J Fluid Mech, 4(4): 426-433.

Phillips, O.M., 1985. Spectral and Statistical Properties of the Equilibrium Range in Wind-Generated Gravity-Waves. J Fluid Mech, 156(Jul): 505-531.

Pierson, W.J. and Moskowitz, L., 1964. Proposed Spectral Form for Fully Developed Wind Seas Based on Similarity Theory of S a Kitaigorodskii. J Geophys Res, 69(24): 5181-5191.

Press, W.H., Flannery, B.P., Teukolsky, S.A. and Vetterling, W.T., 1992. Numerical Recipes in Fortran: The Art of Scientific Computing. Cambridge University Press, 933 pp.

RD Instruments, 2001. Waves User’s Guide, RD Instruments.

Reichel, G. and Nachtnebel, H.P., 1994. Suspended Sediment Monitoring in a Fluvial Environment - Advantages and Limitations Applying an Acoustic-Doppler-Current-Profiler. Water Res, 28(4): 751-761.

Resio, D. and Perrie, W., 1991. A Numerical Study of Nonlinear Energy Fluxes Due to Wave-Wave Interactions .1. Methodology and Basic Results. J Fluid Mech, 223: 603-629.

Resio, D.T. and Perrie, W., 2008. A Two-Scale Approximation for Efficient Representation of Nonlinear Energy Transfers in a Wind Wave Spectrum. Part I: Theoretical Development. J Phys Oceanogr, 38(12): 2801-2816.

Richards, S.D., Heathershaw, A.D. and Thorne, P.D., 1996. The Effect of Suspended Particulate Matter on Sound Attenuation in Seawater. J Acoust Soc Am, 100(3): 1447-1450.

Ris, R.C., Holthuijsen, L.H. and Booij, N., 1999. A Third-Generation Wave Model for Coastal Regions - 2. Verification. J Geophys Res-Oceans, 104(C4): 7667-7681.

Roberts, H.H., Braud, D. and Edrington, C., 2010. Results of a Geophysical and Sedimentological Evaluation: Tiger-Trinity Shoals as Sources of Sand for Coastal Restoration, Bureau of ocean energy management, regulation and environment.

Rodriguez, G. and Soares, C.G., 1999. Uncertainty in the Estimation of the Slope of the High Frequency Tail of Wave Spectra. Appl Ocean Res, 21(4): 207-213.

Rodriguez, G., Soares, C.G. and Ocampo-Torres, F.J., 1999. Experimental Evidence of the Transition Between Power Law Models in the High Frequency Range of the Gravity Wave Spectrum. Coast Eng, 38(4): 249-259.

Rogers, W.E. and Holland, K.T., 2009. A Study of Dissipation of Wind-Waves by Mud at Cassino Beach, Brazil: Prediction and Inversion. Cont Shelf Res, 29(3): 676-690.

Rogers, W.E., Hwang, P.A. and Wang, D.W., 2003. Investigation of Wave Growth and Decay in the SWAN Model: Three Regional-Scale Applications. J Phys Oceanogr, 33(2): 366-389.

Rogers, W.E. et al., 2007. Forecasting and Hindcasting Waves with the SWAN Model in the Southern California Bight. Coast Eng, 54(1): 1-15.

Safak, I., Sheremet, A., Allison, M.A. and Hsu, T.J., 2010. Bottom Turbulence on the Muddy Atchafalaya Shelf, Louisiana, USA. J Geophys Res-Oceans, 115.

Sarkar, R.K.A., Aggarwal, V.K., Bhatt, V., Bhaskaran, P.K. and Dube, S.K., 2000. Ocean Wave Model- Sensitivity Experiments. International Conference PORSEC-2000 NIO, Goa, India, pp. 621-627.

Sheremet, A., Jaramillo, S., Su, S.F., Allison, M.A. and Holland, K.T., 2011. Wave-Mud Interaction over the Muddy Atchafalaya Subaqueous Clinoform, Louisiana, United States: Wave Processes. J Geophys Res-Oceans, 116.

Sheremet, A., Mehta, A.J., Liu, B. and Stone, G.W., 2005. Wave-Sediment Interaction on a Muddy Inner Shelf During Hurricane Claudette. Estuar Coast Shelf S, 63(1-2): 225-233.

Sheremet, A. and Stone, G.W., 2003. Observations of Nearshore Wave Dissipation over Muddy Sea Beds. J Geophys Res-Oceans, 108(C11): 11 pp.

Siadatmousavi, S.M., Jose, F. and Stone, G.W., 2009. Simulating Hurricane Gustav and Ike Wave Fields along the Louisiana Innershelf: Implementation of an Unstructured Third-Generation Wave Model, SWAN., Oceans'09, Biloxi, Mississippi, pp. 1-12.

Siadatmousavi, S.M., Jose, F. and Stone, G.W., 2011a. The Effects of Bed Friction on Wave Simulation: Implementation of an Unstructured Third-Generation Wave Model, SWAN. J Coastal Res, 27(1): 140-152.

Siadatmousavi, S.M., Jose, F. and Stone, G.W., 2011b. Evaluation of Two WAM Whitecapping Parameterizations Using Parallel Unstructured SWAN with Application to the Northern Gulf of Mexico, USA. Appl Ocean Res, 33(1): 23-30.

Siadatmousavi, S.M., Jose, F. and Stone, G.W., 2012. On the Importance of High Frequency Tail in Third Generation Wave Models. Coast Eng, 60(0): 248-260.

Snyder, R.L., Dobson, F.W., Elliott, J.A. and Long, R.B., 1981. Array Measurements of Atmospheric-Pressure Fluctuations above Surface Gravity-Waves. J Fluid Mech, 102(Jan): 1-59.

SonTek, 1997. SonTek Doppler Current Meters-Using Signal Strength Data to Monitor Suspended Sediment Concentration, SonTek/YSI Inc., San Diego, CA.

SonTek, 2001. Acoustic Doppler Velocimeter Principles of Operation, SonTek/YSI Inc.

Sorensen, O.R., Kofoed-Hansen, H., Rugbjerg, M. and Sorensen, L.S., 2004. A Third-Generation Spectral Wave Model Using an Unstructured Finite Volume Technique, International Conference on Coastal Engineering 29, pp. 894-906.

Soulsby, R. and Clarke, S., 2005. Bed Shear-Stresses Under Combined Waves and Currents on Smooth and Rough Beds. Hydraulics research report TR 137, HR Wallingford, Hydraulics research report TR 137.

Stone G.W., Jose, F., Siadatmousavi, S.M., Allahdadi, M.N. and Liu, B., 2012. Environmental Investigation of the Long-term Use of Tiger & Trinity Shoals Sand Resources for Large Scale Beach and Coastal Restoration in Louisiana .

Stone, G.W., Zhang, X.P., Gibson, W. and Frederichs, R., 2001. A New Wave-Current Online Information System for Oil Spill Contigency Planning (WAVCIS), 24th Arctic and Marine Oil spill Program Technical Seminar, Edmonton, Alberta, CANADA, pp. 401-425.

Svendsen, I.A., 2006. Introduction To Nearshore Hydrodynamics. Advanced Series on Ocean Engineering. World Scientific Publishing Company, 744 pp.

SWAMP Group, 1985. Ocean Wave Modeling. Plenum Press, New York and London.

SWAN team, 2010. SWAN Cycle III Version 40.81, Scientific and Technical Documentation.

Thomas, B.R., Kent, E.C. and Swail, V.R., 2005. Methods to homogenize wind speeds from ships and buoys. Int J Climatol, 25(7): 979-995.

Thorne, P.D. and Hanes, D.M., 2002. A Review of Acoustic Measurement of Small-Scale Sediment Processes. Cont Shelf Res, 22(4): 603-632.

Thorne, P.D., Holdaway, G.P., Flatt, D., Jones, S.E. and Prandle, D., 1999. Comparison between ADCP and Transmissometer Measurements of Suspended Sediment Concentration. Cont Shelf Res, 19(3): 421-441.

Thorne, P.D., Vincent, C.E., Hardcastle, P.J., Rehman, S. and Pearson, N., 1991. Measuring Suspended Sediment Concentrations Using Acoustic Backscatter Devices. Mar Geol, 98(1): 7-16.

Thornton, E.B., 1977. Re-Derivation of Saturation Range in Frequency-Spectrum of Wind-Generated Gravity-Waves. J Phys Oceanogr, 7(1): 137-140.

Thornton, E.B. and Guza, R.T., 1983. Transformation of Wave Height Distribution. J Geophys Res-Oc Atm, 88(Nc10): 5925-5938.

Toba, Y., 1973. Local Balance in the Air-Sea Boundary Processes, III. On the Spectrum of Wind Waves. Journal of Oceanographical Society of Japan, 29: 209-220.

Tolman, H.L., 1991. A Third-Generation Model for Wind Waves on Slowly Varying Unsteady, and Inhomogeneous Depths and Current. J Phys Oceanogr, 21: 782-797.

Tolman, H.L., 1992a. Effects of Numerics on the Physics in a 3rd-Generation Wind-Wave Model. J Phys Oceanogr, 22(10): 1095-1111.

Tolman, H.L., 1992b. An Evaluation of Expressions for Wave Energy-Dissipation Due to Bottom Friction in the Presence of Currents. Coast Eng, 16(2): 165-179.

Tolman, H.L., 1994. Wind-Waves and Moveable-Bed Bottom Friction. J Phys Oceanogr, 24(5): 994-1009.

Tolman, H.L., 2009. User Manual and System Documentation of WAVEWATCH III ^{TM} Version 3.14.

Tolman, H.L. and Chalikov, D., 1996. Source Terms in a Third-Generation Wind Wave Model. J Phys Oceanogr, 26(11): 2497-2518.

Urick, R.J., 1983. Principles of Underwater Sound. McGraw-Hill, Inc.

van der Westhuysen, A.J., Zijlema, M. and Battjes, J.A., 2007. Nonlinear Saturation-Based Whitecapping Dissipation in SWAN for Deep and Shallow Water. Coast Eng, 54(2): 151-170.

van Vledder, G.P., 2006. The WRT Method for the Computation of Non-Linear Four-Wave Interactions in Discrete Spectral Wave Models. Coast Eng, 53(2-3): 223-242.

van Vledder GP., 2001. Extension of the Discrete Interaction Approximation for Computing Nonlinear Quadruplet Wave-Wave Interactions in Operational Wave Prediction Models, Ocean Wave Measurement and Analysis, San Francisco, pp. 540-549.

van Vledder GP. and Bottema, M., 2003. Improved Modelling of Nonlinear Four-Wave Interactions in Shallow Water, 28th International Conference on Coastal Engineering. ASCE, Cardif, Wales, pp. 459-71.

Walker, N.D. and Hammack, A.B., 2000. Impacts of Winter Storms on Circulation and Sediment Transport: Atchafalaya-Vermilion Bay Region, Louisiana, USA. J Coastal Res, 16(4): 996-1010.

Walmsley, J.L., 1988. On Theoretical Wind-Speed and Temperature Profiles over the Sea with Applications to Data from Sable-Island, Nova-Scotia. Atmos Ocean, 26(2): 203-233.

Weber, N., 1991. Bottom Friction for Wind Sea and Swell in Extreme Depth-Limited Situations. J Phys Oceanogr, 21(1): 149-172.

Wells, J.T., 1983. Dynamics of Coastal Fluid Muds in Low-Tide, Moderate-Tide, and High-Tide-Range Environments. Can J Fish Aquat Sci, 40: 130-142.

Wells, J.T. and Kemp, G.P., 1981. Atchafalaya Mud Stream and Recent Mud Flat Progradation - Louisiana Chenier Plain. Gulf Coast Association of Geological Societies Transactions, 31: 409-416.

Wells, J.T. and Roberts, H.H., 1980. Fluid Mud Dynamics and Shoreline Stabilization: Louisiana Chenier Plain. Seventeenth International Coastal Engineering Conference, Australia, Sydney, pp. 1382-1401.

Westerink, J.J., Luettich, R.A., Baptista, A.M., Scheffner, N.W. and Farrar, P., 1992. Tide and Storm-Surge Predictions Using Finite-Element Model. J Hydraul Eng-Asce, 118(10): 1373-1390.

Whitehouse, R., Soulsby, R., Roberts, W. and Mitchener, H., 2000. Dynamics of Estuarine Muds: A Manual for Practical Applications. Thomas Telford, London

Whitham, G.B., 1965. A General Approach to Linear and Non-Linear Dispersive Waves Using a Lagrangian. J Fluid Mech, 22: 273-283.

Winterwerp, J.C., de Graaff, R.F., Groeneweg, J. and Luijendijk, A.P., 2007. Modelling of wave damping at Guyana mud coast. Coast Eng, 54(3): 249-261.

WMO, 2008. Guide to Meteorological Instruments and Methods of Observation, Measurement of Surface Wind. World Meteorological Organizations, Geneva, Switzerland.

Work, P.A., 2008. Nearshore Directional Wave Measurements by Surface-Following Buoy and Acoustic Doppler Current Profiler. Ocean Eng, 35(8-9): 727-737.

Yamamoto, T., Koning, H.L., Sellmeijer, H. and Vanhijum, E.P., 1978. Response of a Poro-Elastic Bed to Water-Waves. J Fluid Mech, 87(Jul): 193-206.

Yan, L., 1987. An Improved Wind Input Source Term for Third Generation Ocean Wave Modelling. 87-8, Royal Dutch Metrology Institute.

Young, I.R., 1999. Wind Generated Ocean Waves. Elsevier Ocean Engineering Series. Elsevier, 306 pp.

Young, I.R. and Babanin, A.V., 2006. Spectral Distribution of Energy Dissipation of Wind-Generated Waves Due to Dominant Wave Breaking. J Phys Oceanogr, 36(3): 376-394.

Young, I.R. and Gorman, R.M., 1995. Measurements of the Evolution of Ocean Wave Spectra Due to Bottom Friction. J Geophys Res-Oceans, 100(C6): 10987-11004.

Young, I.R. and Vanvledder, G.P., 1993. A Review of the Central Role of Nonlinear-Interactions in Wind Wave Evolution. Philos T Roy Soc A, 342(1666): 505-524.

Young, I.R. and Verhagen, L.A., 1996a. The Growth of Fetch Limited Waves in Water of Finite Depth .1. Total Energy and Peak Frequency. Coast Eng, 29(1-2): 47-78.

Young, I.R. and Verhagen, L.A., 1996b. The Growth of Fetch Limited Waves in Water of Finite Depth .2. Spectral Evolution. Coast Eng, 29(1-2): 79-99.

Zhang, D., Kiu, H. and Lin, P., 2003. The Application of SWAN to the Simulation of a Storm Surge, International Conferene on Estuaries and Coasts, Hangzhou, China.

Zijlema, M., 2009. Multiscale Simulations Using Unstructured Mesh SWAN Model for Wave Hindcasting in The Dutch Wadden Sea. Coastal Dynamics 09, Tokyo, JAPAN, pp. 1-12.

Zijlema, M. and van der Westhuysen, A.J., 2005. On Convergence Behaviour and Numerical Accuracy in Stationary SWAN Simulations of Nearshore Wind Wave Spectra. Coast Eng, 52(3): 237-256.

Zubier, K., Panchang, V. and Demirbilek, Z., 2003. Simulation of Waves at Duck (North Carolina) Using Two Numerical Models. Coast Eng J, 45(3): 439-469.

APPENDIX A: COVER PAGE OF JOURNAL OF APPLIED OCEAN RESEARCH PAPER

Applied Ocean Research 33 (2011) 23–30

Contents lists available at ScienceDirect

Applied Ocean Research

journal homepage: www.elsevier.com/locate/apor

Evaluation of two WAM white capping parameterizations using parallel unstructured SWAN with application to the Northern Gulf of Mexico, USA

S. Mostafa Siadatmousavi [a,b,*], F. Jose [a], G.W. Stone [a,b]

[a] Department of Oceanography and Coastal Sciences, Louisiana State University, Baton Rouge, LA 70803, USA
[b] Coastal Studies Institute, Louisiana State University, Baton Rouge, LA 70803, USA

ARTICLE INFO

Article history:
Received 7 August 2010
Received in revised form
21 October 2010
Accepted 8 December 2010
Available online 30 December 2010

Keywords:
White capping
Parallel unstructured SWAN
WAM
Saturation spectrum
Gulf of Mexico

ABSTRACT

The performance of two well accepted formulations for white capping and wind input of third generation wave models, viz., WAM-3 and WAM-4, were investigated using parallel unstructured SWAN (PunSWAN). Several alternative formulations were also considered to evaluate the effects of higher order steepness and wave number terms in white capping formulations. Distinct model configurations were calibrated and validated against available *in situ* measurements from the Gulf of Mexico. The results showed that some of the *in situ* calibrated models outperform the saturation level calibrated models in reproducing the idealized wave growth curves. The simulation results also revealed that increasing the power of the steepness term can enhance the accuracy of significant wave height (H_s), at the expense of a higher bias for large waves. It also has negative effects on mean wave period (T_a) and peak wave period (T_p). It is also demonstrated that the use of the quadratic wave number term in the WAM-3 formulation, instead of the existing linear term, ameliorates the T_a underestimation; however, it results in the model being unable to reach any saturation level. In addition, unlike H_s and T_p, it has been shown that T_a is sensitive to the use of the higher order WAM-4 formulation, and the bias is decreased over a wide range of wave periods. However, it also increases the scatter index (SI) of simulated T_a. It is concluded that the use of the WAM-4 wind input formulation in conjunction with the WAM-3 dissipation form, is the most successful case in reproducing idealized wave growth curves while avoiding T_a underestimation of WAM-3 and a potential spurious bimodal spectrum of WAM-4; consequently, this designates another perspective to improve the overall performance of third generation wave models.

1. Introduction

Third generation wave models which solve the spectral form of the action balance equation [1] are efficient tools for simulating wave fields in medium- and large-scale domains [2]. Unlike earlier generations, these phase-averaged models include nonlinear wave–wave interaction, and dissipation terms without any prior assumption of spectral shape [3,4]. Among source/sink terms in deep water (wind input, quadruplet wave–wave interaction and energy dissipation [5]), dissipation is widely considered to be the least understood term [6]. Although several different formulations have been proposed for energy dissipation in deep water [6–10], the pulse-based quasi-linear model for the white capping term proposed by Hasselmann [11] remains in use in third generation wave models [12,13]. This approach successfully reproduces the fully developed wind–sea when used in conjunction with efficient quadruplet nonlinear wave interaction formulation referred to as the Discrete Interaction Approximation (DIA) [14], and rescaled wind input formulation of [15,16]. These sets of equations are used in the WAM cycle 3 model and are referred to as WAM-3 hereafter.

Advancements in understanding of wave growth in open water led to a theoretical description of the wind input term, which results in an acceptable level of agreement with *in situ* measurements [17]. The WAM cycle 4 model (WAM-4) employs wind–wave energy transfer parameterization based on quasi-laminar theory, and also considered quadratic dependence of dissipation on the wave number to provide more flexibility in the formulation for white capping dissipation [18]. This formulation also became part of many recent third generation wave models [12,13,19].

The third generation model, Simulating Wave Nearshore (SWAN) [12], has been well suited for both parameterizations, WAM-3 and WAM-4, and hence provides a tangible platform to compare and contrast their performance. Although originally developed for shallow water, SWAN incorporates all source and sink terms for generation and propagation of waves in deep and shallow water, and has been verified for several geographic settings and for different met-ocean conditions [2,8,20–25].

* Corresponding author at: Coastal Studies Institute, Louisiana State University, Baton Rouge, LA 70803, USA. Tel.: +1 225 578 4728; fax: +1 225 578 2520.
E-mail address: ssiada1@lsu.edu (S.M. Siadatmousavi).

0141-1187/$ – see front matter © 2010 Elsevier Ltd. All rights reserved.
doi:10.1016/j.apor.2010.12.002

APPENDIX B: COVER PAGE OF JOURNAL OF COASTAL ENGINEERING PAPER

Coastal Engineering 60 (2012) 248–260

Contents lists available at SciVerse ScienceDirect

Coastal Engineering

journal homepage: www.elsevier.com/locate/coastaleng

On the importance of high frequency tail in third generation wave models

S. Mostafa Siadatmousavi [a,b,*], F. Jose [b], G.W. Stone [a,b]

[a] Department of Oceanography and Coastal Sciences, Louisiana State University, Baton Rouge, LA 70803, USA
[b] Coastal Studies Institute, Louisiana State University, Baton Rouge, LA 70803, USA

ARTICLE INFO

Article history:
Received 19 January 2011
Received in revised form 25 September 2011
Accepted 31 October 2011
Available online 30 November 2011

Keywords:
Wave spectrum
White capping
SWAN
WAVEWATCH-III
High frequency tail
Gulf of Mexico

ABSTRACT

Two well-known third generation wave models, SWAN and WAVEWATCH-III, with different assumptions for high cut-off frequency were used to evaluate the interaction of low and high frequency components in wave spectral evolution. The results showed that WAM cycle 3 formulation overestimates the energy content in frequency band of 0.5–1 Hz for Gulf of Mexico, which suggests using cut-off frequency close to 0.5 Hz rather than 1 Hz would improve the simulated bulk wave parameters. The evaluation of WAM cycle 4 and a newer nonlinear formulation implemented recently for white capping in SWAN also showed the better performance of wave model in oceanic scale with cut-off frequency close to 0.5 Hz. However, WAM cycle 3 was more sensitive to cut-off frequency as well as to the exponent used in the expression for the frequency tail, than other formulations in SWAN. The use of f^{-5} tail shape, rather than the f^{-4} form for the frequency spectrum beyond both cut-off frequencies used in this study, resulted in better agreement between simulated and observed wave parameters for most of the formulations implemented in these models. Also, it was demonstrated that WAM cycle 3 with dynamic cut-off frequency outperformed the corresponding configuration with static cut-off frequency. The suggested modifications for cut-off frequency and the expression for high frequency tail in SWAN substantially ameliorates the widely known underestimation of the average wave period associated with the WAM cycle 3 formulation, and reduces the amount of calculations needed for other formulations.

Published by Elsevier B.V.

1. Introduction

Third generation phase-averaged wave models are efficient tools for simulating wave field in medium- and large-scale domains (Zubier et al., 2003). These models are based on the wave action balance equation, and is given by

$$\frac{DN}{Dt} = \frac{S}{\sigma} \tag{1}$$

in which $N \equiv F/\sigma$ is wave action density, F is wave energy density, $\sigma = 2\pi f$, in which f denotes relative frequency, and S is the total of source/sink terms. Wind input, quadruplet wave–wave interaction and energy dissipation are the most common source/sink terms in deep water wave equation (Komen et al., 1994). Several packages have been suggested for energy transfer from wind to waves and wave energy dissipation, to be implemented in third generation wave models (Babanin et al., 2010; Cavaleri et al., 2007; Komen et al., 1984; Rogers et al., 2003; Tolman and Chalikov, 1996; van der Westhuysen et al., 2007); including WAM cycle 3 (WAM-3 here after) and WAM cycle 4 (WAM-4 here after) formulations. In his pioneering work, Komen et al. (1984) showed that pulse-based quasi-linear model of Hasselmann (1974) proposed for calculating the white capping term, and rescaled wind input formulation of Snyder et al. (1981), were able to reproduce the fully developed wind sea. These formulations became the core of the WAM-3 wave model. A more detailed understanding of the complex interaction of wind and waves in energy transfer to waves resulted in a newer wind input formulation (Janssen, 1991) and was incorporated in WAM-4; along with dissipation term with quadratic dependence on the wave number, to provide more dissipation in high frequency end of the spectrum (Janssen, 2004). The dependence of wave dissipation on mean wavenumber and steepness in WAM formulation resulted in erroneous over-prediction of wind sea in the presence of swell waves (van der Westhuysen et al., 2007). The field evidence do not confirm the enhanced growth of wind sea in combined sea-swell environment (Ardhuin et al., 2007; Young and Babanin, 2006). To solve this problem, van der Westhuysen et al. (2007) suggested a nonlinear saturated-based white capping equation which was entirely local in the frequency domain (Westhuysen hereafter). Their package also included the wind energy transfer of Yan (1987) which was in better agreement with observations than Snyder et al. (1981) during strongly forced waves. Tolman and Chalikov (1996) suggested two different mechanisms for dissipation of energy in high and low ends of the spectrum. In their source package (TC hereafter) the low frequency

* Corresponding author at: Department of Oceanography and Coastal Sciences, Louisiana State University, Baton Rouge, LA 70803, USA. Tel.: +1 225 578 4728; fax: +1 225 578 2520.
E-mail address: ssiada1@lsu.edu (S.M. Siadatmousavi).

0378-3839/$ – see front matter. Published by Elsevier B.V.
doi:10.1016/j.coastaleng.2011.10.007

APPENDIX C: ELSEVIER COPYRIGHT POLICY

Firefox

www.elsevier.com/wps/find/editors.print/editors_update/issue8?avoidEmail=true&printHome=cws_home

ELSEVIER

http://www.elsevier.com

Editors' Update, Issue 8 - October 2004

More freedom for authors

Transformation of Elsevier's copyright policy allows Authors to:

- post final text of article to own websites;
- share the final text with peers world-wide;
- present papers without seeking permission;
- re-use published papers (wholly or partially).

Until recently, authors have been restricted from electronically circulating published papers. To improve this situation, some years ago Elsevier established the right of authors to circulate pre-print versions of their papers on specialised pre-print servers and then to post the published versions of their papers on their institutions' secure internal websites.

Recently, Elsevier copyright policy was further transformed allowing authors to use their published papers more broadly. We discussed this change with Mark Seeley, General Counsel for Elsevier.

Simplified access
This latest development in copyright policy gives authors the right, without having to seek permission, to post the published versions of their papers (the manuscript versions updated to reflect edits) on their personal websites and on their institutions' external websites. The "final version" is the author's Word (or TeX or similar word processing) file, which can be updated by the author to incorporate changes made during the peer-review and editing processes.

"The only requirements are that the paper must be accompanied by a link to the home page of the journal of publication, and that the paper must not be used for commercial purposes," says Seeley. Commercial purposes include systematic distribution or creating links for commercial customers to articles.

Balancing act
"It is always difficult to find the right balance of what is good for the author and what is good for the journal of publication," explains Seeley. "We think this policy change is good for both since authors can increase awareness of their work while we can continue to attract excellent authors to our journals."

For authors, the main improvements to come from the policy change concern scientific advancement and scholarly communication. A side effect is an increase in authors' educational use of their papers.

Scientific advancement
Authors can present their papers at meetings or conferences without having to seek permission to use the material. As well, papers can be reused either in whole or in part for a thesis or dissertation, or for a published collection of works. Hence, advancing the research described in published papers is made more straightforward for authors.

"Even though some authors have not known it, both presenting papers and reusing papers have been existing rights for several years," explains Seeley. "We see this new copyright policy and the way issues like these are clarified as a way to further empower the authoring community."

Scholarly communication
This policy allows authors to share the published version of the paper, either in print or in electronic format, with research colleagues and peers world wide, addressing the core of authors' needs. Scholarly communication, the backbone of scientific advancement, is made less complicated and authors have greater opportunity to discuss their papers in their scholarly and scientific communities.

Educational use
The way is open for increased author comfort when developing courses or lectures using their published papers. Although some publishers have more restrictive copyright policies, authors of Elsevier-published papers have long been allowed to use them, either in print or in electronic format, for courses or for classroom teaching. "This has been allowed for a long time," explains Seeley, "even though some authors have assumed it was not."

Many benefits
"Don't forget that this copyright policy aligns with the institutional repositories model of open access putting the creation of a body of information in the hands of authors and their institutions," says Seeley.

An author receives significant acknowledgement when their paper is published in a reputable journal. Most authors want to take this further and use their papers more widely for professional reasons. Elsevier's newest copyright policy allows it.

Please send responses to this article to **editorsupdate@elsevier.com**.

ISSUE 8: TOPICS

- Elsevier Copyright Policy
- Scopus
- Behind the Scenes
- Virtual Forum on Referee Schools

EDITORS' UPDATE:

- Recent Issues
- Editors Forum
- Index
- Archive
- About
- Contact

APPENDIX D: COVER PAGE OF JOURNAL OF COASTAL RESEARCH PAPER

Journal of Coastal Research	27	1	140–152	West Palm Beach, Florida	January 2011

The Effects of Bed Friction on Wave Simulation: Implementation of an Unstructured Third-Generation Wave Model, SWAN

S. Mostafa Siadatmousavi, F. Jose, and G.W. Stone

Coastal Studies Institute
Department of Oceanography and Coastal Sciences
Louisiana State University
Baton Rouge, LA 70803, U.S.A.
ssiada1@lsu.edu
felixjose@lsu.edu
gagreg@lsu.edu

www.cerf-jcr.org

ABSTRACT

SIADATMOUSAVI, S.M.; JOSE, F., and STONE, G.W., 2011. The effects of bed friction on wave simulation: implementation of an unstructured third-generation wave model, SWAN. *Journal of Coastal Research*, 27(1), 140–152. West Palm Beach (Florida), ISSN 0749-0208.

Parallel implementation of an unstructured Simulating Waves Nearshore (SWAN) model with the Wave Model (WAM) cycle 4 formulation was used to evaluate the performance of a third-generation wave model over large spatial scales. Data from a network of National Data Buoy Center (NDBC) buoys and the Wave Current Information System (WAVCIS) stations were used to assess the skill of the input and output of the wave model. The simulation results reveal that the underestimation of energy in the low-frequency band (0.12–0.17 Hz) can be ameliorated if the model is calibrated using site specific *in situ* measurements instead of the Pierson-Moskowitz spectra. This process led to more than a 25% decrease in the root mean square error between simulated significant wave height and *in situ* observations. Use of the verified model for the Gulf of Mexico, with bed friction computed from grain-size distribution, as opposed to a default constant bed-friction formulation, showed that the wave height difference can exceed 1.5 m or 40% of local wave height for a large spatial extent during extreme events, such as Hurricane Dennis. In addition, with the use of eddy viscosity bed-friction formulation with usSEABED (U.S. Geological Survey), the sediment data results were in better agreement with the *in situ* observations during Hurricane Dennis, with less than a 4% increase in computational cost. The mean wave-height distribution over several cold fronts also demonstrates the influence of bed grain-size parameterization in wave transformation, especially in water depths shallower than 15 m, thereby demonstrating the significance of this study in advancing our understanding of sediment-transport modeling.

ADDITIONAL INDEX WORDS: *JONSWAP, Madsen bed friction formula, numerical modeling, Hurricane Dennis, Gulf of Mexico, SWAN.*

INTRODUCTION

Third-generation wave models are employed as viable tools to simulate the wave field for medium (order of 50 km) and large-scale (oceanic) domains (Zubier, Panchang, and Demirbilek, 2003). These phase-averaged models include deep water source/sink terms, such as wind input, quadruplet wave–wave interaction, and energy dissipation (Komen *et al.*, 1994), among which dissipation in deep water is widely considered to be the least-understood term (Cavaleri *et al.*, 2007). In third-generation models, the most commonly used formulation for deep water dissipation and wind input, are Wave Model (WAM) cycle 3 (WAM-3) and WAM cycle 4 (WAM-4) (Komen *et al.*, 1994). The WAM-3 employs an empirical formulation for wind input (Komen, Hasselmann, and Hasselmann, 1984; Snyder *et al.*, 1981) and a pulse-based, quasilinear model (Hasselmann, 1974). It has been shown that WAM-3 formulations and nonlinear wave interaction formulation referred to as the Discrete Interaction Approximation (DIA) (Hasselmann *et al.*, 1985) can reproduce a fully developed wind–sea (Komen, Hasselmann, and Hasselmann, 1984). A detailed spectral analysis of WAM-3 and its consistent underprediction of wave-energy levels at lower frequencies are well described in Rogers, Hwang, and Wang (2003). The WAM-4 is the newer equation, based on quasilaminar wind–wave energy transfer with more flexibility in the formulation for whitecapping dissipation (Janssen, 2004). In addition, some models, such as MIKE21-SW, exclusively include WAM-4 formulations (Sørensen *et al.*, 2004). Therefore, a detailed study on the spectral performance of WAM-4 is necessitated to help establish whether this formulation also suffers from the underprediction of the energy density in low frequencies.

When waves propagate across intermediate and shallow waters, wave transformation processes, such as bed friction, become important. In shallow water, bed friction is as important as nonlinear wave–wave interaction (Graber and

DOI: 10.2112/JCOASTRES-D-10-00073.1 received 15 May 2010; accepted in revision 17 August 2010.
Published Pre-print online 12 November 2010.

APPENDIX E: LETTER OF PERMISSION; JOURNAL OF COASTAL RESEARCH

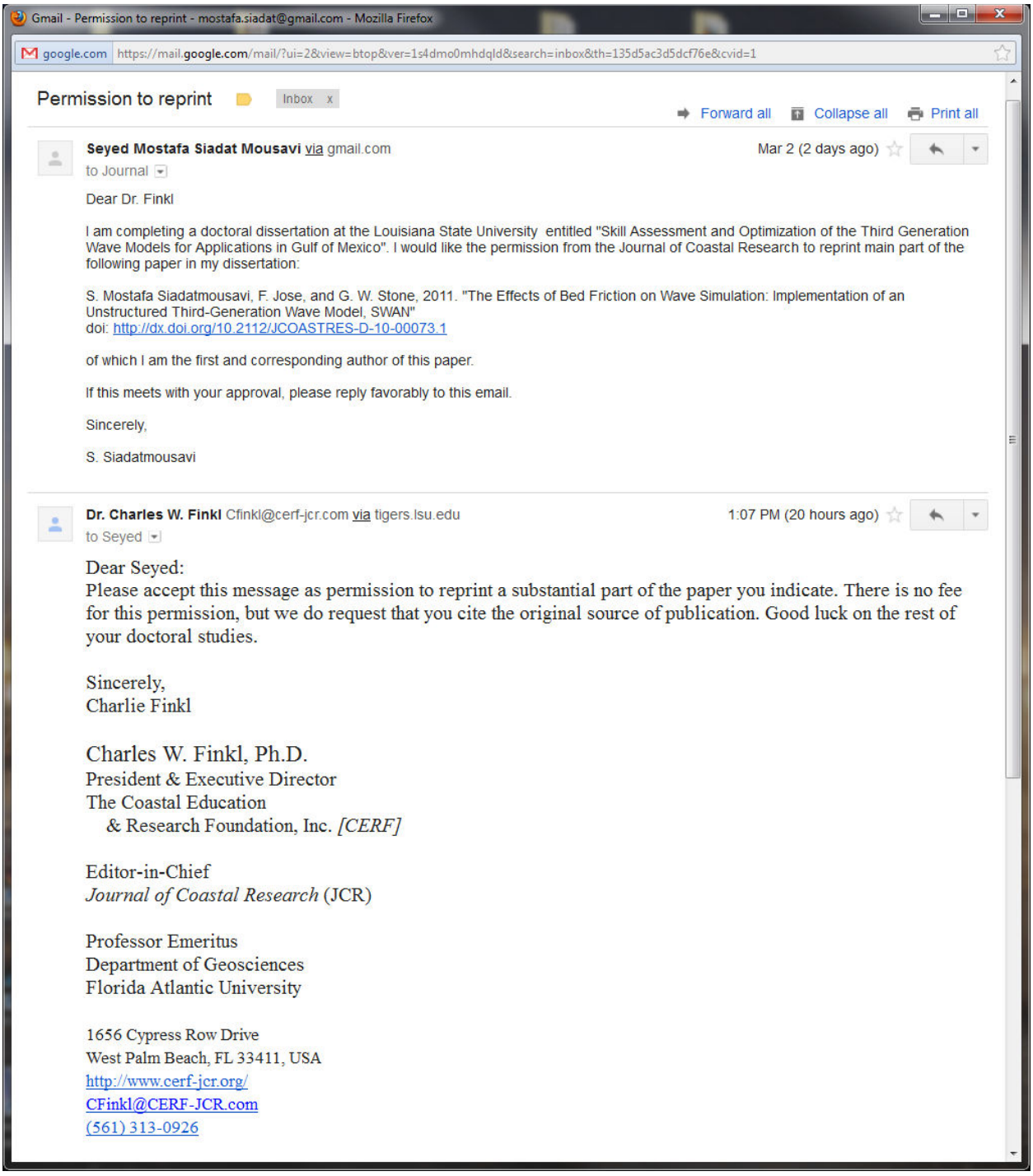

Gmail - Permission to reprint - mostafa.siadat@gmail.com - Mozilla Firefox

google.com https://mail.google.com/mail/?ui=2&view=btop&ver=1s4dmo0mhdqld&search=inbox&th=135d5ac3d5dcf76e&cvid=1

Permission to reprint Inbox x

Forward all Collapse all Print all

Seyed Mostafa Siadat Mousavi via gmail.com Mar 2 (2 days ago)
to Journal

Dear Dr. Finkl

I am completing a doctoral dissertation at the Louisiana State University entitled "Skill Assessment and Optimization of the Third Generation Wave Models for Applications in Gulf of Mexico". I would like the permission from the Journal of Coastal Research to reprint main part of the following paper in my dissertation:

S. Mostafa Siadatmousavi, F. Jose, and G. W. Stone, 2011. "The Effects of Bed Friction on Wave Simulation: Implementation of an Unstructured Third-Generation Wave Model, SWAN"
doi: http://dx.doi.org/10.2112/JCOASTRES-D-10-00073.1

of which I am the first and corresponding author of this paper.

If this meets with your approval, please reply favorably to this email.

Sincerely,

S. Siadatmousavi

Dr. Charles W. Finkl Cfinkl@cerf-jcr.com via tigers.lsu.edu 1:07 PM (20 hours ago)
to Seyed

Dear Seyed:
Please accept this message as permission to reprint a substantial part of the paper you indicate. There is no fee for this permission, but we do request that you cite the original source of publication. Good luck on the rest of your doctoral studies.

Sincerely,
Charlie Finkl

Charles W. Finkl, Ph.D.
President & Executive Director
The Coastal Education
& Research Foundation, Inc. *[CERF]*

Editor-in-Chief
Journal of Coastal Research (JCR)

Professor Emeritus
Department of Geosciences
Florida Atlantic University

1656 Cypress Row Drive
West Palm Beach, FL 33411, USA
http://www.cerf-jcr.org/
CFinkl@CERF-JCR.com
(561) 313-0926

VITA

Seyed Mostafa Siadatmousavi was born in Tehran, Iran, in September 1981. He entered the Department of Civil Engineering at *Isfahan University of Technology* in September 1999 and started his second major in the Department of Mathematics in January 2000. After his graduation from the Civil Engineering Department in July 2003, he started his graduate studies in Marine Structures at the *University of Tehran* under Dr. Peyman Badiei, and focused on third generation wave models. In January 2004, he received his Bachelor of Science in applied mathematics from the *Isfahan University of Technology*. After completing his master studies in July 2006, Mostafa joined the *Sazeh Pardazi Iran* consulting company and worked on several projects on hydrodynamics, sediment transport and integrated coastal zone managements. He entered *Louisiana State University*, Department of Oceanography and Coastal Sciences, as a doctoral student in January 2008, and worked as a graduate research assistant. Mostafa was awarded the Dissertation Year Fellowship 2011-2012 offered by Graduate School of *Louisiana State University*. He will graduate with a Doctor of Philosophy degree in physical oceanography and with a minor in coastal engineering in May 2012.